UNIVERSITÀ DEGLI STUDI DI MILANO

Department of Physics

PhD School in Physics, Astrophysics and Applied Physics
Cycle XXIII

Nonlinear wave excitation and interaction in pure electron plasmas

Disciplinary Scientific Sector FIS/03

Director of the School: Prof. Matteo Paris

Supervisor of the Thesis: Prof. Massimiliano Romé

PhD Thesis of:
Nicola Panzeri

Academic Year 2020/2021

Commission of the final examination:

External Referees:
Dr. James R. Danielson
Prof. Matthew R. Stoneking

Commision Members:
Prof. Ruggero Barni
Prof. Piero Martin
Prof. Lucio Rossi

Final examination:

January, 27 2021

Università degli Studi di Milano, Dipartimento di Fisica, Milano, Italy

MIUR subjects:

FIS/03 - Physics of Matter

PACS:

52.27.Jt

Nature may reach the same result in many ways. Like a wave in the physical world, in the infinite ocean of the medium which pervades all, so in the world of organisms, in life, an impulse started proceeds onward, at times, may be, with the speed of light, at times, again, so slowly that for ages and ages it seems to stay, passing through processes of a complexity inconceivable to men, but in all its forms, in all its stages, its energy ever and ever integrally present.

A single ray of light from a distant star falling upon the eye of a tyrant in bygone times may have altered the course of his life, may have changed the destiny of nations, may have transformed the surface of the globe, so intricate, so inconceivably complex are the processes in Nature.

In no way can we get such an overwhelming idea of the grandeur of Nature than when we consider, that in accordance with the law of the conservation of energy, throughout the Infinite, the forces are in a perfect balance, and hence the energy of a single thought may determine the motion of a universe.

-Nikola Tesla

Contents

List of Figures

List of Tables

Introduction

Motivation

Plasmas with a single sign of charge can be confined for very long times in Penning-Malmberg traps [1]. A major key of the success of these confinement devices lies in their conceptual simplicity and robustness: charged particles are confined thanks to the superposition of a uniform magnetic field (radial confinement) and an electrostatic potential well generated by cylindrical electrodes aligned over the magnetic field axis. Nonneutral plasmas confined in Penning traps have proven to be excellent subjects for well controlled studies on basic physics problems [2] and industrial research over a wide range of parameters. Just to name a few, nonneutral plasma physics enabled advancements and progresses in low uncertainty mass spectrometry and metrology [3], chemical analysis (via broad-range mass spectrometry) [4] and ion pumps [5].
A wide variety of electromagnetic traps have been used to confine and storage antimatter at low energy [6] [7] [8] [9] including Penning traps, magnetic mirrors, and levitated magnetic dipoles. For the long-time confinement, merger and recombination of large numbers of positrons or antiprotons, the method of choice is some variant of the Penning-Malmberg trap, and many of the techniques for the manipulation of charged particles, such as cooling, compression, transfer, and ultimately a stable confinement in a quiescent state, are based on methods first developed by the nonneutral plasma community using electron plasmas [10] [11].
Another enticing and fascinating properties of nonneutral plasmas is the fluid analogy. For cold, magnetized, pure electron plasmas, the electron cyclotron and longitudinal bounce frequency are very high compared to the low frequency $\mathbf{E} \times \mathbf{B}$ motion. The slow transverse dynamics averages over the fast cyclotron and bounce motion, allowing a 2D description of the plasma. The bounce averaged plasma density $n(r, \theta, t)$ evolves under the $v_{\mathbf{E}\times\mathbf{B}}$ flow field according to the continuity equation, and the potential $\phi(r, \theta, t)$ is determined by the density through Poisson's equation. It can be easily shown that these 2D drift-Poisson equations are isomorphic to the Euler equations for an ideal (incompressible and inviscid) 2D fluid. The electric potential corresponds to the stream function and the density to the vorticity. Hence, a pure electron plasma in a Penning-Malmberg trap evolves as an inviscid, incompressible 2D fluid, and can be used to model fluid physics problems with a series of surprising advantages. For example, the vorticity (electron density) can be measured directly by ejecting the plasma out to a phosphor screen coupled to a CCD camera, imaging the axially integrated electron distribution, while it is hard to directly measure the vorticity in a real fluid. Moreover, the plasma is well separated from the longitudinal ends and the confinement electrodes, so there are

no boundary layers to induce shear and complicate the flow. Even though this analogy is well known for decades, it still provides interesting questions and scientific challenges [12] [13] [14] [15].
In the frame of the fluid analogy, the study and control of the various waves and instabilities is of great importance, and it is often intertwined with non-linearity and turbulence. Experiments aimed at unveiling hidden dependencies between parameters or to improve the control over non-equilibrium, unstable configurations can lead not only to the discover of new phenomena and peculiarities in the field of plasma and fluid physics, but also help developing the theory supporting it. Moreover, as Penning-Malmberg traps are the experimental devices of choice for antimatter plasmas, new techniques and a more thorough understanding of basic plasma physics phenomena, like the excitation and interaction of different plasma modes, are likely to be useful tools for a range of applications. In this thesis work, we present the results of the experiments made on two different Penning-Malmberg traps on the excitation and interaction of nonlinear waves in pure electron plasmas.
On the Eltrap device, located at the University of Milan, Italy, we performed experiments on the excitation and control of high order diocotron modes via the rotating electric field technique.
On the CamV device, located at the University of California, San Diego, we investigated the newly discovered phenomenon of TG waves splitting due to the interaction with a diocotron mode.

Thesis overview

Main results

The main results of the thesis are summarized below.

- We successfully prove the validity of the theory for the diocotron mode excitation with the rotating electric field technique exciting high order diocotron modes, up to $l = 7$, never excited before.

- We provide new insights into the resonance dynamics for the diocotron mode growth. These features are mainly due to the non linearity regime of the experiments, and do not have any theoretical support, the theory being only developed for small perturbations in linear regime.

- We show that autoresonance is an efficient and promising mechanism to improve the control over the high order diocotron mode excitation.

- We observe for the first time the dynamics of TG waves propagating on a non-axisymmetric plasma column.

- We experimentally characterize the main features of the newly discovered phenomenon of the TG splitting and, within the limits of our diagnostics, we claim there is a linear dependence of the amplitude of the splitting on the plasma elliptical deformation $\Delta\nu \propto (\epsilon^1)$.

- We elaborate a theoretical model for the TG splitting involving the mixing of orthogonal waves and a degeneracy removal for the $m_r > 1$ cases, and the change in frequency due to a new equilibrium configuration for the $m_\theta \neq 0$ modes.

Organizational note

This thesis consists of three parts and seven chapters, each one devoted to a different aspect of the investigation of nonlinear waves in pure electron plasma columns. Part I is composed of chapters 1, 2 and 3, and presents the theoretical frame of the problem, introducing some key notions of wave theory for nonneutral plasmas. Part II consists of chapter 4 and 5, and is dedicated to the experimental devices where the experiments are performed: Eltrap and CamV, two Penning-Malmberg traps located, respectively, in Milan (Italy) and San Diego (California). Part III, corresponds to chapter 6 and 7, shows the experimental procedures and results: in chapter 6, the experimental campaign performed with Eltrap about the high order diocotron mode excitation and control via the rotating electric field technique introduced in chapter 2; in chapter 7, the experiments performed with CamV regarding the newly found phenomenon of the interaction and mixing of diocotron and TG modes, that manifests as a frequency "splitting" of the TG modes electrostatic signal in the Fourier space.

Chapter 1. Diocotron modes: after a description of the rotational equilibrium of a nonneutral plasma column, the diocotron modes perturbation are introduced in the context of linear theory, and the diocotron mode dispersion relationship is calculated.

Chapter 2. Diocotron modes excitation through rotating electric field: the rotating electric field technique, that allows excitation of high order diocotron modes overcoming the major experimental constraint of the limited number of azimuthally segmented electrode, is introduced for the case of 4-sector and 8-sector electrodes.

Chapter 3. Trivelpiece-Gould modes: after introducing the notion of plasma dielectric tensor, the theory for Trivelpiece-Gould (TG) modes is developed in cylindrical geometry, the natural system for nonneutral plasmas in Penning-Malmberg traps.

Chapter 4. Eltrap: description of the main features of Eltrap, the Penning-Malmberg trap at the physics department of the University of Milan.

Chapter 5. CamV: description of the main features of CamV, the Penning-Malmberg trap devoted to the study of pure electron plasma physics of the Nonneutral Plasma Group at UCSD.

Chapter 6. High order diocotron mode excitation and control: the main experimental results on the excitation and control of high order diocotron modes, through the application of the rotating electric field technique, in Eltrap, are presented, with the associated data analysis, for different excitation schemes.

Chapter 7. TG modes behavior in non axysimmetrical plasma column: the newly found phenomenon of the splitting of TG modes interacting with diocotron modes is described here. After showing all the experimental results, a preliminary theoretical model is presented.

Conclusions and future directions: a brief summary of the future research steps following from the main results of this thesis is given.

Appendix A. Charge collector diagnostic: the experimental technique to measure the total plasma electric charge, in Eltrap, is described.

Appendix B. CCD image early elaboration: the noise removal routine and calibration procedure for the CCD camera diagnostic are explained.

Part I

Introduction to wave theory in nonneutral plasma

CHAPTER 1

Diocotron modes

Kelvin-Helmholtz modes are ubiquitous instabilities in fluid physics, that arise whenever there is shear in the fluid velocity. Thanks to the isomorphism between the equations of a 2D eulerian fluid (incompressible and inviscid) and a nonneutral plasma [16], KH modes are often present in confined pure electrons plasmas such as, for example, when the plasma column is subject to an azimuthal potential perturbation. Purely azimuthal perturbations caused by a shear in the $\mathbf{E}\times\mathbf{B}$ drift velocity are known, in nonneutral plasma physics, as "$diocotron$ modes", and they correspond, in the context of fluid physics, to KH modes. The diocotron modes dominate the low frequency, $\sim$ kHz, dynamics of nonneutral plasmas in Penning-Malmberg traps [17] and toroidal traps [18]. In this chapter, the diocotron modes dispersion relationship is derived, in the context of linear perturbation theory for cold, magnetized, pure electron plasma columns [19]. Physical quantities are in CGS system units.

1.1 Cold-fluid equilibrium rotation

Let us consider an infinite long column of magnetized nonneutral plasma (of, for definiteness, electrons) in a uniform magnetic field, with a flat profile of the form

$$n_e(r) = \begin{cases} n_e = const & 0 \le r \le R_p \\ 0 & R_p < r \le R_w \end{cases} \tag{1.1}$$

with R_p the plasma radius and R_W the trap radius.
By solving the Poisson equation associated with the profile (1.1) in cylindrical coordinates, and with the boundary conditions for our conductive trap wall $\phi(R_W) = 0$, we obtain the electrostatic potential

$$\phi(r) = \begin{cases} \frac{m_e}{4e}\omega_p^2(r^2 - R_p^2) + \frac{m_e}{2e}\omega_p^2 R_p^2 \log\frac{R_p}{R_W} & 0 \le r < R_p \\ \frac{m_e}{2e}\omega_p^2 R_P^2 \log\frac{r}{R_W} & R_P \le r < R_W \end{cases} \tag{1.2}$$

$\omega_p^2 = \dfrac{4\pi n_e e^2}{m_e}$ being the well known plasma frequency.
From (1.2) we immediately obtain, via $\mathbf{E} = -\nabla\phi$, the electrostatic field produced by the plasma

$$E_r(r) = \begin{cases} -\frac{m_e}{2e}\omega_p^2 r & 0 \le r < R_p \\ -\frac{m_e}{2e}\omega_p^2 \frac{R_p^2}{r} & R_p \le r < R_W \end{cases} \tag{1.3}$$

In the cold fluid approximation the radial force balance can be expressed as

$$-\frac{m_e v_\theta^2(r)}{2} + eE(r) = -\frac{e}{c} v_\theta(r) B \tag{1.4}$$

the left side being the outward forces, centrifugal and Coulomb force respectively, and the right side the inward force, the Lorentz force.
Substituting with (1.3) we obtain, for the plasma angular velocity $\omega(r) = \dfrac{v_\theta(r)}{r}$

$$\omega^2 + \frac{1}{2}\omega_p^2 - \omega\Omega_C = 0 \tag{1.5}$$

with $\Omega_C = \dfrac{Be}{m_e c}$ the usual electron cyclotron frequency.
Solving (1.5) we obtain

$$\omega^{\pm} = \frac{1}{2}\Omega_C \left[1 \pm \left(1 - \frac{2\omega_p^2}{\Omega_C^2} \right)^{\frac{1}{2}} \right] \tag{1.6}$$

By imposing the reality of $\omega^{\pm}$ and writing it as a condition on the plasma density, we obtain the Brillouin density limit: $n_b = \dfrac{B^2}{8\pi m_e c^2}$. Nonneutral plasma can be radially confined only if $n_e \leq n_b$. For plasma densities higher than the Brillouin limit, plasma cannot be confined, because the de-focusing, outward force becomes too strong.

Eq.(1.6) shows that the plasma column rotates as rigid rod, because in (1.6) there is no dependence on r, with a slow rotation, ω^-, or a fast rotation ω^+.
For a low density plasma (in terms of Brillouin limit) where $\dfrac{\omega_p^2}{\Omega_c} \ll 1$, (1.6) can be rewritten as

$$\omega_{re}^+ \simeq \Omega_c \qquad\qquad \omega_{re}^- \simeq \frac{\omega_p^2}{2\Omega_c} \equiv \omega_{E\times B} \tag{1.7}$$

The plasma column can rotate with the fast electron cyclotron frequency, $\omega^+ = \Omega_c$, or with the slow $E_r \hat{\mathbf{r}} \times B\hat{\mathbf{z}}$ rotation, $\omega^- = \omega_{E\times B}$. $\omega_{E\times B}$ is the plasma $E \times B$ drift rotation frequency. Whether the plasma column is rotating with either slow ω^- or fast ω^+ rotation velocity, depends on the way in which the nonneutral plasma is formed and confined (e.g. injection conditions). In our case, cold, low density and strongly magnetized pure electron plasmas confined in Penning-Malmberg traps, the plasma columns always rotates with $\omega = \omega_{E\times B}$. Hence the electron motion satisfies the inequalities

$$\omega_{E\times B} << \omega_b << \Omega_C \tag{1.8}$$

from which we can take an average of the dynamics on the longitudinal dimension, and consider the trapped plasma as a 2D fluid system in (r, θ).

1.2 Linear perturbation theory

Let us consider a cold-fluid guiding-center model, where we neglect the inertial effects associated with the electrons mass $m_e \to 0$: eq.(1.4) becomes

$$0 = -en_e(\mathbf{x},t)\left[\mathbf{E}(\mathbf{x},t) + \frac{1}{c}\mathbf{v}(\mathbf{x},t) \times B\hat{\mathbf{e}_\mathbf{z}}\right] \tag{1.9}$$

from which we can immediately write

$$\mathbf{v}(\mathbf{x},t) = -\frac{c}{B}\nabla\phi \times \hat{\mathbf{e}_\mathbf{z}} \tag{1.10}$$

Fluid velocity and density are related via the continuity equation

$$\frac{\partial}{\partial t}n_e(\mathbf{x},t) + \nabla \cdot [n_e(\mathbf{x},t)\mathbf{v}(\mathbf{x},t)] = 0 \tag{1.11}$$

and, considering the cylindrical geometry of the problem, that we are dealing with a 2D system (r,θ), and assuming perturbations with no z-dependence ($\partial\phi/\partial z = 0$), we can rewrite the continuity equation in a form more explicit for our problem:

$$\left\{\frac{\partial}{\partial t} - \frac{c}{Br}\frac{\partial\phi}{\partial\theta}\frac{\partial}{\partial r} + \frac{c}{Br}\frac{\partial\phi}{\partial r}\frac{\partial}{\partial\theta}\right\}n_e(r,\theta,t) = 0 \tag{1.12}$$

We can then relate plasma density and plasma potential via Poisson equation

$$\left\{\frac{1}{r}\frac{\partial}{\partial r}r\frac{\partial}{\partial r} + \frac{1}{r^2}\frac{\partial^2}{\partial\theta^2}\right\}\phi(r,\theta,t) = 4\pi e n_e(r,\theta,t) \tag{1.13}$$

Equations (1.10),(1.12) and(1.13) constitute a self-consistent and fully nonlinear description of the plasma evolution in the cold fluid, 2D, mass-less ($m_e \to 0$) guiding center approximation.
Let us consider small-amplitude perturbations about an azimuthally symmetric equilibrium ($\frac{\partial}{\partial\theta} = 0$) and investigate the stability properties of n_e and ϕ under such perturbations.
The perturbed electron density and electrostatic potential are expressed as

$$\begin{aligned} n_e(r,\theta,t) &= n_e^0(r) + \sum_{l=-\infty}^{+\infty}\delta n_e^l(r)\exp(il\theta - i\omega t) \\ \phi(r,\theta,t) &= \phi^0(r) + \sum_{l=-\infty}^{+\infty}\delta\phi^l(r)\exp(il\theta - i\omega t) \end{aligned} \tag{1.14}$$

where l is the azimuthal mode number of the perturbation, we assume a 2D dynamics evolution ($\frac{\partial}{\partial z} = 0$), and ω is the complex oscillation frequency of the perturbations. $Im(\omega) > 0$ corresponds to instability, that is to say the amplitude of the perturbation (mode) grows in time.
n_e^0 and ϕ^0 are the equilibrium density profile and electrostatic potential related by the one-dimensional (having assumed $\frac{\partial}{\partial\theta} = 0$ and $\frac{\partial}{\partial z} = 0$) Poisson equation

$$\frac{1}{r}\frac{\partial}{\partial r}r\frac{\partial}{\partial r}\phi_0(r) = 4\pi e n_e^0(r) \tag{1.15}$$

For small amplitude perturbations, and low density plasma, with $\frac{\omega_p^2}{\Omega_c^2} << 1$ substituting eq. (1.14) in eq.(1.12)

$$\left(\omega - l\omega_{re}^-(r)\right)\delta n_e^l(r) = -cl\frac{\delta\phi^l(r)}{B_r}\frac{\partial}{\partial r}n_e^0(r) \tag{1.16}$$

where $\omega_{re}^-(r)$ is the equilibrium $E_r\hat{\mathbf{r}} \times B\hat{\mathbf{z}}$ rotation velocity of the electron fluid defined by

$$\omega_{re}^-(r) = -\frac{cE_r(r)}{rB} = \frac{c}{rB}\frac{\partial}{\partial r}\phi_0(r) \tag{1.17}$$

In the case of a flat profile as (1.1), the equilibrium rotation velocity is indeed the diocotron frequency $\omega_{re}^- = \omega_{E\times B}$. Substituting (1.14) and (1.16) into the Poisson equation(1.15) we obtain the eigenvalue equation:

$$\frac{1}{r}\frac{\partial}{\partial r}r\frac{\partial}{\partial r}\delta\phi^l(r) - \frac{l^2}{r^2}\delta\phi^l(r) = -\frac{l}{\omega_c r}\frac{\delta\phi^l(r)}{\omega - l\omega_{re}^-(r)}\frac{\partial}{\partial r}\omega_p^2(r) \tag{1.18}$$

For a given equilibrium density profile $n_e^0(r)$, the eigenvalue equation (1.18) can be used to determine the eigenfunction $\delta\phi^l(r)$ and the complex associated frequency ω^l.
It is analytically proven that, a *necessary* condition for instability to small amplitude electrostatic perturbation is that $\frac{\partial n_e^0}{\partial r}$ changes sign in $0 < r < R_P$. Alternatively, in terms of angular rotation, a *necessary* condition for instability is that $\frac{\partial}{\partial r}\frac{1}{r}\frac{\partial}{\partial r}\left(r^2\omega_{re}^-(r)\right)$ changes sign in $0 < r < R_P$.

1.3 Diocotron modes

Let us solve the eigenvalue equation (1.18) for the flat density profile (1.1). By substituting (1.1) in (1.18), considering that $\frac{\partial n_e^0(r)}{\partial r} = -\hat{n_e}\delta(r - R_P)$ we have

$$\frac{1}{r}\frac{\partial}{\partial r}r\frac{\partial}{\partial r}\delta\phi^l(r) - \frac{l^2}{r^2}\delta\phi^l(r) = \frac{l}{r}\frac{\omega_p^2}{\Omega_C}\frac{\delta\phi^l(R_p)}{\left(\omega - l\omega_{re}^-(R_p)\right)}\delta(r - R_p) \tag{1.19}$$

Except for $r = R_p$, eq.(1.19) can be written as

$$\frac{1}{r}\frac{\partial}{\partial r}r\frac{\partial}{\partial r}\delta\phi^l(r) - \frac{l^2}{r^2}\delta\phi^l(r) = 0 \tag{1.20}$$

If we impose $\delta\phi \propto r^\alpha$ from eq.(1.20) we obtain $\alpha = \pm l$ hence, the most general solution with this form is $\delta\phi^l = Ar^l + Br^{-l}$. If we solve (1.20) separately for $0 \le r < R_p$ and $R_p < r \le R_W$, with the boundary condition $\delta\phi(R_W) = 0$ and the continuity of $\delta\phi$ in R_p, we obtain

$$\delta\phi(r) = \begin{cases} Br^l + Cr^{-l} & 0 \le r < R_p \\ \left(BR_p^l + CR_p^{-l}\right)\left(\dfrac{1 - (\frac{r}{R_W})^{2l}}{1 - (\frac{R_p}{R_W})^{2l}}\right)\left(\dfrac{R_p}{r}\right)^l & R_p \le r < R_W \end{cases} \tag{1.21}$$

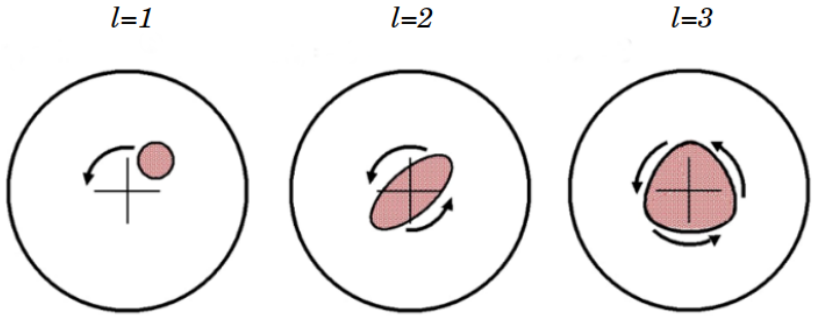

Figure 1.1: Sketch of a plasma density profile $n(r,\theta)$ subject to different diocotron modes. The magnetic field is coming out from the page.

with B and C to be determined. If we multiply by r and then integrate the eigenvalue equation 1.19 on an infinitesimally small step around $r = R_W$ we have

$$R_p \frac{\partial}{\partial r}\delta\phi|_{r=R_p^-} - R_p \frac{\partial}{\partial r}\delta\phi|_{r=R_p^+} = -2l\omega_{E\times B}\frac{\delta\phi(R_p)}{(\omega - l\omega_{re}^-(R_p))} \tag{1.22}$$

Eq.(1.22) relates the discontinuity in the radial electric field at the density profile discontinuity to the perturbed charge in R_p. By substituting the expression (1.14) for the potential and ω_{re}^- in (1.22), with some algebraic manipulation we have

$$\left(\frac{\omega}{\omega_{E\times B}}\right)^2 - b_l\left(\frac{\omega}{\omega_{E\times B}}\right) + c_l = 0 \tag{1.23}$$

with $b_l = l + \left(\frac{R_p}{R_W}\right)^2$ and $c_l = l - 1 + \left(\frac{R_p}{R_W}\right)^2$.
Finally, the oscillation frequency ω of a small amplitude electrostatic perturbation propagating on the surface of a pure electron plasma column is

$$\omega_l = \omega_{E\times B}\left(l - 1 + (\frac{R_p}{R_W})^{2l}\right) \tag{1.24}$$

ω_l is known as the angular frequency of the l^{th} *diocotron mode*. The diocotron modes are z-independent, low-frequency distortions of the plasma column which propagate azimuthally due to the $\mathbf{E}\times\mathbf{B}$ drift created by the perturbed potential $\delta\phi$. Since $Im(\omega_l) = 0$ $\forall l$, the system is stable for all mode numbers l, consistent with the necessary conditions stated above. In fig. 1.1 a representative drawing of a plasma column subject to different diocotron perturbations. The l^{th} term of the Fourier series corresponds to the l^{th} diocotron mode. Indeed, as the $l = 2$ diocotron mode (elliptical deformation) has two wavelengths in $(0, 2\pi)$, the $l = 3$ (triangular deformation) has three wavelengths and so on, so $\sin(2\theta)$ and $\cos(2\theta)$ have two periods in $(0, 2\pi)$, $\sin(3\theta)$ and $\cos(3\theta)$ have three, etc.

Another important feature of the diocotron modes is the fact that they are negative energy modes. The distorted plasmas shown in fig. 1.1 have lower potential energies than the corresponding cylindrically symmetric equilibrium plasma with the same density. Therefore, the total plasma energy with the mode present is lower than the original equilibrium. A key feature of these modes is that they can be driven unstable by processes that remove energy and angular momentum from the plasma, such as resistance

in the wall electrodes [20] and collisions with other species [21].
Eq. (1.24) does not take into account second order corrections due, for example, to the plasma finite length and distortion of plasma cross-section [22] [23]: these more refined models allow derivation of a more accurate expression for the electric field $\mathbf{E}$, adding corrective terms to eq. (1.24). Moreover, experiments show there exists a nonlinear relationship between frequency and amplitude of the mode, with $\frac{\partial \omega_l}{\partial A_l} < 0 \; \forall l \geq 2$, and $\frac{\partial \omega_l}{\partial A_l} > 0$ for $l = 1$. Except for the $l = 1$ and $l = 2$ mode, this effect has not yet a complete theoretical explanation.

CHAPTER 2

Diocotron mode excitation through rotating electric field

One of the biggest limitations in exciting high order $l > 2$ diocotron modes on a nonneutral plasma column in a Penning trap is given by the limited number of azymuthally sectored electrodes in experimental devices (8 is the maximum in both Eltrap and CamV), see Part II of this thesis. Indeed, being the diocotron modes purely azimuthal potential perturbations, only some angular configurations of a static external drive induce, more or less efficiently, specific modes excitations [24], while a fully cylindrical electrode cannot excite any diocotron mode. In this chapter, a technique to excite high order diocotron modes is exploited [25] [26]: it relies on an external rotating electric field (the phase differences of the drive signal between adjacent sectors is constant) at a specific frequency, and, depending on the geometry and the structure of the electric field (dipolar, quadrupolar, etc...) it allows excitation of high order diocotron modes despite the limited number of azimuthal sectors in the segmented electrode in use.

2.1 Potential perturbation with generical boundary condition

To see how to excite high order diocotron mode through a rotating electric field, let us solve again eq. (1.20) with the boundary condition $\delta\phi(R_w) = \delta\phi(\theta, t)$: we are applying a perturbation on the plasma column by imposing an arbitrary electrostatic potential that varies in time and angular position. Firstly, let us decompose the applied potential on the wall with a Fourier series in trigonometric polynomials

$$\delta\phi(R_w, \theta, t) = \sum_l c_l \exp(il\theta - i\omega_d t) \tag{2.1}$$

where ω_d is the angular frequency of the external drive applied at R_w. As already done in the previous chapter, we look for a solution of (1.20) of the form $\delta\phi(r) = Ar^l + Br^{-l}$ separately for inside and outside of the plasma:

$$\delta\phi(r) = \begin{cases} Ar^l + Br^{-l} & 0 \leq r < R_p \\ Cr^l + Dr^{-l} & R_p \leq r \leq R_W \end{cases} \tag{2.2}$$

Again, to find A, B, C, D, we impose the potential continuity on the plasma surface $\delta\phi(R_p^-) = \delta\phi(R_p^+)$, the discontinuity of the radial electric field in R_p (and this conditions has the same form of eq. (1.22)), and using (2.1) for $\delta\phi(R_w)$. Noticing that $B = 0$ to

avoid the potential divergence for $r = 0$, we obtain, with some algebraic manipulation

$$\begin{aligned} A &= \frac{c_l(t)\left(\omega_d - l\omega_{E\times B}\right) R_w^{-l}}{\omega_d - \omega_l} \\ C &= \frac{c_l(t)\left(\omega_d - (l+1)\omega_{E\times B}\right) R_w^{-l}}{\omega_d - \omega_l} \\ D &= \frac{c_l(t)\omega_{E\times B} R_p^{2l} R_w^{-l}}{\omega_d - \omega_l} \end{aligned} \tag{2.3}$$

Now that we have found the general expression for a potential perturbation with an external drive (the potential applied on the wall (2.1)), let us consider two more specific cases, that can be reproduced experimentally with our devices.

2.2 Four sectors excitation

Let us consider the case of an azymuthally segmented cylindrical sector with 4 sections of angular width $\Delta\alpha = 90°$. The potential on this sector can be expressed as

$$\begin{aligned} \delta\phi(R_w, \theta, t) = \sum_{m=0}^{3} V_m(t) \left[H(\theta - m\frac{\pi}{2}) - H(\theta - (m+1)\frac{\pi}{2} \right] \\ V_m = V_d \cos\left(\omega_d t + \sigma m \frac{\pi}{2}\right) \end{aligned} \tag{2.4}$$

where V_d and ω_d are, respectively, the amplitude and the frequency of the external drive, that is to say, the potential we are applying on the wall, at R_w, and $H(\theta, m)$ is the Heaviside function. σ defines the drive rotation direction and can only assume the value $\sigma = \pm 1$: if we choose a potential that rotates in the same direction of the plasma (co-rotation) $E \times B$ drift, then $\sigma = -1$; if the wall potential rotates in the opposite direction of the $E \times B$ drift (counter-rotation), then $\sigma = +1$

We can rewrite eq. (2.4) in the more explicit form of a dipolar rotating potential, see also fig. 2.1

$$\delta\phi(R_W, \theta, t) = \begin{cases} V_0 = V_d \cos(\omega_d t) & 0 \le \theta < \dfrac{\pi}{2} \\ V_1 = \sigma V_d \sin(\omega_d t) & \dfrac{\pi}{2} \le \theta < \pi \\ V_2 = -V_0 = -V_d \cos(\omega_d t) & \pi \le \theta < \dfrac{3\pi}{2} \\ V_3 = -V_1 = -\sigma V_d \sin(\omega_d t) & \dfrac{3\pi}{2} \le \theta < 2\pi \end{cases} \tag{2.5}$$

If we write (2.4) in the form (2.1), the Fourier coefficients are

$$c_l = \begin{cases} \dfrac{V_0 - V_1}{l\pi} - i\dfrac{V_0 + V_1}{l\pi} & l = 4k+1 \\ \dfrac{V_1 - V_0}{l\pi} + i\dfrac{V_0 + V_1}{l\pi} & l = 4k+3 \end{cases} \tag{2.6}$$

with $k \in \mathbb{Z}$. Only certain l-values are present: the conditions on l translate to a selection of the possible modes that can be excited with this geometrical configuration for the external potential drive. In particular, only the odd modes can be excited. Making the

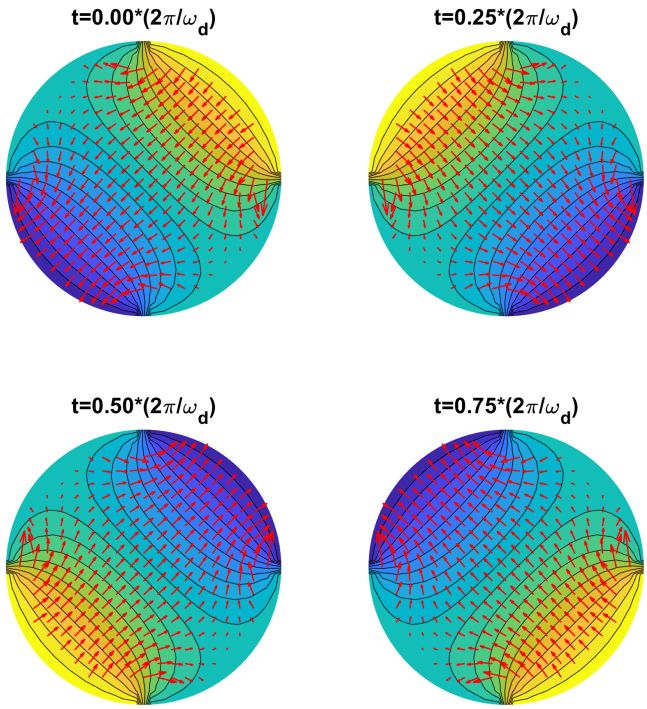

Figure 2.1: Contour-plot of the electrostatic potential for a rotating dipole, see (2.4). It is obtained with a 4 sector electrode, and the potential between adjacent sectors is shifted by $\pi/2$.

dependency on σ explicit through eq.(2.5), we obtain

$$\sigma = +1: \qquad c_l(t) = \begin{cases} \left(\dfrac{V_d \exp(-i\pi/4)}{\pi(4k+1)}\right) e^{+i\omega_d t} & l = 4k+1 \\ \left(\dfrac{V_d \exp(+i\pi/4)}{\pi(4k+3)}\right) e^{-i\omega_d t} & l = 4k+3 \end{cases} \tag{2.7}$$

$$\sigma = -1: \qquad c_l(t) = \begin{cases} \left(\dfrac{V_d \exp(-i\pi/4)}{\pi(4k+1)}\right) e^{-i\omega_d t} & l = 4k+1 \\ \left(\dfrac{V_d \exp(+i\pi/4)}{\pi(4k+3)}\right) e^{+i\omega_d t} & l = 4k+3 \end{cases} \tag{2.8}$$

These coefficients describes the perturbation at a certain time t, while we are interested in how the potential perturbation evolves, on the plasma surface, given the perturbation at $t = 0$. To obtain this kind of information, we perform a Laplace transform in time of the potential

$$\delta\phi(R_e, \theta, s) = \int_0^{+\infty} \delta\phi(R_w, \theta, t) \exp(-st) dt = \sum_{-\infty}^{+\infty} c_l(s) \exp(-il\theta) \tag{2.9}$$

and then we calculate the inverse Laplace transform of eq.(2.9) to look for secular growth, resonances or instabilities.
So if we perform the Laplace transform of the coefficient (2.7) and (2.8) we have

$$\sigma = +1: \qquad c_l(s) = \begin{cases} \dfrac{K}{s - i\omega_d} & l = 4k+1 \\ \dfrac{K'}{s + i\omega_d} & l = 4k+3 \end{cases} \tag{2.10}$$

$$\sigma = -1: \qquad c_l(s) = \begin{cases} \dfrac{K}{s + i\omega_d} & l = 4k+1 \\ \dfrac{K'}{s - i\omega_d} & l = 4k+3 \end{cases} \tag{2.11}$$

K and K′ being constants. Now we select one of the four cases for $c_l(s)$, we substitute it in the expression found for $\delta\phi(r)$ (2.3), to obtain $\delta\phi(R_p, \theta, s)$ and we perform the inverse Laplace transform, to evaluate the details of the temporal evolution of the potential perturbation on the plasma surface.

$$\sigma = +1: \quad \delta\phi(R_p, \theta, t) = \begin{cases} K \left(\dfrac{R_p}{R_w}\right)^l \left(\dfrac{\omega_l - l\omega_{E\times B}}{\omega_l + \omega_d}\right) \exp(-i\omega_l t - il\theta) + & l = 4k+1 \\ \quad + \left(\dfrac{\omega_l + l\omega_{E\times B}}{\omega_l + \omega_d}\right) \exp(i\omega_d t - il\theta) & \\ K' \left(\dfrac{R_p}{R_w}\right)^l \left(\dfrac{\omega_l - l\omega_{E\times B}}{\omega_l - \omega_d}\right) \exp(-i\omega_l t - il\theta) + & l = 4k+3 \\ \quad + \left(\dfrac{\omega_l + l\omega_{E\times B}}{\omega_l - \omega_d}\right) \exp(-i\omega_d t - il\theta) & \end{cases} \tag{2.12}$$

We are interested in finding those values of ω_d for which $\delta\phi(R_p)$ grows the most, so basically the poles of eqs. (2.12). There is a singularity only if $l = 4k + 3$, for $\omega_d = \omega_l$: in

this case the potential perturbation on the plasma surface is

$$\delta\phi(r = R_p, \theta, t) = K' \left(\frac{R_p}{R_w}\right)^l (1 + i(l\omega_{E\times B} - \omega_l)t) \exp(i(l\theta - \omega_l t)) \tag{2.13}$$

The perturbation amplitude grows linearly in time, and propagates with frequency ω_l.
In the case of a 4 azimuthal sectors electrode, if we apply an external dipolar potential (drive) that is counter rotating with respect to the $\mathbf{E} \times \mathbf{B}$ velocity drift, and has a frequency $\omega_d = \omega_l$, then the plasma resonates: the l^{th} diocotron modes is excited, and propagates on the plasma surface $r = R_p$ with its characteristics frequency ω_l. Only the modes with $l = 4k + 3$ can be excited when the external perturbation frequency matches their mode frequency. As the perturbation persists, the amplitude of the l^{th} diocotron modes grows linearly in time. We are sure that modes excited are indeed diocotron modes because they are the only solution for the eigenvalue equation (1.19)
The same applies for the case of a co-rotating drive $\sigma = -1$ but, as can be inferred from eq.(2.12), only the diocotron modes with $l = 4k + 1$ can propagate in this case.

2.3 Eight sector excitation

Let us now consider the case of an azimuthally segmented cylindrical electrodes with 8 sections of angular width $\Delta\alpha = 45°$. The external potential drive applied through this electrode can be expressed as

$$\begin{aligned} \delta\phi(R_w, \theta, t) = \sum_{m=0}^{7} V_m(t) \left[H(\theta - m\frac{\pi}{4}) - H(\theta - (m+1)\frac{\pi}{4})\right] \\ V_m = V_d \cos\left(\omega_d t + \sigma m \frac{\pi}{2}\right) \end{aligned} \tag{2.14}$$

where, again, V_d and ω_d are the amplitude and frequency of the potential applied on the wall $r = R_w$.
If we write (2.14) in the more explicit form of a quadrupolar rotating potential (see also fig. 2.2)

$$\delta\phi(R_W, \theta, t) = \begin{cases} V_0 = V_d \cos(\omega_d t) & 0 \le \theta < \frac{\pi}{4} \\ V_1 = \sigma V_d \sin(\omega_d t) & \frac{\pi}{4} \le \theta < \frac{\pi}{2} \\ V_2 = -V_0 = -V_d \cos(\omega_d t) & \frac{\pi}{2} \le \theta < \frac{3\pi}{4} \\ V_3 = -V_1 = -\sigma V_d \sin(\omega_d t) & \frac{3\pi}{4} \le \theta < \pi \\ V_4 = V_0 = V_d \cos(\omega_d t) & \pi \le \theta < \frac{5\pi}{4} \\ V_5 = V_1 = \sigma V_d \sin(\omega_d t) & \frac{5\pi}{4} \le \theta < \frac{3\pi}{2} \\ V_6 = -V_0 = -V_d \cos(\omega_d t) & \frac{3\pi}{2} \le \theta < \frac{7\pi}{4} \\ V_7 = -V_1 = -\sigma V_d \sin(\omega_d t) & \frac{7\pi}{4} \le \theta < 2\pi \end{cases} \tag{2.15}$$

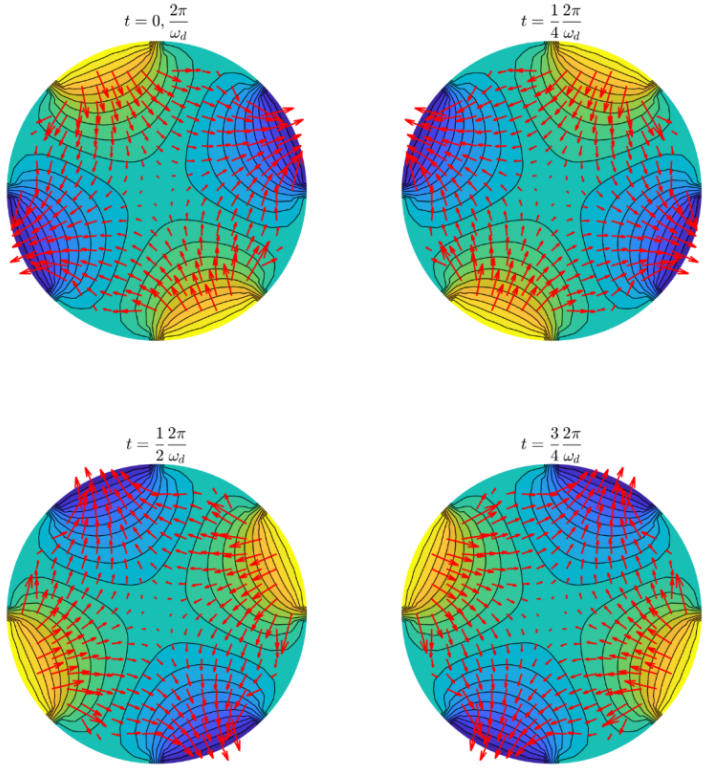

Figure 2.2: Contour-plot of the electrostatic potential for a rotating quadrupole, see (2.4). It is obtained with an 8 sector electrode, and the potential between adjacent sectors is shifted by $\pi/2$.

The coefficients of the Fourier series (2.1) are then

$$c_l = \begin{cases} \dfrac{(-1)^l V_0 + (-1)^{l+1} V_1}{l\pi} - i\dfrac{V_0 + V_1}{l\pi} & l = 8k+2 \\ \dfrac{(-1)^l V_1 + (-1)^{l+1} V_0}{l\pi} + i\dfrac{V_0 + V_1}{l\pi} & l = 8k+6 \end{cases} \tag{2.16}$$

where again only specific l-values contribute to the Fourier series: all those c_l for which l does not satisfy $l = 8k+2$ or $l = 8k+6$ are null. In particular, only even modes can be excited this way.
Substituting the expressions for V_0 and V_1 of (2.15) we obtain

$$\sigma = +1: \qquad c_l(t) = \begin{cases} \left(\dfrac{V_d \exp(-i\pi/2)}{\pi(8k+2)}\right) e^{+i\omega_d t} & l = 8k+2 \\ \left(\dfrac{V_d \exp(+i\pi/2)}{\pi(8k+6)}\right) e^{-i\omega_d t} & l = 8k+6 \end{cases} \tag{2.17}$$

$$\sigma = -1: \qquad c_l(t) = \begin{cases} \left(\dfrac{V_d \exp(-i\pi/2)}{\pi(8k+2)}\right) e^{-i\omega_d t} & l = 8k+2 \\ \left(\dfrac{V_d \exp(+i\pi/2)}{\pi(8k+6)}\right) e^{+i\omega_d t} & l = 8k+6 \end{cases} \tag{2.18}$$

Applying the Laplace transform, we obtain the same as (2.11), with the $l(k)$ values of this wall geometry

$$\sigma = +1: \qquad c_l(s) = \begin{cases} \dfrac{K}{s - i\omega_d} & l = 8k+2 \\ \dfrac{K'}{s + i\omega_d} & l = 8k+6 \end{cases} \tag{2.19}$$

$$\sigma = -1: \qquad c_l(s) = \begin{cases} \dfrac{L}{s + i\omega_d} & l = 8k+2 \\ \dfrac{L'}{s - i\omega_d} & l = 8k+6 \end{cases} \tag{2.20}$$

L and L' being constants. Now, let us consider each case separately, using the expression for the potential perturbation on the plasma surface (2.3), and we apply the inverse Laplace transform in time:

$$\sigma = +1: \quad \delta\phi(R_p, \theta, t) = \begin{cases} L\left(\dfrac{R_p}{R_w}\right)^l \left(\dfrac{\omega_l - l\omega_{E\times B}}{\omega_l + \omega_d}\right) \exp(-i\omega_l t - il\theta) + & l = 8k+2 \\ \quad + \left(\dfrac{\omega_l + l\omega_{E\times B}}{\omega_l + \omega_d}\right) \exp(i\omega_d t - il\theta) & \\ L'\left(\dfrac{R_p}{R_w}\right)^l \left(\dfrac{\omega_l - l\omega_{E\times B}}{\omega_l - \omega_d}\right) \exp(-i\omega_l t - il\theta) + & l = 8k+6 \\ \quad + \left(\dfrac{\omega_l + l\omega_{E\times B}}{\omega_l - \omega_d}\right) \exp(-i\omega_d t - il\theta) & \end{cases} \tag{2.21}$$

(2.21) has the same form of (2.12): for the $\sigma = +1$ case, there are poles only if $\omega_d = \omega_l$ and $l = 8k+6$. In this case, the potential perturbation on the plasma surface is

$$\delta\phi(r = R_p, \theta, t) = L'\left(\frac{R_p}{R_w}\right)^l (1 + i(l\omega_{E\times B} - \omega_l)t) \exp(i(l\theta - \omega_l t)) \tag{2.22}$$

Configuration	V_m	σ=-1	σ=+1
rotating dipole	$V_d \cos(\omega_d t + \sigma m \pi/4)$	$l = 8k + 1$	$l = 8k + 7$
rotating quadrupole	$V_d \cos(\omega_d t + \sigma m \pi/2)$	$l = 8k + 2$	$l = 8k + 6$
rotating sextupole	$V_d \cos(\omega_d t + \sigma m 3\pi/4)$	$l = 8k + 3$	$l = 8k + 5$
non rotating octupole	$V_d \cos(\omega_d t + \sigma m \pi)$	$l = 8k + 4$	$l = 8k + 4$

Table 2.1: Excitable diocotron modes for different configurations of an electric rotating field for an electrode with 8 azimuthal sectors.

that is to say, when the external drive frequency matches the l^{th} diocotron mode frequency, the l^{th} diocotron mode, that has frequency ω_l, is excited, and its amplitude envelope grows linearly in time as long as the drive is applied. Only those modes with $l = 8k + 6$ can be excited with this rotating electric field configuration.
While, if $\sigma = -1$, with the same calculations, we can see that only the $l = 8k + 2$ diocotron modes are excited, and they grow linearly in time.
These results can be easily generalized for other potential configurations feasible with an 8 sectors electrode like a rotating dipole. The mathematical procedure and the physical considerations are the same, what differs between the several cases are the Fourier coefficients c_l and consequently the number of diocotron modes excitable, that depend on the conditions on $l = l(k), \quad k \in \mathbb{Z}$. In the table 2.1, the excitable diocotron modes for various configuration of a rotating electric field with an 8 sectors electrode.

CHAPTER 3

Trivelpiece-Gould modes

When the plasma equilibrium is perturbed, the plasma exhibits collective modes of oscillation. The focus is on linear electrostatic plasma modes, since electromagnetic corrections are typically negligible in experimental regimes. After the definition of plasma dielectric tensor, a general theory for plasma modes on a pure electron plasma column in a Penning-Malmberg trap is developed [27] [28] [29] [30]. Among these modes, particularly relevant, because easily excited even from thermal noise, are the Trivelpiece-Gould (TG) modes [31], simply defined as plasma modes on a finite length plasma column. Their dispersion relationship is calculated for typical experimental regimes. Physical quantities are in CGS system units.

3.1 Plasma dielectric tensor

Let's consider a cold nonneutral plasma perturbed away from its equilibrium state. Considering small amplitude oscillations we can write:

$$\begin{cases} n(\mathbf{r},t) = n_0(r,t) + \delta n(\mathbf{r}) \exp(-i\omega t) \\ \mathbf{v}(\mathbf{r},t) = \delta \mathbf{v}(\mathbf{r}) \exp(-i\omega t) \\ \phi(\mathbf{r},t) = \phi_0(r,z) + \delta\phi(\mathbf{r}) \exp(-i\omega t) \end{cases} \tag{3.1}$$

where n_0 is the equilibrium density, $\mathbf{v}(\mathbf{r},t)$ is the fluid velocity and ϕ_0 is the equilibrium potential. $\omega/2\pi$ is the frequency oscillation of the perturbation Doppler-shifted with respect to the laboratory frame, that is to say in the plasma *rotating frame*.
In fluid theory, the momentum conservation (Euler equation) for a nonneutral electron plasma yields:

$$m_e n \left(\frac{\partial \mathbf{v}}{\partial t} + \mathbf{v} \cdot \nabla \mathbf{v} \right) = -en \left(-\nabla\phi + \frac{\mathbf{v} \times \mathbf{B}}{c} \right) - \nabla p \tag{3.2}$$

where p is the plasma thermal pressure.
Substituting eq.3.1 in eq.3.2, to the linear order in the perturbed quantities we have

$$-i\omega\delta\mathbf{v} = -\frac{e}{m}\nabla\delta\phi + \Omega_v \delta\mathbf{v} \times \hat{z} \tag{3.3}$$

where $\Omega_v \equiv \Omega_c - 2\omega_{E\times B}$ is the vortex frequency, that is to say the cyclotron frequency as seen in the rotating frame. p has been neglected because we are considering cold plasma, thus the thermal pressure can be ignored. The convective term $\mathbf{v} \cdot \nabla \mathbf{v}$ has been neglected

too because it is non-linear in δu.
Eq.3.3 is linear in $\delta\mathbf{u}$ so it can be easily solved:

$$\delta\mathbf{v} = -\frac{\sigma\cdot\nabla\delta\phi}{en_0} \tag{3.4}$$

where σ is the conductivity tensor for the plasma

$$\underline{\sigma} = i\begin{pmatrix}\sigma_1 & i\sigma_2 & 0\\ -i\sigma_2 & \sigma_1 & 0\\ 0 & 0 & \sigma_3\end{pmatrix} \tag{3.5}$$

with

$$\sigma_1 = \frac{\omega_p^2\omega}{4\pi(\omega^2-\Omega_v^2)} \qquad \sigma_2 = \frac{\omega_p^2\Omega_v}{4\pi(\omega^2-\Omega_v^2)} \qquad \sigma_3 = \frac{\omega_p^2}{4\pi\omega} \tag{3.6}$$

The conductivity tensor σ expresses the linear relationship between the perturbed electric field $-\nabla\delta\phi$ and the perturbed current density $en_0\delta\mathbf{v}$.
If we combine eq.3.1 and the continuity equation 1.12, at first order in the perturbation terms we have

$$-i\omega\delta n + \nabla\cdot(n_0\delta\mathbf{v}) = 0 \tag{3.7}$$

Now, relating the perturbed density with the perturbed potential via linearized Poisson equation

$$\nabla^2\delta\phi = 4\pi\delta n \tag{3.8}$$

and substituting (3.4) in the linearized continuity equation (3.7) we obtain the wave equation

$$\nabla\cdot\underline{\epsilon}\cdot\nabla\delta\phi = 0 \tag{3.9}$$

where we have introduced the frequency dependent plasma dielectric tensor $\underline{\epsilon}\equiv\mathbb{I}+\frac{i4\pi}{\omega}\underline{\sigma}$ ($\mathbb{I}$ is the unit tensor). More explicitly

$$\underline{\epsilon} = \begin{pmatrix}\epsilon_1 & -i\epsilon_2 & 0\\ i\epsilon_1 & \epsilon_2 & 0\\ 0 & 0 & \epsilon_3\end{pmatrix} \tag{3.10}$$

with

$$\epsilon_1 = 1-\frac{\omega_p^2}{\omega^2-\Omega_v} \qquad \epsilon_2 = \frac{\omega_p^2\Omega_v}{\omega(\omega^2-\Omega_v^2)} \qquad \epsilon_3 = 1-\frac{\omega_p^2}{\omega^2} \tag{3.11}$$

The dielectric tensor is not isotropic because the applied magnetic field and plasma rotation break plasma isotropy. Eq. (3.9) contains all the information about the electrostatic cold plasma modes of oscillation, and shows that magnetized plasma is a dielectric medium: a normal perturbation mode causes a charge motion that polarizes the plasma producing an electric displacement $\mathbf{D} = -\underline{\epsilon}\cdot\nabla\delta\phi$.

3.2 Trivelpiece-Gould (TG) modes in a cylindrical plasma

In a Penning trap, the plasma is not an infinite and homogeneous medium: waves reflect from the plasma edges, setting up normal modes of oscillation. For instance, for a long plasma column of length L the modes have axial wavenumber k_z that roughly satisfy

$k_z = m_z\pi/L$, with m_z integer number. The lowest order axial-mode, $m_z = 0$ corresponds to a potential perturbation with no z-dependence within the plasma, the $m_z = 1$ mode has a single axial node in the center of the plasma (one-half wavelength in the plasma), and so on...
Plasma modes can be determined analytically for the typical cylindrical geometry of a Penning-Malmberg trap. For a long uniform density plasma column of radius R_p and length L running from $z = 0$ to $z = L$, the dielectric tensor $\underline{\epsilon}$ is uniform in space. Hence, re-writing eq.(3.9) in cylindrical coordinates

$$\epsilon_1 \left(\frac{1}{r}\frac{\partial}{\partial r} r \frac{\partial \delta\phi}{\partial r} + \frac{1}{r^2}\frac{\partial^2 \delta\phi}{\partial \theta^2} \right) + \epsilon_3 \frac{\partial^2 \delta\phi}{\partial z^2} = 0 \tag{3.12}$$

The differential eq.(3.12) is separable, and can be analytically solved:

$$\delta\phi(\mathbf{r}, t) = A J_{m_\theta}(k_\perp) \cos(k_z z) \exp\left(i m_\theta - i\omega t\right) \qquad r < R_p \tag{3.13}$$

where A is a coefficient to be found and m_θ, non-negative integer number, is the azimuthal mode number. k_z is the component of the wave vector parallel to $\mathbf{B}$ and $k_\perp = \sqrt{k_x^2 + k_y^2}$ is the module of the transverse wave vector $\mathbf{k}_\perp \perp k_z\hat{z}$ so that $\mathbf{k} = (\mathbf{k}_\perp, k_z)$. J_{m_θ} is a Bessel function of the first kind. The cosine in the solution is chosen so that the electric field vanishes at the ends of the plasma column.
Outside the plasma, where $n_e = 0$ and therefore $\epsilon_1 = \epsilon_3 = 1$ the solution of eq.(3.12) is

$$\delta\phi(\mathbf{r}, t) = B \left(I_{m_\theta}(k_z r) K_{m_\theta}(k_z R_w) - I_{m_\theta}(k_z R_w) K_{m_\theta}(k_z r) \right) \cos(k_z z) \exp(i m_\theta \theta - i\omega t) \quad r > R_p \tag{3.14}$$

where I_{m_θ} and K_{m_θ} are Bessel functions of the second kind and B is a coefficient to be determined.
To obtain a dispersion relation $\omega = \omega(k)$ for our plasma modes, we have to find A and B. If we impose the potential continuity between outside and inside the plasma

$$\phi(R_p^-) = \phi(R_p^+) \tag{3.15}$$

and we impose the continuity of normal component of the electric displacement $\underline{D}$ across the plasma surface

$$\hat{r} \cdot (\underline{\epsilon} \cdot \nabla\delta\phi)|_{R_p^-} = \hat{r} \cdot (\underline{\epsilon} \cdot \nabla\delta\phi)|_{R_p^+} \tag{3.16}$$

by substituting the expressions found for $\delta\phi$ (3.13) and (3.14) in both (3.16) and (3.15) we can determine A and B and finally obtain

$$\begin{aligned} &\epsilon_1 \frac{\partial}{\partial R_p} J_{m_\theta}(k_\perp R_p) + \epsilon_2 \frac{m_\theta}{R_p} J_{m_\theta}(k_\perp R_p) \\ &= J_{m_\theta}(k_\perp R_p) \frac{\dfrac{\partial}{\partial R_p} \left(I_{m_\theta}(k_z R_p) K_{m_\theta}(k_z R_w) - I_{m_\theta}(k_z R_w) K_{m_\theta}(k_z R_p) \right)}{I_{m_\theta}(k_z R_p) K_{m_\theta}(k_z R_w) - I_{m_\theta}(k_z R_w) K_{m_\theta}(k_z R_p)} \end{aligned} \tag{3.17}$$

If we neglect reflections from the plasma edges, we can write in Fourier representation the waves associated with density perturbation

$$\delta\phi(\mathbf{r}, t) = A \exp(i\mathbf{k} \cdot \mathbf{r} - i\omega t) \tag{3.18}$$

Waves of this form allow direct solution of eq.(3.9), since $\nabla\delta\phi = i\mathbf{k}\delta\phi$. Substituting (3.18) in (3.9) we obtain

$$k_\perp^2\epsilon_1 + k_z^2\epsilon_3 = 0 \tag{3.19}$$

For finite plasma length this is a useful but rough approximation that improves as the length of the column increases.
Eq. (3.17) together with (3.19) is the Trivelpiece-Gould dispersion relation. In general it yields real solutions $\omega(k)$, but without further hypothesis on the plasma quantities and geometry that simplify (3.17), solutions can be found only numerically.
Trivelpiece-Gould plasma modes are finite k plasma oscillation on the magnetized plasma column, with frequency $\omega_{TG} \sim \omega_p$. If we assume $k_z R_w << 1$ and in the strong magnetic field limit, such that $\omega_p << \Omega_v$ and therefore $\epsilon_1 = 1$, then the mode frequency follows from eq.(3.19):

$$\omega_{TG}^2 = \frac{\omega_p^2 k_z^2}{k_\perp^2 + k_z^2} \tag{3.20}$$

These TG modes are magnetized cold plasma waves with k_z and $k_\perp$ quantized by the finite plasma length and radius. We can calculate $k_\perp$ from (3.17) taking $\epsilon_1 = 1$ because of the strong magnetic field regime, and $\epsilon_2 = 0$, because we are assuming a very long plasma column, with $k_z/k_\perp << 1$

$$R_p \frac{\partial}{\partial R_p} J_{m_\theta}(k_\perp R_p) = J_{m_\theta}(k_\perp R_p) \begin{cases} -m_\theta \dfrac{1 + \left(\dfrac{R_p}{R_w}\right)^{2m_\theta}}{1 - \left(\dfrac{R_p}{R_w}\right)^{2m_\theta}} & m_\theta > 0 \\ -\dfrac{1}{\ln\left(\dfrac{R_w}{R_p}\right)} & m_\theta = 0 \end{cases} \tag{3.21}$$

For fixed k_z and m_θ there are multiple solutions for (3.21), corresponding to waves with different radial nodes within the plasma column. For example, for $m_\theta = 0$ there is a solution with 0 radial nodes

$$k_\perp r_p \sim \sqrt{\frac{2}{\ln\left(R_w/R_p\right)}} \quad R_p << R_w \tag{3.22}$$

The solutions with more nodes roughly satisfy $J_1(k_\perp R_p) = 0$ so that

$$k_\perp = j_{1,n}/R_p \quad n = 1, 2, 3 \ldots \tag{3.23}$$

where $j_{m_\theta,n}$ is the n-th zero of the Bessel function $J_{m_\theta}(x)$ excluding the origin.
For $m_\theta > 0$, if $R_w >> R_p$ the right hand side of eq.(3.21) can be approximated as $-m_\theta J_{m_\theta}$. Thanks to Bessel functions identities, we can rewrite

$$k_\perp = j_{m_\theta - 1,n}/R_p \quad n = 1, 2, 3 \ldots \tag{3.24}$$

These solutions correspond to a potential with $n-1$ radial nodes $m_r = n - 1$, that is to say, the axial fluid velocity changes sign as a function of radius. The formulae in this section, while useful in their regime of validity, are only approximate, but considering the wave numbers, we can affirm that higher m_z results in higher mode frequency; higher m_θ results in lower Doppler-shifted mode frequency $\omega_{TG} - m_\theta\omega_{E\times B}$; higher radial mode

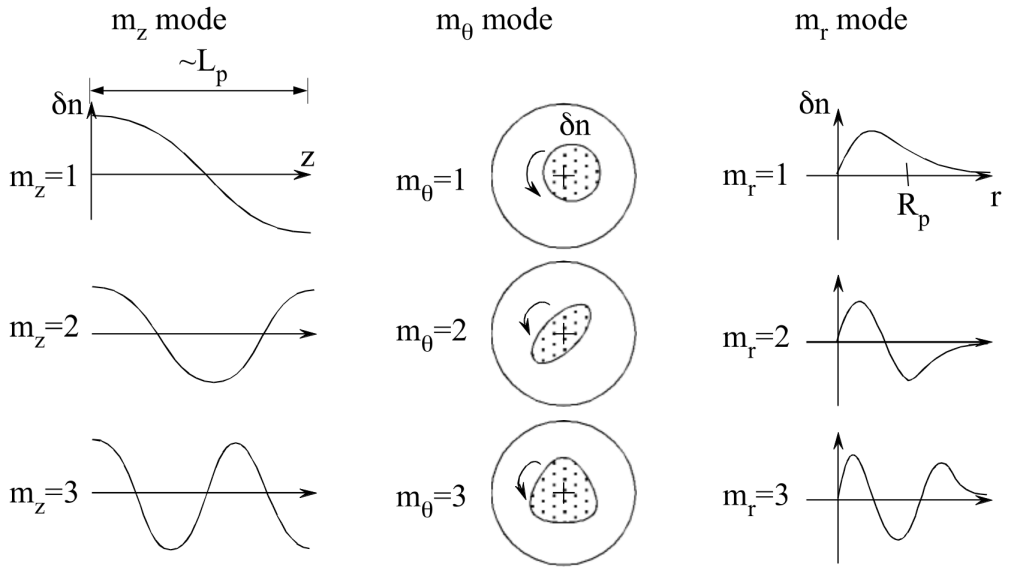

Figure 3.1: Graphic representation of the three wave numbers for a TG mode on a cylindrical plasma column.

number m_r results in lower mode frequency. In fig. 3.1 a sketch of the quantum wave numbers m_z, m_θ, m_r physical meaning.

If we include the thermal pressure, not neglecting ∇p in eq.(3.2), the dispersion relation (3.19), valid for an infinite plasma length, becomes

$$\omega_{TG}^2 = \frac{\omega_p^2 k_z^2}{k_\perp^2 + k_z^2} + 3\frac{k_B T_e k_z^2}{m_e} \tag{3.25}$$

where this temperature correction assumes the density remains uniform, even at finite T. The thermal pressure adds a small correction linear in T, that always increases the mode frequency.
For trapped plasmas, with finite length L where the TG waves behave as a standing wave with quantized wavelength $k_z = \dfrac{m_z \pi}{L}$, in the limit of a long column $k_z/k_\perp << 1$ and $R_p << L$, it can be shown that the frequency of the TG waves has an additional positive term $\propto (T^1)$.
In these approximations, that reproduce the typical experimental regime, the TG dispersion relation does not depend directly from the magnetic field B, while the diocotron mode frequency is $\omega_l \propto B^{-1}$. This is because while the diocotron mode are perturbations on the $\mathbf{E} \times \mathbf{B}$ drift equilibrium of the plasma column, the TG modes are just general potential perturbations of a nonneutral plasma equilibrium profile (n_0, ϕ_0), that does not necessarily involve the radial confinement through a magnetic field (even though, of course, the theory here presented has been developed considering a plasma in a cylindrical Penning trap). Although there is no explicit dependence $\omega_{TG} \not\propto (B)$ the magnetic field plays a relevant role in the TG modes frequency in the usual case of a plasma confined in a Penning-Malmberg trap: at high magnetic field, the cyclotron radiation

emission becomes the most relevant cooling mechanism for the plasma electrons. As the temperature decreases, so does accordingly ω_{TG}, see eq.(3.25).

It is interesting to notice that if we take the limit for $k_0 \to 0$ in (3.21), for a highly magnetized plasma with a flat profile (1.1) we obtain exactly (1.24).

Part II

Experimental devices: Eltrap and CamV

CHAPTER 4

Eltrap

Eltrap (ELectron TRAP) is the Penning Malmberg trap located in the plasma physics laboratory of the University of Milan. It has been operating since the year 2003 to perform experiments on magnetized pure electron plasma columns, such as, to name just a few, RadioFrequency generation of the plasma and its dynamics structures under continuous RF excitation [32], fluid instabilities and turbulence [33], coherent structure and collective behavior [34].

4.1 Trap geometry and main features

Eltrap consists of a stack of 12 hollow coaxial cylindrical electrodes, all with inner diameter of $2R_W = 90$ mm. The length of the "C" electrodes is $L_C = 90$ mm, while the length of the "S" electrodes is $L_S = 150$ mm, and the separation distance between each electrode and the adjacent one is 1 mm. The "C" electrodes are fully cylindrical, while $S2$, $S4$ and $S8$ are azimuthally segmented in 2,4, and 8 sectors respectively. Between C8 and the phosphor screen the "SH" electrode is always grounded to shield the phosphor screen high voltage. Shown in fig. 4.1 is a schematic of the trap.
All the electrodes are made in oxygen-free high-conductivity (OFHC) copper, with $S8$ having an additional golden layer coating. They are all mounted, independently of each other, on an aluminum bar held at ground, with 4 Macor rings between each of the electrodes and the aluminum bar, to guarantee the electrical insulation of the trap, see fig. 4.2.

The longitudinal confinement is obtained by applying a negative voltage, usually $V_C \sim -100$ V, on two of anyone of the "C" electrodes. The negative voltage is provided by two high voltage generators, that can reach up to -800V. The two voltage generators are controlled by a fast, low noise, high voltage switch with MOSFET transistor,

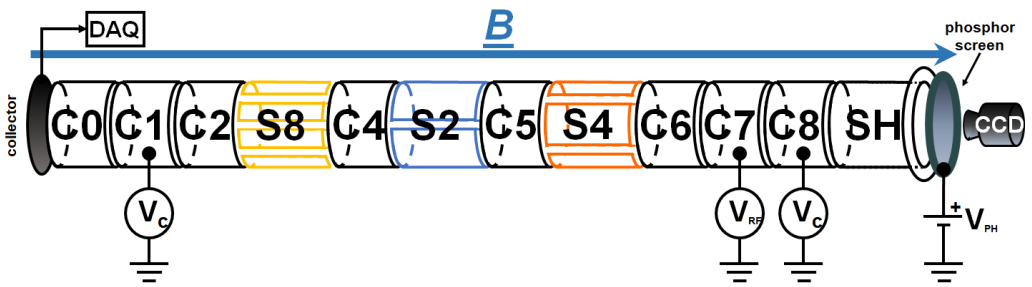

Figure 4.1: Eltrap electrode scheme.

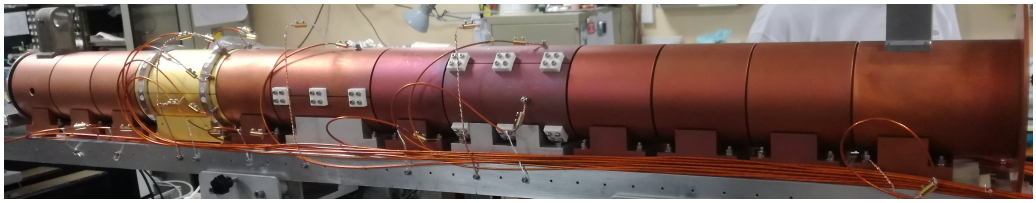

Figure 4.2: The electrode stack: from left to right, C0 to the shield electrode. The golden electrode is S8, the one divided in eight azimuthal sectors.

designed for trap applications. With our coupling capacity $C \sim 100$ pF, we can switch from V_C to $V = 0$ in $\tau_{Switch} \sim 100$ ns, a time very short with respect to the plasma dynamical time scales, characterized by a longitudinal bounce frequency $\nu_{bounce} \sim$ MHz.
The electrodes stack and the bar are inside a stainless steel vacuum chamber, with inner diameter $\phi = 25$ cm and length $L = 175$ cm. The vacuum chamber is pumped to the desired pressure with a sequence of three pumps: first a scroll pump to reach a pressure level of $P \sim 10^{-3}$ mbar, second a turbomolecular pump for pressure level down to $P \sim 10^{-8}$ mbar and third and last an ion pump, working at $V = 5$ kV, to reach the $P \sim 10^{-9}$ mbar level. Hence the trap is always kept at $P \sim 10^{-9}$ mbar, the so called Ultra High Vacuum (UHV) regime. The pressure inside the vacuum chamber is measured with a cold cathode gauge for $P > 10^{-8}$ mbar, while for $P < 10^{-8}$ mbar we rely on the characteristic current-pressure calibration curve of the ion pump.
The trap magnetic field is provided by a solenoid coil, 150 cm long and with an inner diameter $\phi = 32$ cm. The solenoid coil consists of three helical trifilar winding layers. The nine conductors are water cooled in parallel and electrically connected in series. Moreover, the solenoid is enclosed in a soft iron cage that acts as a shield against the Earth's magnetic field. If needed, four dipole correcting coils compensate for errors in the main solenoid winding, allowing adjustment of any misalignment between the magnetic field and the trap longitudinal axis. These features grant a high spatial homogeneity of the magnetic field for the whole trap length. The relationship between the solenoid current I and the magnetic field in the trap B is linear:

$$B(T) = 0.2T\frac{I}{I_{max}} \tag{4.1}$$

The maximum current is $I_{max} = 600$ A, corresponding to the maximum achievable magnetic field $B = 0.2$ T. Even though the trap can be equipped with an external electron source, a thermocathode for example, as it has been for several years [35], in the present configuration Eltrap does not have an external source. The plasma is created through the RadioFrequency (RF) generation technique [36], [37], [38], [39]. In UHV regime, if we apply to one of the electrode a radiofrequency signal, usually $\nu_{RF} \sim$ MHz, $V_{RF} \sim$ V, for a time $t_{RF} \sim$ s, we obtain a low density, $n_e \sim 10^6$ cm^{-3}, electron plasma column. This mechanism is based on the resonant excitation of some of the free electrons already present in the trap, that through the continuous excitation provided by the RF signal, acquire energy sufficient to ionize the residual background gas. The plasma column total charge is $Q \sim -10^2$ pC and the electrons temperature, once the RF signal is off and the plasma reaches the thermal equilibrium is $T_e \sim$ eV. The positive ions are mostly removed by the electrostatic potential applied on the confinement electrodes, leaving in the trap a positive ions to electrons ratio of $\frac{n_i}{n_e} \sim 10\%$. The RF generation technique, although

mastered and well explored in its experimental parameters, still lacks of a complete theoretical explanation.

4.2 Diagnostics

We employ two kinds of diagnostics in Eltrap: an optical diagnostic, that requires plasma ejection, and an electrostatic diagnostic, that does not perturb the plasma. The optical diagnostic consists of a Charge-Coupled Device (CCD) camera coupled to a phosphor screen located at one end of the trap: when the plasma is ejected on this side of the trap, the phosphor screen, kept at high voltage, emits luminosity proportional to the number of electrons collected per unit area, and the luminosity is then recorded by the CCD camera. This allows to reconstruct a 2D (r, θ) density profile. The phosphor screen has an active area of diameter 10.4 mm$< \phi_{PH} < 10.2$ mm, enough to cover the whole trap area, and it is a P43 phosphor screen emitting green light, $\lambda = 513$ nm, the wavelength with the efficiency peak for this kind of screen. The typical luminescence decay time is $\tau \sim 1$ ms, and there is no accessory aluminum reflective layer on top of the phosphor coating. The phosphor screen works with a stable high voltage $V_{Ph} \sim 8$kV and to ensure electrical insulation, is mounted with three Macor supports on an aluminum ring, surrounded by an additional aluminum shield. In fig. 4.3 the phosphor screen mounted on its support.

The CCD camera has a maximum resolution of 1344 pixel $\times$ 1024 pixel, corresponding to 0.4mm/pixel resolution and, depending on the phosphor screen luminosity, we can chose a 1×1 (maximum resolution), 2×2 or 4×4 pixel binning. A low charge plasma gives a faint luminosity, so we need a 4×4 binning, while a high charge plasma requires a 1×1 binning to avoid image saturation. Given the luminescence decay time of the phosphor screen, the exposure time to collect a plasma profile is no longer then 1 ms.
As a non destructive and non perturbative diagnostic, we can measure the current signal the plasma induces on any of the electrodes when subject, for example, to a diocotron mode. With our typical plasma parameters, $L_P \sim 80$ cm, $\frac{R_p}{R_W} \sim 0.3$, $n_e \sim 10^6$ cm^{-3}, $B \sim 0.1$ T we have an induced current $i \sim$ nA. With our oscilloscope, in order to properly resolve a signal and distinguish it from the noise level, we need at least a 10 mV signal. Moreover, to not perturb the plasma, we have to avoid energy dissipation due to the resistive wall instability, and so we have to couple our sectors with a very low $\sim \Omega$ or a very high MΩ impedance. We can satisfy both these conditions with our transimpedance amplifier, that does not have a resistance in input, and whose gain in the 1 kHz$< \nu <$100 kHz bandwidth is $G = 10^6 V/A$.
In addition to these two diagnostics there is a collector plate on the end of the trap opposite to the optical diagnostic side, that we can use to measure the total plasma charge, see appendix A. Measuring the total plasma charge through the collector also allows calibration of the optical diagnostic, since we can evaluate the ratio $\frac{Electric\,charge}{Luminosity}$.
Shown in fig. 4.4 is the charge collector.

In the table 4.1, a list of some typical plasma parameters in Eltrap is given.

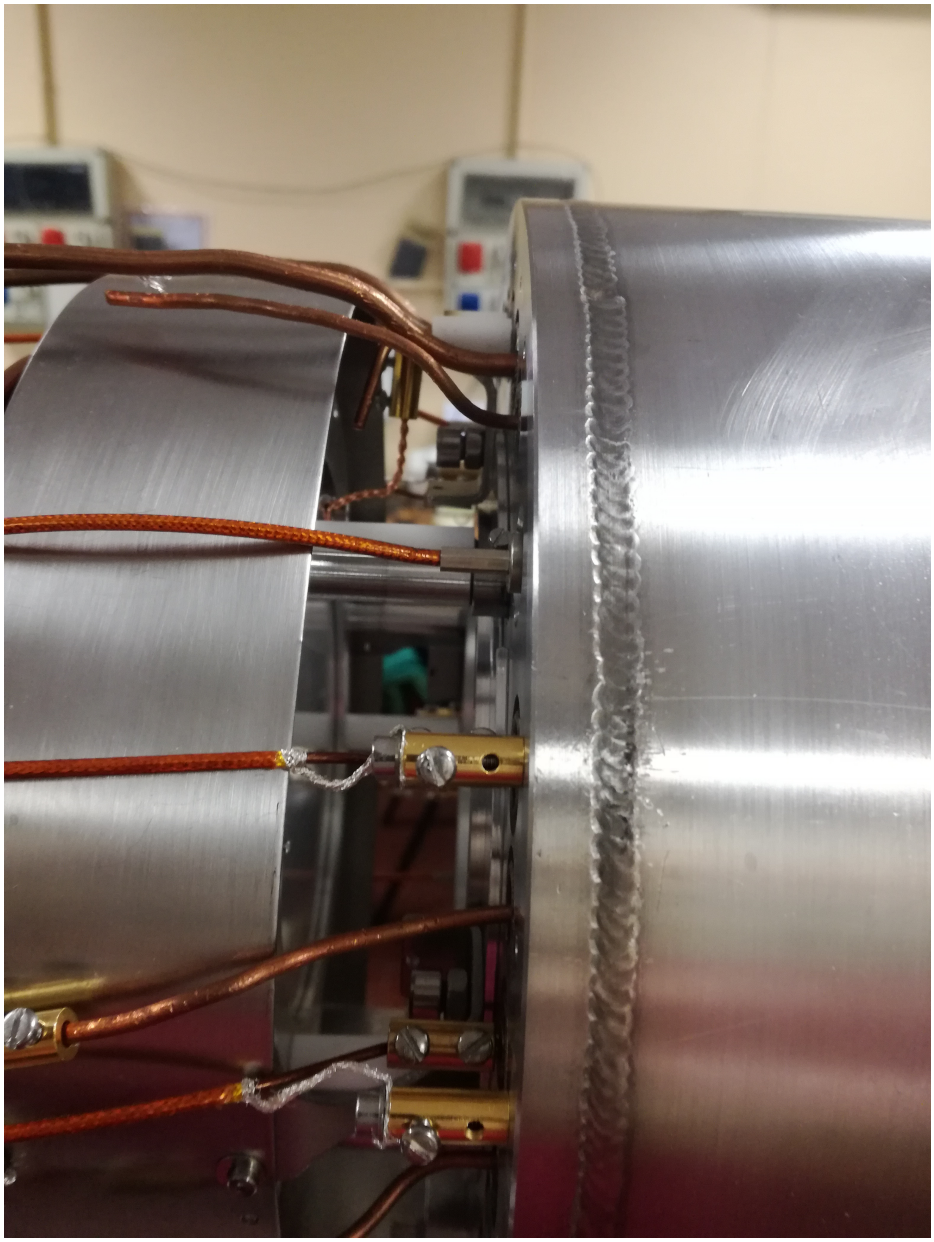

Figure 4.3: The phosphor screen, mounted in its position, can be spotted surrounded by an aluminum sheet. Also the three Macor insulator supports can be seen. Except for S8 and the charge collector, all the wires for the electrostatic diagnostic come out of the trap on this side, so it is very important to shield any disruptive high voltage.

Figure 4.4: Eltrap charge collector. Three Macor supports provide the electrical insulation from the aluminum bar (ground potential). Between the C0 electrode and the aluminum bar, two Macor rings can be spotted. The metal piece over C0 was used as support for the AC wires, when Eltrap is operated with a thermocathode.

Parameters	Symbol and units	Typical value
Magnetic field	B(T)	0.1
Temperature	T_e(eV)	3
Density	n_e(cm^{-3})	10^6
Length	L_p(cm)	90
Radius	R_p(cm)	2.25
	R_p/R_W	0.5
Debye length	λ_D(cm)	0.8
Collisionality	ν_{ee}(Hz)	10^2
$E \times B$ drift	$\nu_{E\times B}$(Hz)	10^3
Longitudinal bounce	ν_b(Hz)	10^6
Plasma frequency	ω_p(Hz)	10^7
Cyclotron frequency	Ω_C(Hz)	10^9
Plasma potential	Φ_p(V)	-10(at $r = 0$)
Confinement potential	V_C (V)	-160

Table 4.1: Typical experimental parameters for electron plasmas in Eltrap.

CHAPTER 5

CamV

CamV is one of the Penning Malmberg traps of the Nonneutral Plasma group at University of California, San Diego (UCSD)[40], [41]. It is devoted to the study of magnetized pure electron plasma physics. "Cam" stands for camera, referring to the CCD camera diagnostic, and "V" stands for "Voltage" referring to the voltage confinement applied on the electrodes. The apparatus is ideally suited to studies of 2D fluid instabilities [42], turbulence and relaxations [43], and, more recently, multi-species plasma dynamics with single sign of charge [44].

5.1 Trap geometry and main features

CamV consists of a stack of 10 hollow coaxial cylindrical electrodes, with inner diameter $2R_W = 70$ mm. The "L" electrode is 140 mm long, the "G" and "S" electrodes are 70 mm long, and the "H" electrodes are 35 mm long. The "L","G" and "H" electrodes are fully cylindrical, while $S4$ and $S7$ are divided in 4 and 8 azimuthal sections respectively. $S4$ has $60°$ sectors, with $30°$ sections of the frame of electrode 4 (outer frame), while $S7$ has $25°$ sectors, with $20°$ sections of the frame of electrode 7 (outer frame). All the electrodes are made of oxygen-free high-thermal-conductivity (OFHC) copper and are electroplated with a layer of gold to prevent oxidation. The "A" electrodes can be used as a tool the measure the plasma energy, but in our experiments, they are all constantly kept at $V_A = +100$ V, to help accelerate the electrons toward the phosphor screen. In fig. 5.1 a schematic of the CamV apparatus is shown.

The confinement potential, $V_C = -100$ V, is applied on any two of any of the fully cylindrical electrodes. When the plasma is injected, the confinement electrode closer to the source is grounded for at least 500 μs allowing a plasma column to form in the confinement region, and then the plasma is trapped by ramping the grounded confinement

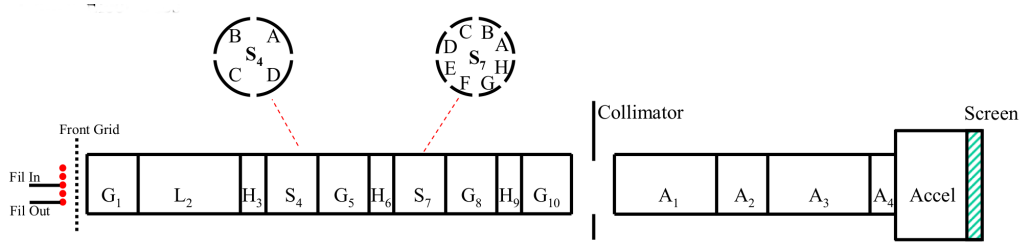

Figure 5.1: A schematic of the CamV apparatus. From left to right, the thermocathode, the electrode stack, the energy analyzer section ("A" sectors) and the optical diagnostic, to the far right.

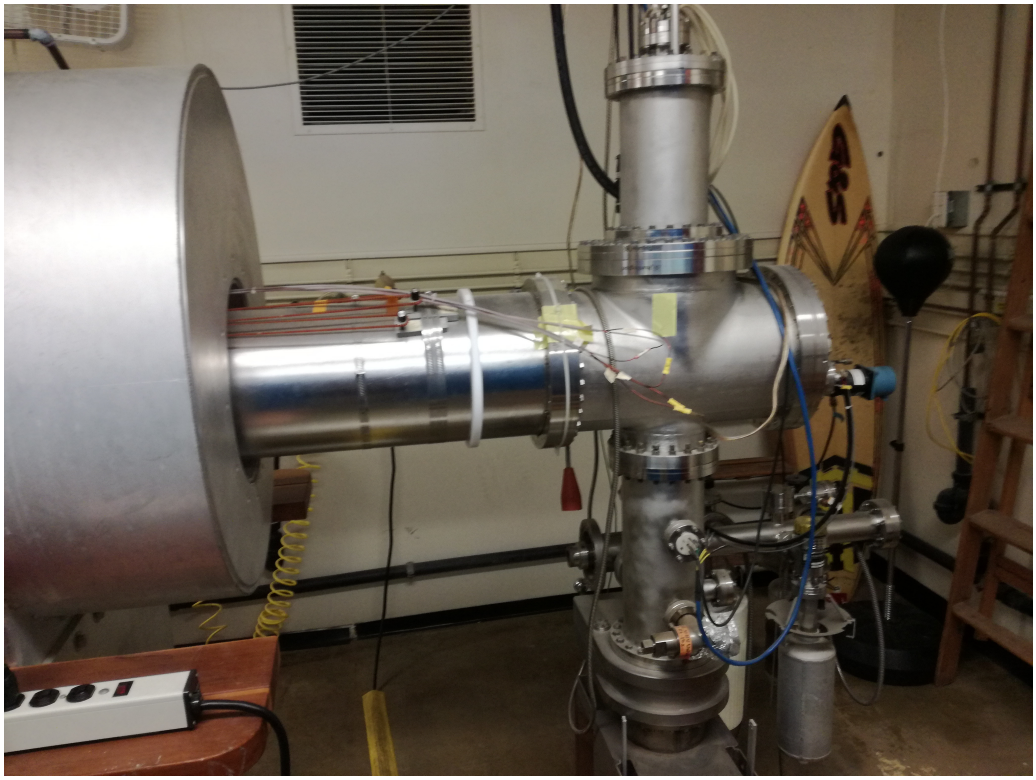

Figure 5.2: Pumping system of CamV. The top pump is a Ti pump, while the bottom pump is a diode pump. On the left side, we can see the liquid helium dewar, and its bore, where the vacuum vessel lies.

electrode back to $V_C = -100$ V in ~ 2 μs.
The trap and the source are constantly kept in Ultra High Vacuum (UHV) pressure regime, at $P \sim 10^{-10}$ mbar, thanks to an ion diode pump, as can be seen in fig. 5.2. The pressure inside the vacuum vessel is measured with a cold cathode gauge.

The magnetic field is provided by a superconducting solenoid: the maximum achievable longitudinal magnetic field is $B_z = 2$ T. Additional B_x and B_y saddle coils are used to align the magnetic field axis with the axis of the cylinder. In order for the superconducting solenoid to work, it is cooled down to $T = 4$ K with liquid Helium. The liquid helium dewar, where the solenoid lies, is surrounded by a liquid Nitrogen ($T = 77$ K) shell to slow down the liquid helium heating. With a full liquid nitrogen shell and the dewar at room temperature, 250 l of liquid helium provide 8 days of working time, before it completely evaporates and the superconducting magnet starts heating, losing the superconductive regime. The vacuum chamber resides inside a room temperature bore of the superconducting solenoid.
The source of the electrons is a hot (1800 K) spiral filament of tungsten, with impedance $Z = 1\ \Omega$. The wire is heated with an alternate current (AC) at $\nu_{AC} \sim 16$ kHz, $i \sim 11$ A. The center of the filament is independently biased, usually $V_{bias} = -30$ V with respect to the ground, but it can be adjusted in the range -5 V$< V_{bias} < -40$ V depending on

the desired plasma profile. Indeed, the negative bias accelerates the electrons inside the trapping region, and the injection process stops when the plasma potential at the center is equal to the negative bias, $V_p(r = 0) = V_{bias}$. Hence, changing V_{bias} can result in a dramatic change of the plasma profile.
Between the filament and the G1 electrode, there is a grid that can be set to a desired voltage. It is set more negative with respect to the plasma potential, usually -35 V, to prevent trapping of positive ions due to double potential wells or nested traps configuration. So, any positive ions, mostly $H2^+$ produced in the plasma volume are pulled out and collected by the grid. Otherwise, the positive ions trapped by the grounded grid and positive voltage phosphor screen (or the collector plate) can cause ion-induced instability of diocotron modes.

5.2 Diagnostics

In CamV we have two kinds of diagnostics: an optical, destructive diagnostic and an electrical, non perturbative diagnostic. On the side opposite from the filament, there is a CCD camera coupled to a phosphor screen, as shown in fig. 5.3. The phosphor screen, has a $\phi_{PH} = 10.2$ cm diameter and it emits a blue-green light (P22B). It has an additional aluminum layer 150 nm thick over the phosphor coating to block the light emitted from the filament and enhance the conductivity of the screen. At the time of the dump, the screen is biased to $V_{Ph} = 15$ kV. The CCD camera images are 1024pixel$\times$1024pixel corresponding, given the location and the focal length of the camera, to a spatial resolution of ~ 0.13 mm/pixel. Also, between the G10 and A1 electrodes, a charge collector plate is present, coupled with a RC circuit, as a tool to measure the total plasma charge. When there is an interest in measuring the total plasma charge, the collector is shifted in front of the A1 electrode, to collect the ejected plasma, but the preventing the utilization of the optical diagnostic.

As non perturbative diagnostic, we can measure the induced voltage signal on any of the electrodes. The signal goes through a ten channel, low noise, differential voltage-to-voltage amplifier, with two gain factors $\times 100$ or $\times 1000$. Sectors and amplifier are coupled with $1\ M\Omega$ impedance, to prevent the growth of the resisitive wall instability and hence any plasma perturbation.
In the table 5.1, a list of some typical plasma parameter in CamV is given.

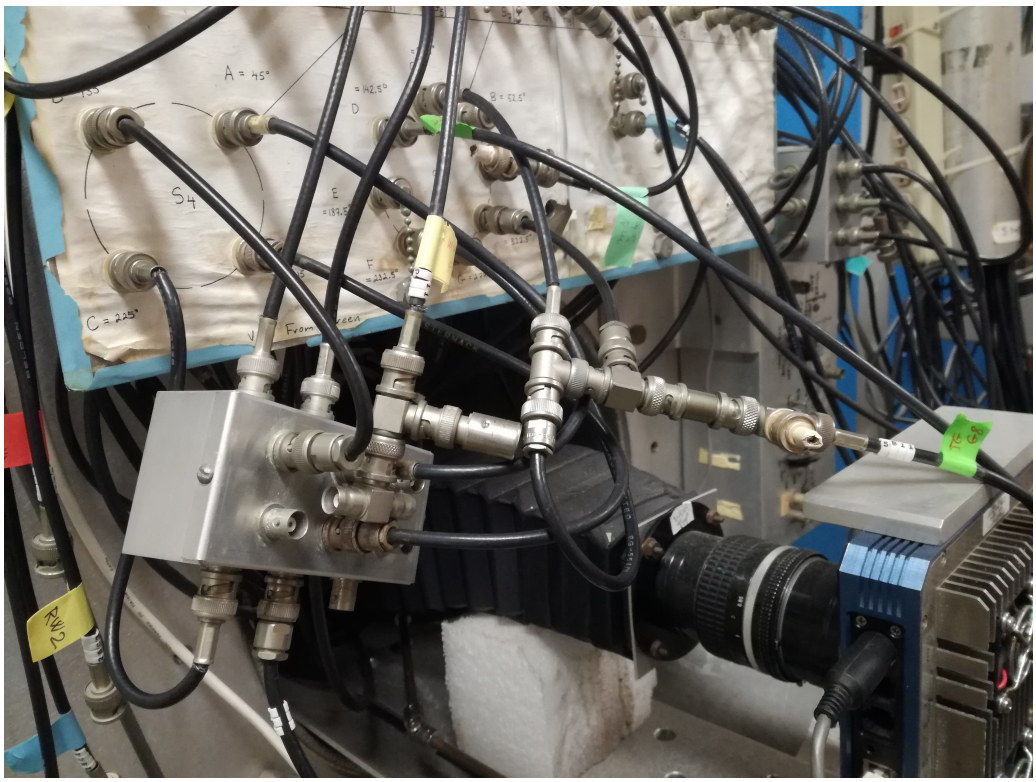

Figure 5.3: The CCD camera pointing toward the phosphor screen. We can see where the induced electrostatic signal is collected, or excited for the azimuthal sectored electrodes. Also the additional 50 Ω or 1 MΩ impedance can be noticed.

Parameters	Symbol and units	Typical value
Magnetic field	B(T)	1
Temperature	T_e(eV)	0.1
Density	n_e(cm^{-3})	10^7
Length	L_p(cm)	40
Radius	R_p(cm)	1
	R_p/R_W	0.25
Debye length	λ_D(cm)	0.2
Collisionality	ν_{ee}(Hz)	10
$E \times B$ drift	$\nu_{E\times B}$(Hz)	10^4
Longitudinal bounce	ν_b(Hz)	3*10^5
Plasma frequency	ω_p(Hz)	10^7
Cyclotron frequency	Ω_C(Hz)	10^{10}
Plasma potential	Φ_p(V)	-30(at $r = 0$)
Confinement potential	V_C(V)	-100

Table 5.1: Typical experimental parameters for electron plasmas in CamV.

Part III

Experiments on non-linear waves in nonneutral plasma

CHAPTER 6

High order diocotron mode excitation and control

In the frame of excitation and control of diocotron modes in pure electron plasmas, we have performed experimental campaigns aimed at exciting high order diocotron modes via the rotating electric field technique, applying the excitation parameters and schemes that, as described in Chapter 2, are the most efficient. We explore the space of the external drive parameters (V_d, ω_d, t_d) that is to say, we apply the potential perturbation on the wall varying, separately, the amplitude V_d, the angular frequency ω_d and the excitation time t_d, looking to maximize the amplitude of the resonantly excited diocotron mode. Moreover, as an attempt to improve our control on the modes, we apply the rotating wall technique with an autoresonant drive [45], [46], and compare the mode evolution with the drive excitations at fixed frequency. Both the optical diagnostic and the electrostatic, non perturbative diagnostic are used to measure the amplitude of the diocotron modes. The results of these parameters scans and analysis are $A(\nu_d)|_{t_{exc}}$ curves, that clearly show the resonant behavior of the phenomenon.
Although the theory presented in Chapter 2 is linear, with small potential perturbations compared to the plasma potential, as the amplitude of the excited mode grows in time, because the plasma resonates with the drive excitation, we fall out of the linear hypothesis, and enter the non-linear regime, with highly deformed plasma density profiles.
The experiments are performed with the Eltrap apparatus.

6.1 Experimental setup

For this experimental work we need to find a plasma excitation scheme that produces plasmas with the best possible shot-to-shot reproducibility, so as not to introduce other variables into our parameter space. Additionally, we need to have plasma radii that are not too big, to avoid losing electrons on the trap wall, but not too small, to better identify the diocotron modes propagating on the plasma surface: we aim at plasma columns with $R_p/R_w \sim 0.5$. For all experimental campaigns, we have kept the following generation scheme:

- Confinement between C1-C7 : confinement length of 81 cm
- $V_{confinement}$ = -160 V on both C1 and C7
- B= 1.3 kG
- RF excitation: V_{PP}= 6.6 V, $\nu_{RF} = 8.8$ MHz, $t_{RF} = 12$ s, applied on C6

To smooth the density profile and remove the $l = 1$ diocotron mode, residual from the RF generation, we manipulate the plasma as follows:

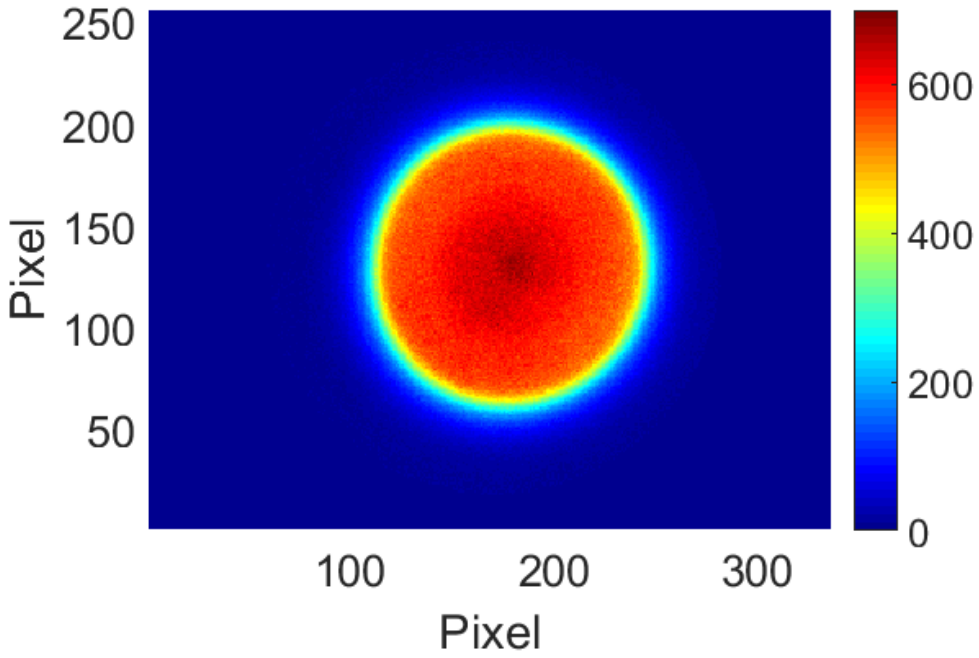

Figure 6.1: Plasma profile imaged with the CCD camera, generated with the generation procedure described in this chapter. The color scale represents the phosphor screen luminosity, uncalibrated.

- Feedback damping: for 1 s, collecting the signal on S4R and exciting on S4L
- Spike ejection: C7 is lowered to -20 V for 10 μs and then switched back to -160 V
- Feedback damping: for 0.5 s, collecting the signal on S4R and exciting on S4L

The feedback damping technique [47] [48] suppresses any residual $l = 1$ diocotron mode with an intuitive stratagem: we collect the signal induced on one of the azimuthally segmented electrodes, S4R in our case, and then we excite the collected signal, dephased by 180°, on S4L, the sector opposite to S4R. By doing this, we are applying on the plasma a force (electric field) equal in strength but opposite in direction, to the force generated (electric field) by the image charge on S4R induced by the plasma, that is to say, the $l = 1$ mode. This technique can be generalized to higher diocotron modes, with suitable signals dephasing and geometry of the sectors depending on the azimuthal symmetries of the mode.
In figs. 6.1 and 6.2 the density profile obtained with the described procedure scheme and parameters is shown, and in fig. 6.3 $\nu_{E\times B}(r)$ for the average density profile is shown.

To excite the rotating potential on the sectored electrodes, S4 and S8, we have used a two-channel wavefunction generator coupled to an eight-channel phase inverter, that can be seen in fig. 6.4. The phase inverter has four input channels and eight output channels: to each input channel correspond two adjacent ouput channels, one with the input signal without any modification (master channel), and the other one with the input signal dephased of 180° (slave channel). With this setup, it is easy to reproduce a potential distribution like (2.15). As an example, to excite an $l = 5$ diocotron mode we use a co-rotating ($\sigma = -1$) dipole for a 4 sectors electrode ($l = 4k + 1$), with $k = 1$. Hence, we set

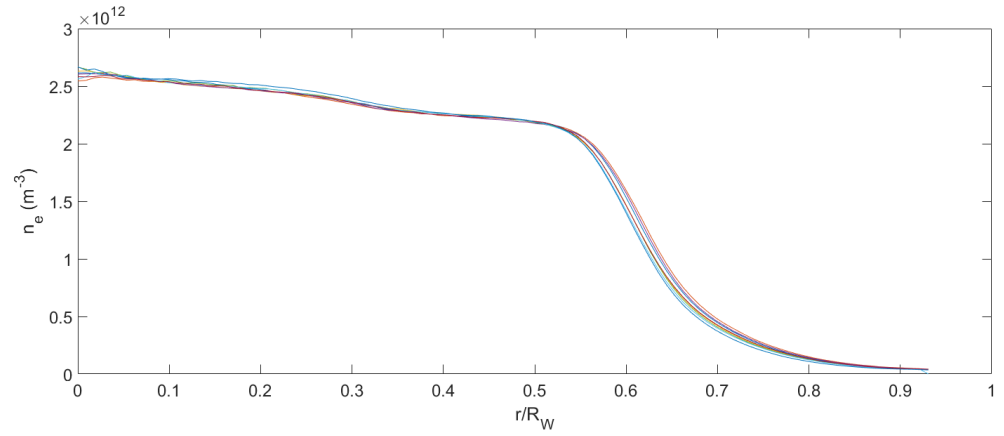

Figure 6.2: Radial plasma density profile obtained from the CCD image. Different curves correspond to the different shots profile: there is a good shot-to-shot reproducibility.

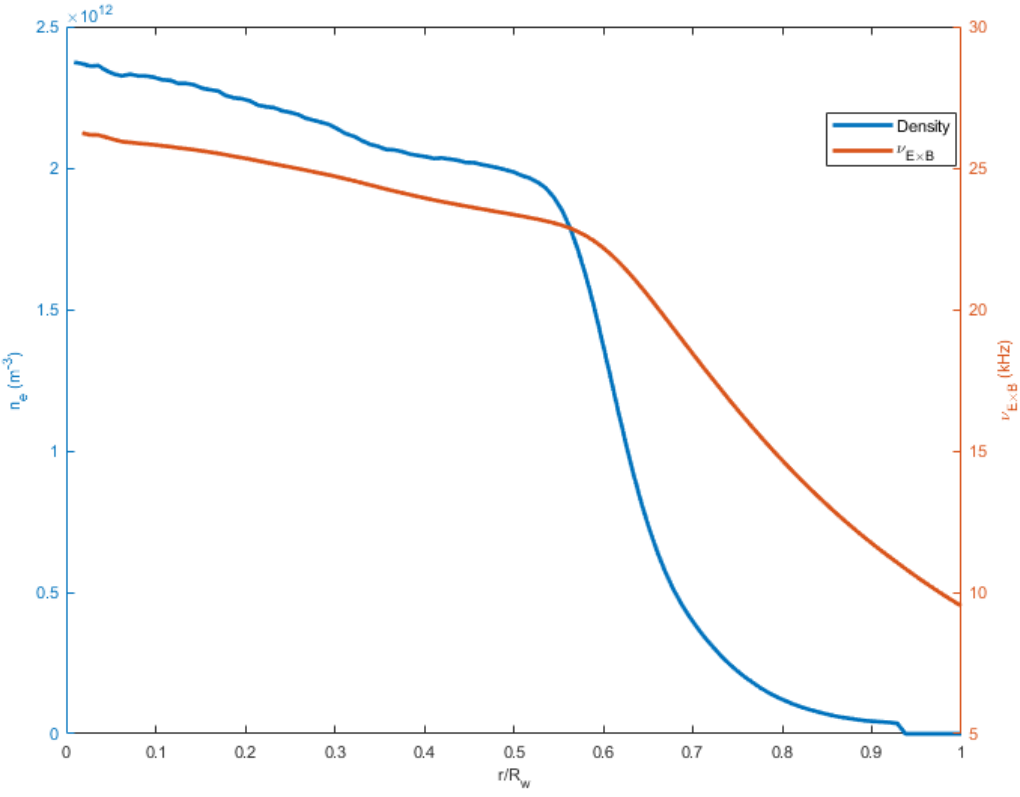

Figure 6.3: Plasma radial density profile and $\nu_{E\times B}$ radial profile. This radial profile is calculated as the average of the density profiles in fig. 6.2.

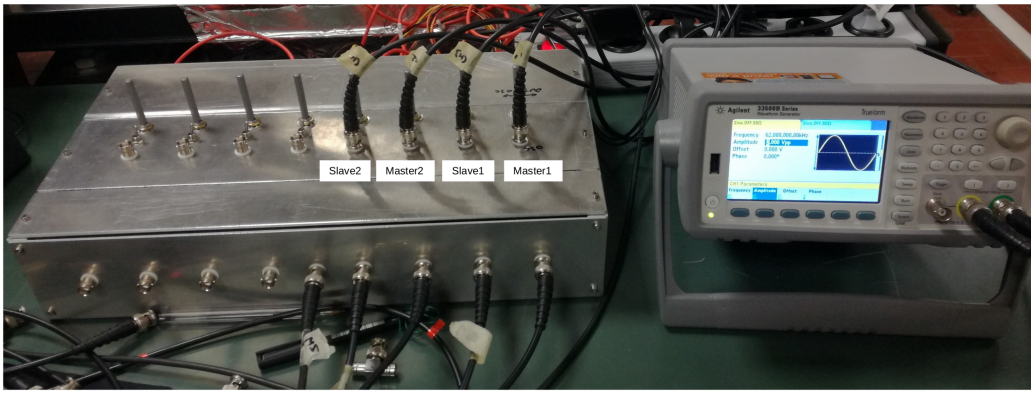

Figure 6.4: The electronics for the rotating potential excitation. To the left, the 8 channel phase inverters: labeled are two coupled master/slave (phase/counter-phase). To the right, the two channels wave generator: one of the channels is the input for the coupled master1/slave1, the other one is the input for the coupled master2/slave2.

t (s)	
0	start RF excitation
12	end RF excitation
12	start feedback damping
13	end feedback damping
13, for 10 μs	spike ejection
13 (after spike ejection)	start feedback damping
13.5	end feedback damping
13.5 for few ms or 100 ms	resonant drive excitation and ejection

Table 6.1: Experimental sequence for the plasma generation and excitation of diocotron modes with the rotating electric field.

one channel of the wavefunctions generator as $V_0 = V_d \cos(\omega_d t)$ (master1) and the other one as $V_1 = V_d \cos(\omega_d t + \pi/2) = V_1 \sin(\omega_d t)$ (master2). Then, connecting to the phase inverter, we have, from the input master1, the outputs V_0 and $V_2 = V_d \cos(\omega_d t + \pi) = -V_0$, and from the input master2, the outputs V_1 and $V_3 = V_d \sin(\omega_d t + \pi) = -V_1$, and so we have reproduced experimentally the potential in (2.15). This procedure can be easily generalized to all the feasible configurations on S4 and S8. In the table 6.1, the temporal sequence of the experiments performed.
Even though exciting the modes with the S4 or S8 electrode introduces a z-dependence, therefore breaking the 2D symmetry, the fluid analogy still holds: the $\omega_{E\times B} << \omega_b$ inequality still applies, and we can consider the fast longitudinal z-dynamics averaged over the slower (r, θ) transverse dynamics.

6.2 Experimental results: resonant excitation of high order diocotron modes via rotating electric field

We first reproduce the experimental results obtained for the l=3 mode in previous experiments, and extend them to other modes. Given the plasma profile in figs. 6.1, 6.2

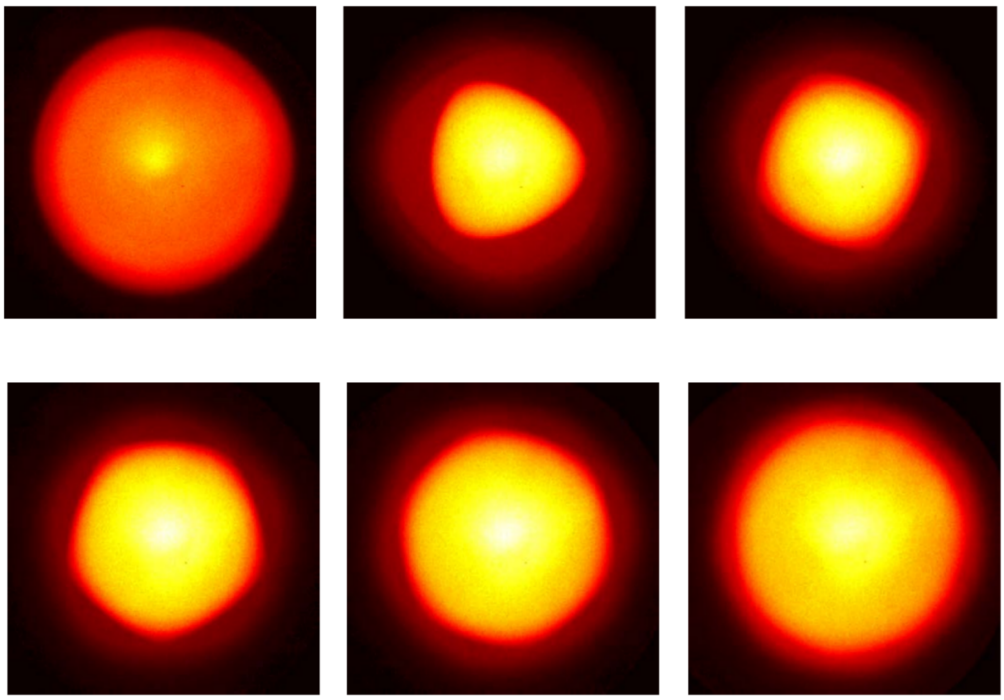

Figure 6.5: CCD image of the plasma profile obtained with the excitation in tab 6.2. The first image is the unperturbed profile. All the images are normalized to the same intensity.

we calculate the frequency of the l^{th} diocotron mode from (1.24) with $\frac{R_p}{R_w} = 0.6$ and $n_e = 2.6 \cdot 10^{12}$ m^{-3}. We perturb the plasma for a time $t_d = 100$ ms, that corresponds to $\frac{t_d}{\omega_{E\times B}^{-1}} \sim 100$, a long time compared to the diocotron mode time scale. In the table 6.2 the drive excitation parameters are given, and in fig. 6.5, the plasma profiles imaged with the optical diagnostic. The potential is applied on S8. For each mode, only one image is provided, the one with the most evident deformation, obtained by varying the excitation frequency in a range centered around the theoretical resonance frequency $\nu_l = \omega_l/2\pi$. Without further detailed analysis, fig. 6.5 and its relative drive parameters in table 6.2 show that the rotating wall technique is an efficient tool to excite high order diocotron modes: we manage to excite up to the $l = 7$ diocotron mode with only 8 azimuthal sectors, and, as expected from (2.12) and (2.21) the excitation is more efficient, in terms of amplitude of the perturbation, when the drive frequency matches the diocotron mode frequency we want to excite. In fig. 6.6 an example of drive frequency scan, with V_d and t_d fixed. We are now interested in taking some more quantitative and precise measurements to exploit all the dependencies of the resonance, and improve the control over the rotating electric field excitation. Let us collect the electrostatic signal induced by the modes on the electrodes. All the fully cylindrical electrodes cannot detect the diocotron modes, these being purely azimuthal waves. Since the S8 electrode is the one designated to the drive excitation, we are left with the S2 and S4 electrodes: we decide to collect the signal with S4T+S4B, two coupled 90° sectors at 180°, as electrostatic diagnos-

l^{th} mode	Configuration	ν_d (kHz)	V_d (V_{PP})	ν_{th} (kHz)
3	$\sigma = -1$ sextupole	61	1.7	58
4	octupole	93	3.0	85
5	$\sigma = +1$ sextupole	120	2.5	113
6	$\sigma = +1$ quadrupole	149	3.0	141
7	$\sigma = +1$ dipole	178	3.4	169

Table 6.2: Drive parameters for the diocotron modes excited in fig. 6.5. These parameters refer to highest deformation (bigger mode amplitude) obtained during the experimental drive parameters scan. The theoretical frequencies in the last column are calculated assuming a flat profile with $n_e = 2.6 * 10^{12}$ m^{-3} and $\frac{R_p}{R_w} = 0.6$.

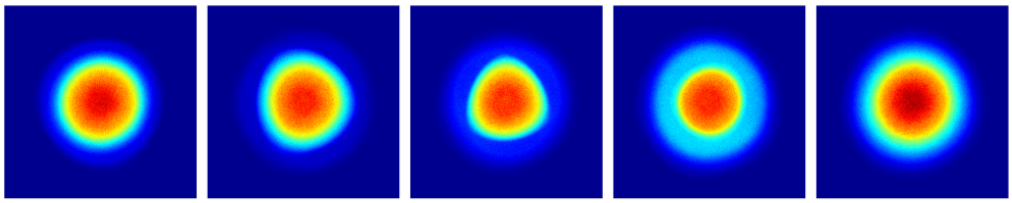

Figure 6.6: $l = 3$ diocotron mode excited with $t_d = 100$ ms and $V_d = 2$ V$_{pp}$ for several ν_d.

tic for the even modes, and S2B, one $180°$ sector, to detect the odd modes. Given the gain bandwidth of the transimpedance amplifier, we cannot detect with sufficient precision the higher order modes: the reliability of our electrostatic measurements is limited to the $l = 3$ mode and lower. The sample rate for both configurations is $5 \cdot 10^3$ kHz.
From all the spectrograms shown from here is subtracted a noise signal, detected with both the diagnostic configurations, S2B and S4B+S4T, and obtained by reproducing exactly the same experimental sequence that created the main signal but always keeping the confinement electrodes grounded, so no plasma is ever present in the trap. By doing so, we are collecting all the signals whose presence is not related to the plasma, and we are also directly measuring the drive excitation signal, so that, with the noise subtraction, we are certain that the spectral lines corresponding to the diocotron modes are actually due to the mode propagating on the plasma surface and we are not recording the drive itself. The noise removal is made by subtracting the intensity of the signals in the Fourier space. Despite the noise subtraction, in the spectrograms the drive signal is still present and distinguishable, most likely due to the plasma amplifying the signal, regardless of the resonance with the diocotron mode.
All the spectrograms shown here have a temporal resolution, that is to say the time interval over which the Fourier transform of the signal is performed, of t=1.5 ms.
In fig. 6.7 the signal for a 100 ms excitation of the $l = 3$ mode, with $V_d = 1$ V, $\nu_d = 54$ kHz and in fig. 6.8, the corresponding plasma density profile at t=100 ms. Fig. 6.8 clearly shows an $l = 3$ mode, although the signals in fig. 6.7 suggest that at 100 ms the amplitude of the $l = 2$ mode is bigger than that of the $l = 3$ mode: this is because of the different geometry of the electrostatic diagnostic. While the S2B sector ($180°$) collects all the odd modes but is not the optimal choice for the $l = 3$ mode, the S4T+S4B ($90°$+$90°$) is the configuration that most efficiently picks up the $l = 2$ mode signal, so the two signals

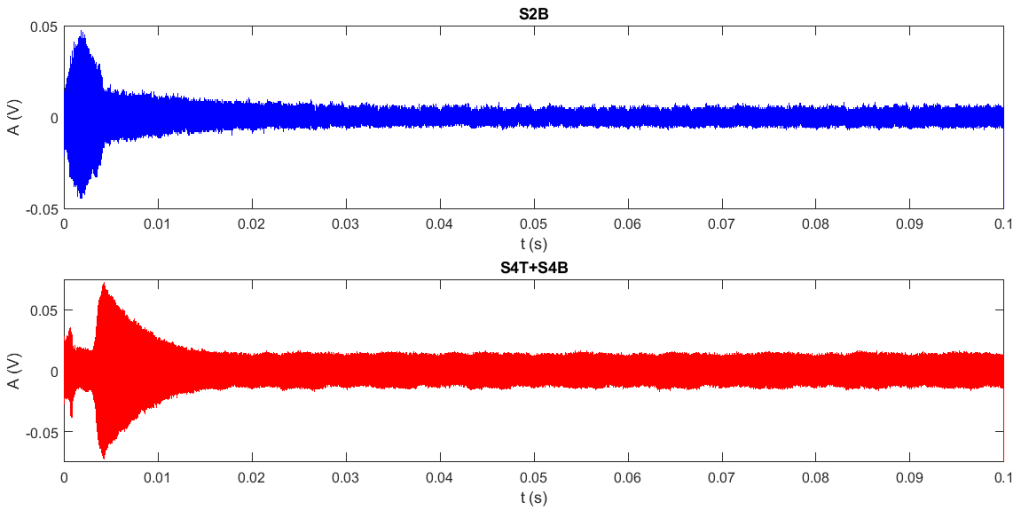

Figure 6.7: Electrostatic signal for a $t_d = 100$ ms, $V_d = 1$ V_{pp}, ν_d =54 kHz excitation, for both the diagnostic configurations. At $t \sim 3$ ms, the resonance peak of the $l = 3$ mode, on S2B, followed by its rapid decay and growth of the $l = 2$ mode (S4T+S4B).

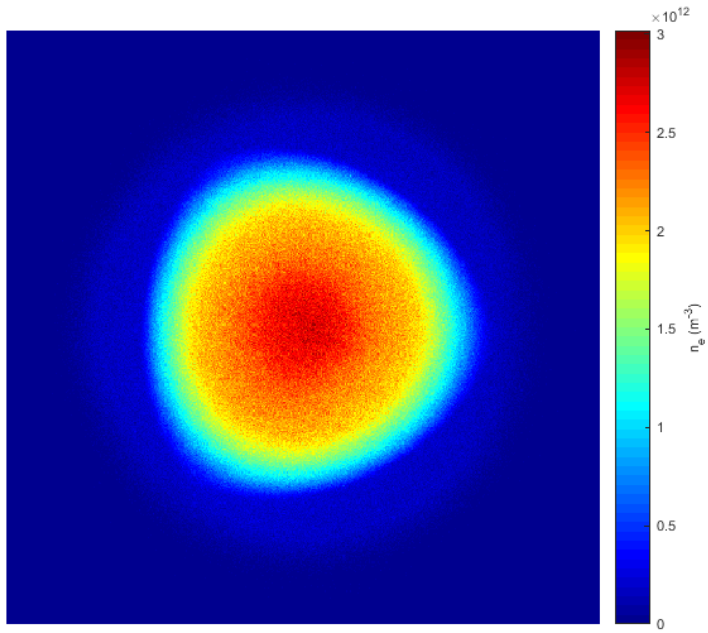

Figure 6.8: Plasma density profile obtained with $\nu_d = 54$ kHz, $V_d = 1.3$ V_{pp} and for $t_d = 100$ ms. The plasma is ejected immediately after the drive is turned off.

in fig. 6.7 cannot be directly compared because they are collected with two different gain factors due to the diagnostic geometry.
Two facts are evident: first, the highest excitation peak is at $t \sim 3$ ms, and its amplitude is almost a factor 5 bigger compared to the amplitude of the mode when we are ejecting the plasma, at $t = 100$ ms. Second, this first resonance peak rapidly decays into another mode, with even azimuthal symmetry, since it is only detected with the coupled S4 sectors. The spectrograms of the signals are shown in figs. 6.9 and 6.11, and in more detail in figs. 6.10 and 6.12. In fig. 6.9, obtained with the S2B sector, we can see at $\nu \sim 11$ kHz a residual $l = 1$ diocotron mode, excited because of minor asymmetries in the sectored electrodes, and also its second, third, and fourth harmonics can be identified at $2\nu_{l=1} \sim 22$ kHz, $3\nu_{l=1} \sim 33$ kHz and $4\nu_{l=1} \sim 44$ kHz respectively. At $\nu \sim 54$ kHz, for $t <$10 ms, the $l = 3$ diocotron mode has its first and stronger resonance. In fig. 6.11 we can see that the signal that arises immediately after the decay of the $l = 3$ mode has a frequency $\nu \sim 33$ kHz, matching the $l = 2$ diocotron mode frequency, while the constant amplitude line at $\nu = 54$ kHz is the drive excitation, still present after the noise removal because of the unavoidable signal bleeding. We can affirm that what we observe at $t \sim 3$ ms is the wave decay $l = 3 \rightarrow l = 2$. We expect this to happen with the other diocotron modes too, although we cannot detect the electrostatic signal.
The cascade decay of the l mode into the longer wavelength $l - 1$ mode, has already been studied in nonneutral plasmas, e.g. in [49] and [50]. Contrary to the studied cases in the cited literature, in our case the diocotron mode decay is not a free evolution phenomenon, because of the continuous external excitation, and the decay mechanism is not clear yet.
In figs. 6.13, 6.14, 6.15 the CCD images for the plasma profile expelled at the peak resonance. In this case, the perturbation regime is highly non-linear, hence the rapid mode damping: the plasma vertices have a significantly different n_e and therefore a different ω_l compared to the inner plasma radii, so the resonance with the drive is lost, because we no longer satisfy $\omega_l|_{R_p} = \omega_d$. Since the outer electrons rotate with a slower ω, the plasma is subject to filamentation, and its typical equilibrium parameters, R_p, n_e and $\phi(r)$ change. Plasma also loses particles: with an external multipolar excitation, some equipotential lines are not closed anymore, but end on the trap wall. The stronger the applied potential, the more these open equipotential lines penetrate into the trap, and more electrons are lost on the trap wall.
If the non-linearity regime conflicts with the small perturbation theory presented in Part I, for example the mode amplitude does not grow linearly as predicted in (2.22), the new plasma equilibrium configuration allows the recoupling with the drive, hence we still see the mode at 100 ms. The drive frequency matches the diocotron frequency at some inner plasma radius, for which $\omega_l|_{R^*} = \omega_d$, with $R^* < R_p$, giving rise to a resonance weaker than the one observed at $t \sim 100$ ms, since the drive is tuned for the original equilibrium configuration, the one in fig. 6.2, and the Debye shielding hampers the perturbation penetration to the inner resonance radius R^*. An interesting example of this uncontrolled recoupling process is in 6.16: the drive is out of resonance, $\nu_d = 58$ kHz, $V_d = 1.8$ V_{pp} and during the whole excitation time there are three different recoupling episodes, with their relative decay to the lower mode. The faster revival of the $l = 3$ mode after the decay of the $l = 2$ mode is related to the drive being slightly out of resonance. Comparing the $l = 3$ mode amplitude of fig. 6.16 with fig. 6.7, we notice that there is a significantly weaker diocotron mode, so the plasma profile is not as severely perturbed as in the resonant case. Therefore the mode is easily excited different times, though with smaller amplitude, because the plasma core is not degraded by a strong nonlinear mode resonance.

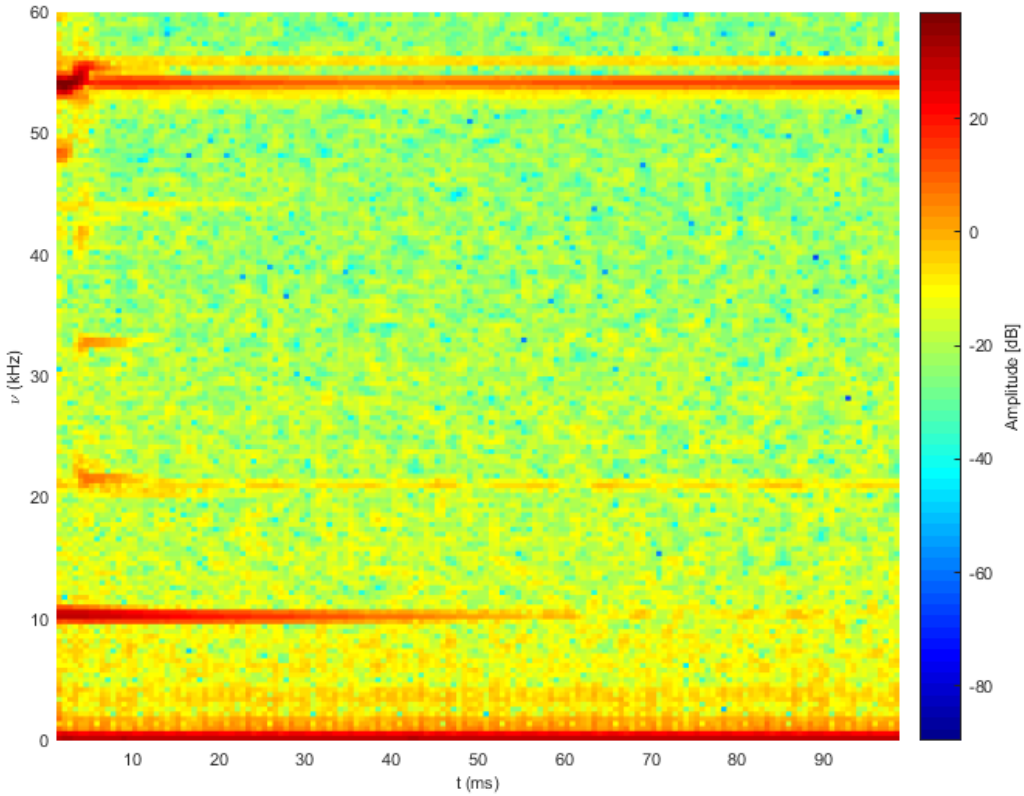

Figure 6.9: Spectrogram of the signal collected on S2B for $\nu_d = 54$ kHz and V_d =1 V_{pp}. At ~ 11 kHz a residual $l = 1$ diocotron mode, and its second, third, and fourth harmonics can be identified at ~ 22 kHz, ~ 33 kHz, ~ 44 kHz respectively. The $l = 3$ mode quickly rises and damps in the first 5 ms, and can be spotted at $\nu = 54$ kHz. Also, the nonlinear growth in frequency due to the amplitude decay is distinguishable. In fig.6.10, a detail of the $l = 3$ mode signal.

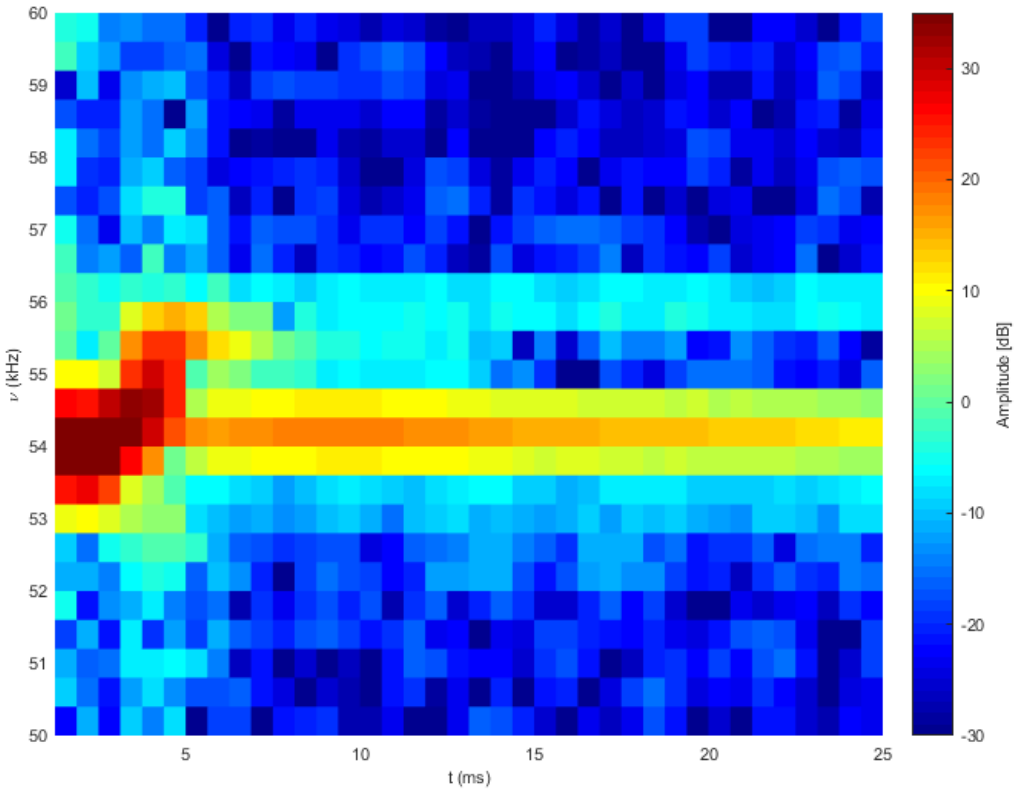

Figure 6.10: Detail of the spectrogram in fig. 6.9, zoomed on the $l = 3$ mode peak resonance. In 5 ms, the mode frequency changes by $\Delta\nu \sim 2$ kHz because of the nonlinear relationship between frequency and mode amplitude.

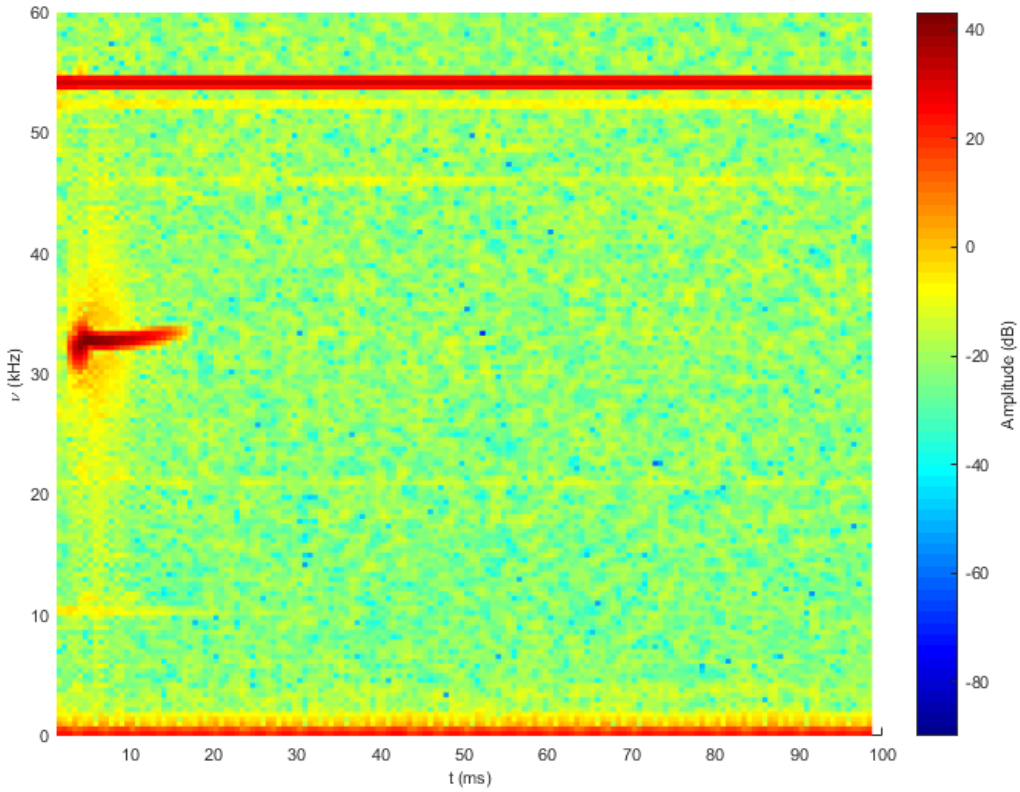

Figure 6.11: Spectrogram of the signal collected on S4T+S4B for $\nu_d = 54$ kHz and V_d =1 V_{pp}. The $l = 2$ mode is evident at $\nu = 32$ kHz, and rises as the $l = 3$ mode damps. At $\nu = 54$ kHz is the drive excitation.

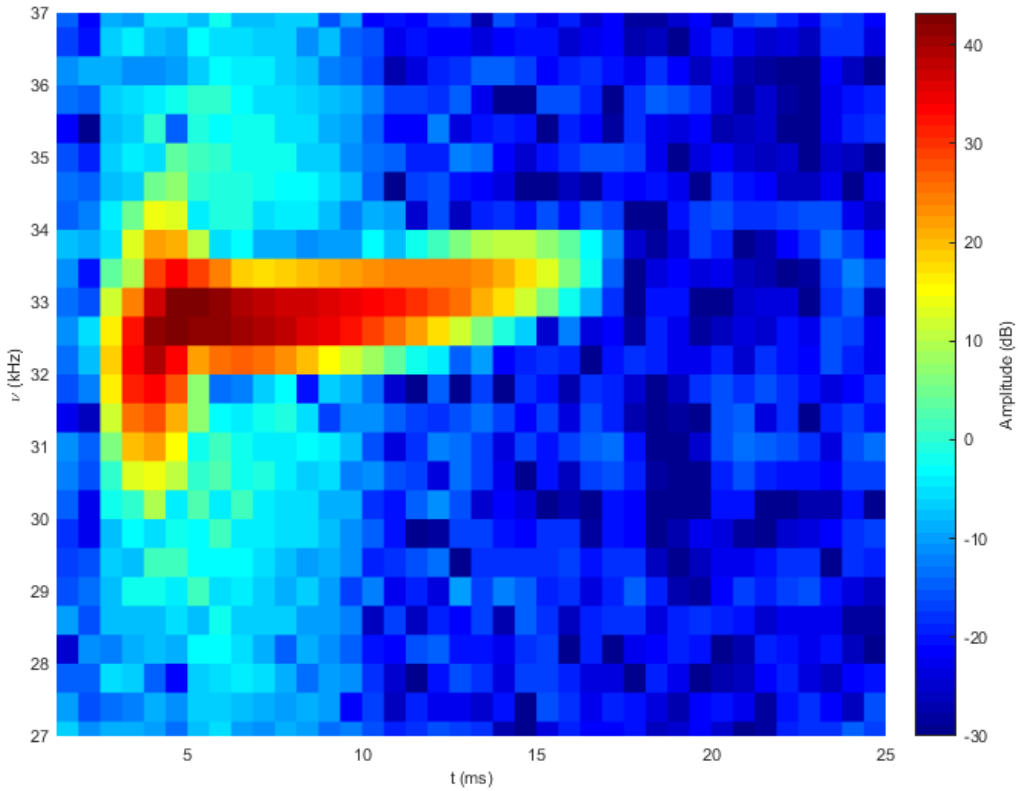

Figure 6.12: Detail of the spectrogram in fig.6.11, zoomed on the $l = 2$ mode. The mode grows when the $l = 3$ mode damps, see 6.10, and its frequency changes by $\Delta\nu \sim 2$ kHz.

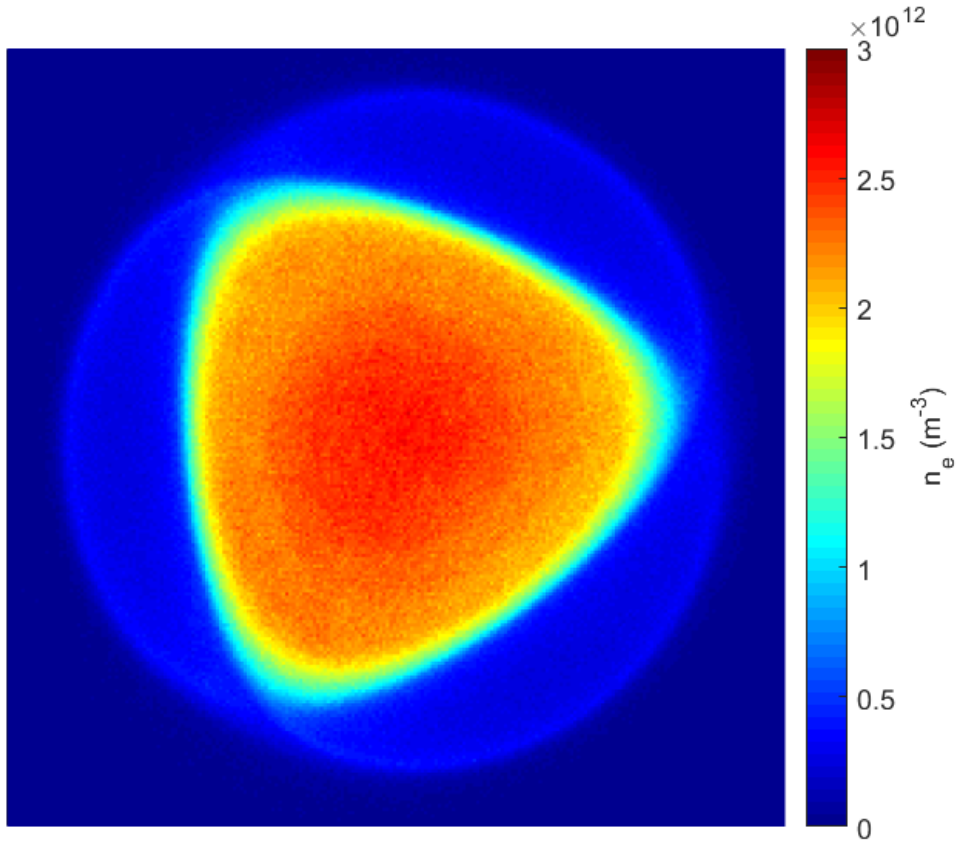

Figure 6.13: Plasma profile after a $t_d = 2$ ms, $V_d = 1$ V_{pp}, $\nu = 54$ kHz excitation: it corresponds to the amplitude peak observed with the electrostatic diagnostic. The amplitude of the diocotron mode is strong enough to irreversibly change the plasma equilibrium profile.

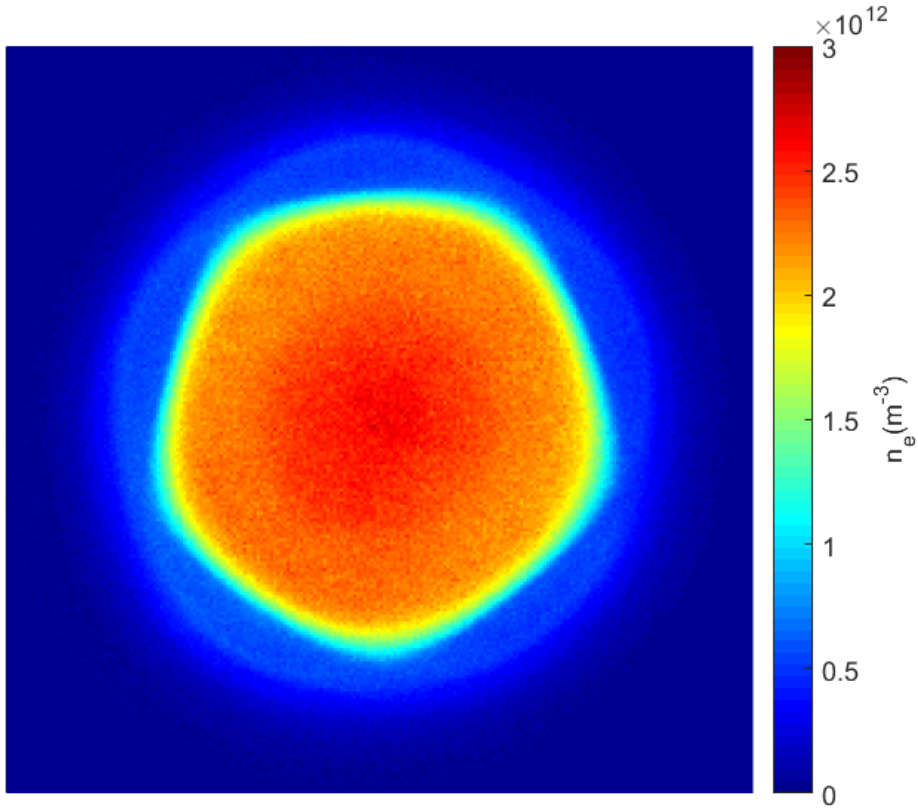

Figure 6.14: Plasma profile after a $t_d = 5$ ms, $V_d = 2\,\mathrm{V}_{pp}$, $\nu = 105$ kHz excitation, that corresponds to the $l = 5$ diocotron mode.

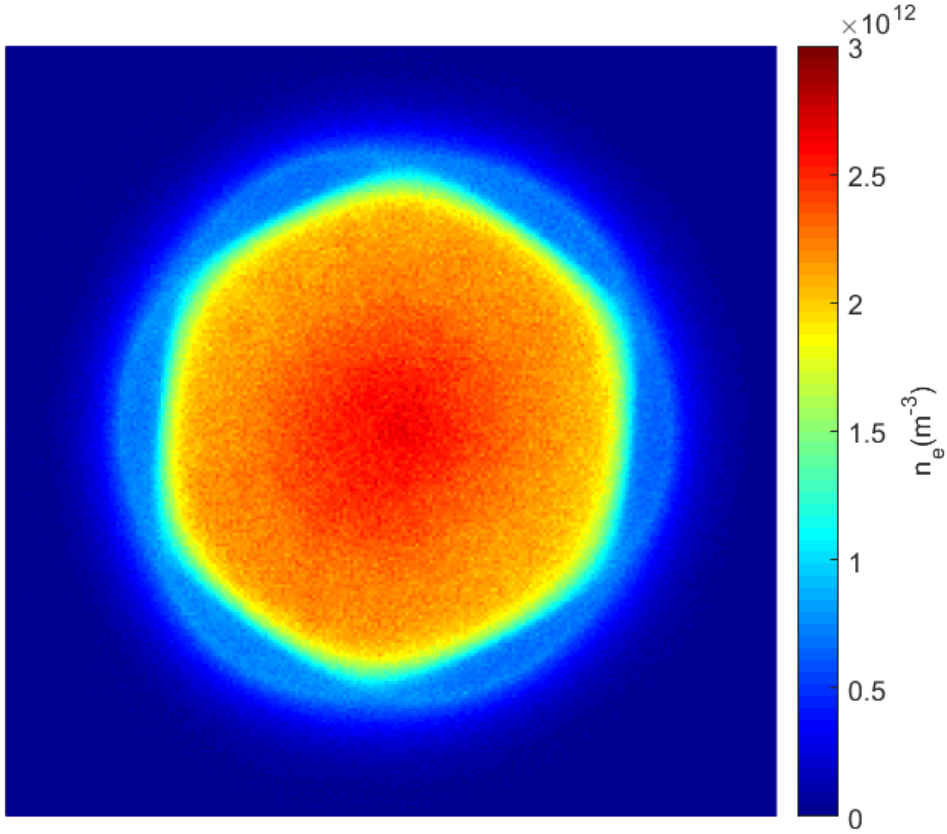

Figure 6.15: Plasma profile after a $t_d = 5$ ms, $V_d = 2\,\mathrm{V}_{pp}$, $\nu = 130$ kHz excitation, that corresponds to the $l = 6$ diocotron mode.

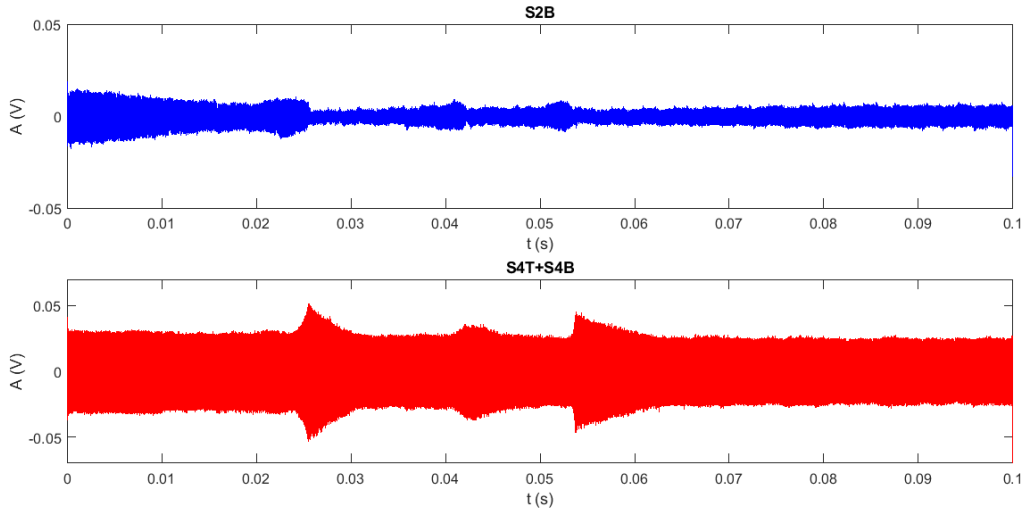

Figure 6.16: Electrostatic signal for a $t_d = 100$ ms, $V_d = 1.8$, V_{pp}, $\nu = 58$ kHz excitation. The drive is slightly out of resonance, and it allows a series of resonant couplings and decays.

6.3 Autoresonant excitation

The excitation at fixed frequency proves to be an efficient tool in exciting the diocotron modes, but it does not grant total control over the mode growth. As seen in fig. 6.7, the resonance happens after few ms, and in 1 ms the diocotron mode reaches the maximum amplitude. Moreover, due to the shot to shot variation, the resonance peak jitters in time of few ms. These features of the static frequency excitation prevent the possibility to completely control the excitation: we cannot, for example, selectively trigger some electronics for a certain value of the mode amplitude, because the resonance changes uncontrollably in time, and this shift is comparable with its typical growth time.
To overcome this unpleasant lack of control, we decide to excite the mode not with a static frequency drive, but with a frequency sweeping in time, to induce autoresonance (nonlinear phase locking) [51].
Autoresonance is the natural tendency of a weakly driven nonlinear system, under certain conditions, to stay in resonance with its drive even if the parameters of the system vary in time. For diocotron modes with $l \geq 2$, there is a nonlinear relationship between the mode frequency and its amplitude, as can be seen in fig. 6.10 and fig. 6.12 and studied in detail for the $l = 2$ mode in [52], where $\dfrac{\partial \nu_l}{\partial A_l} < 0 \; \forall l$. In autoresonance, increasing (decreasing, in our specific case) the drive frequency will cause a corresponding increase in the oscillation amplitude. In some cases, the system need not start phase locked to become phase locked; if the drive frequency is swept slowly through the linear resonant frequency, the system will phase lock automatically. So if we start with a frequency higher than the resonance frequency, and we decrease it slowly and regularly, we expect the system to lock in and the amplitude of the diocotron mode to increase, because of the sign of the derivative in $A(\nu)$. Assuming that the peak resonance is obtained for $\nu \sim 54$ kHz, as can be inferred from fig. 6.6, we impose a frequency sweep 66 kHz$\rightarrow$52 kHz in 100 ms. We perform the drive frequency sweep for various drive amplitudes,

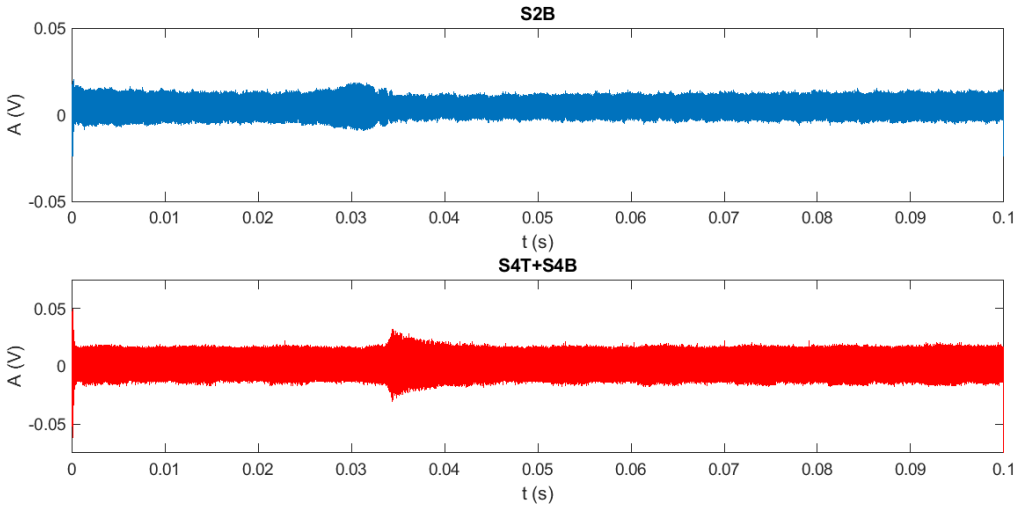

Figure 6.17: Electrostatic signal, for both diagnostic configurations, for $V_d = 1.1$ V and frequency $\nu_d : 66 \rightarrow 52$ kHz in 100 ms. We can clearly see the $l = 3$ mode frequency rising in a time almost 10 times bigger compared to sudden growth of fig. 6.7. We are already over the amplitude autoresonant threshold, so the diocotron mode amplitude does not depend on the drive amplitude, and this signal can be compared to those in figs. 6.7 and 6.16.

0.1 V$< V_d(pp) <$ 2.3 V, to look for an amplitude threshold $V_{d,th}$ and other peculiar features of autoresonance. Below this threshold, the mode amplitude is small and increases with the drive amplitude; above the threshold the mode amplitude is independent of the drive amplitude.
In figs. 6.17, 6.18 and 6.19 the signal with the drive frequency sweep for $V_d = 1.1$ V is shown. In fig. 6.18 we can see that the $l = 3$ mode amplitude grows from $t \sim 10$ ms to $t \sim 35$ ms, when an abrupt decay interrupts this first growth. After the sudden decay, the mode starts rising again. In fig. 6.19 we can see the growth of the $l = 2$ mode immediately after the decay of the $l = 3$ mode, at $t \sim 35$ ms, but its evolution is not related to the sweeping drive. In both the spectrograms, the sweeping external drive is clearly distinguishable even after the noise removal because of the signal bleeding. In fig. 6.20 the amplitude evolution in time for the $l = 3$ and $l = 2$ diocotron modes: the $l = 3$ mode grows at a slower rate compared to the first resonance peak of the static ν_d excitation; it takes almost ~ 30 ms to reach the maximum amplitude. Even though we lack experimental data with a temporal resolution high enough to assess the phase locking of the plasma mode with the external drive, this is a strong hint of autoresonance.

In fig. 6.21 a comparison between two profiles ejected at the same time, t=45 ms, one with drive amplitude over threshold, and the other with drive amplitude below the threshold. For this chirp rate $\frac{\Delta\nu_d}{\Delta t_d} = -1.4 * 10^5$ Hz/s, we find that the drive amplitude threshold is $V_{d,th} \sim 0.2$ V, as can be deduced from fig. 6.22 where we can see the maximum amplitude of the $l = 3$ mode for several drive amplitudes. In fig. 6.22 we can also notice that, although we are above the autoresonant threshold, and therefore the diocotron mode amplitude does not depend on the sweeping drive amplitude, as the drive amplitude increases over $A_d > 0.8$ V the mode maximum amplitude decreases. Again, this effect is due to the change in the plasma profile and particle loss caused by

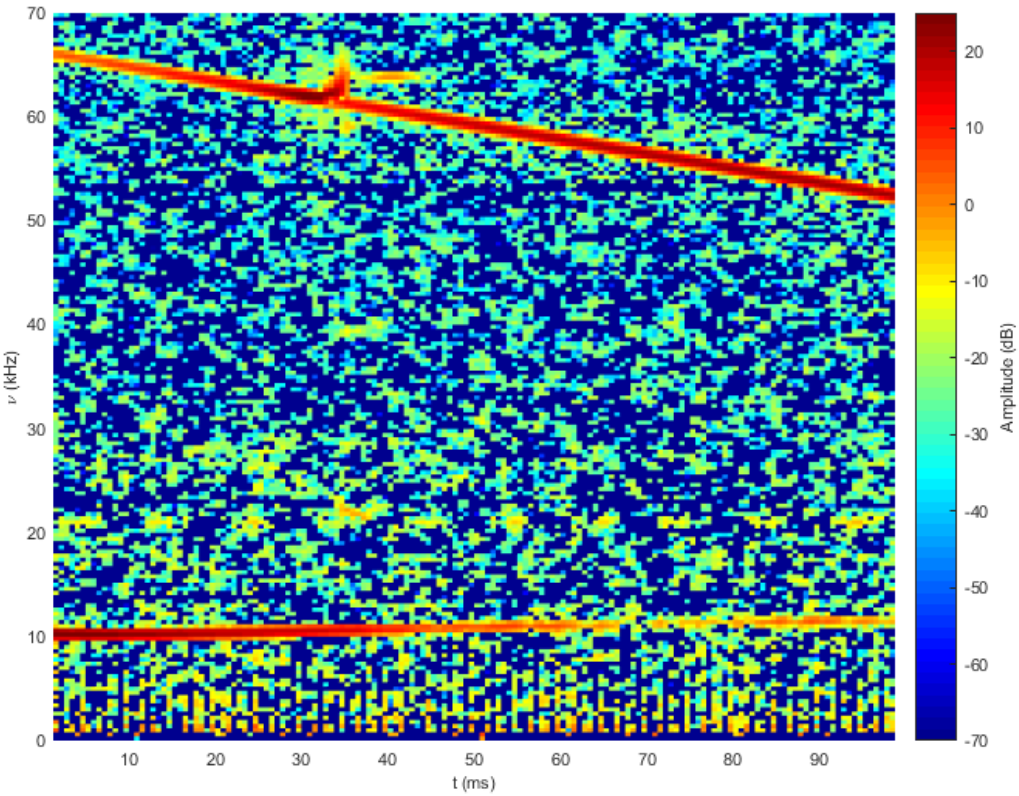

Figure 6.18: Spectrogram of the signal collected on S2B with a sweeping drive. In this case V_d=1.1 V_{pp}. At $\nu \sim 10$ kHz the first order diocotron mode.

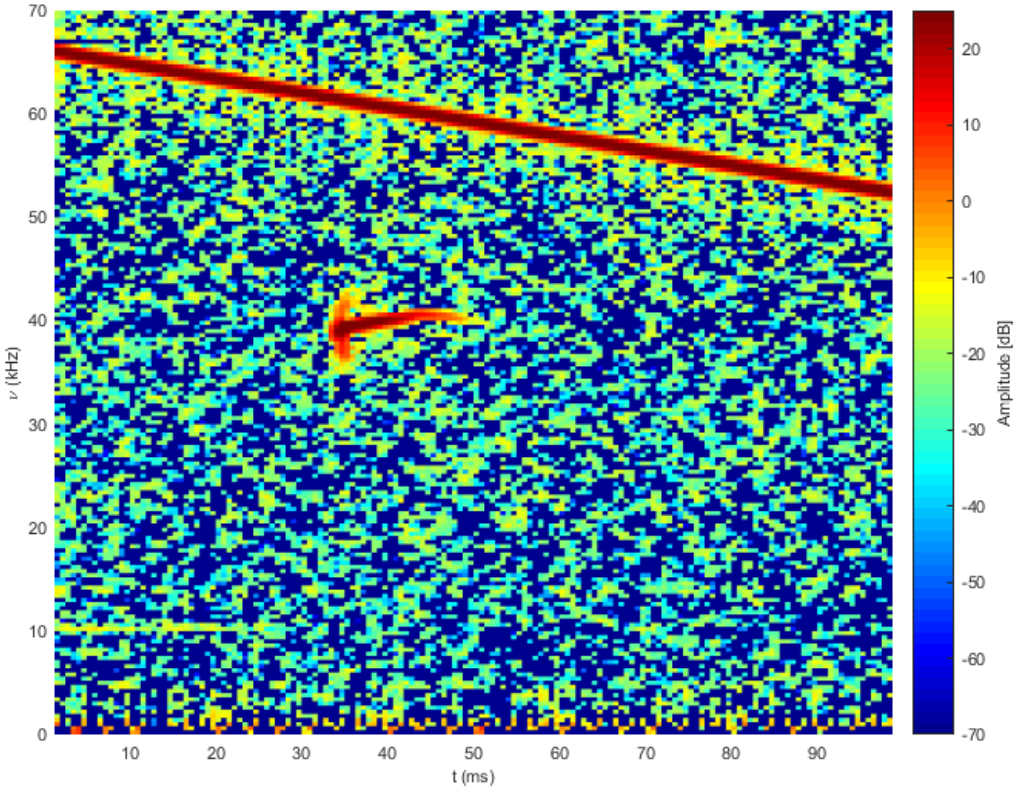

Figure 6.19: Spectrogram of the signal collected on S4T+S4B with a sweeping drive. In this case V_d=1.1 V_{pp}. The $l = 2$ mode follows from the decay of the autoresonant $l = 3$ mode, and appears at $t \sim 35$ ms, with $\nu \sim 40$ kHz.

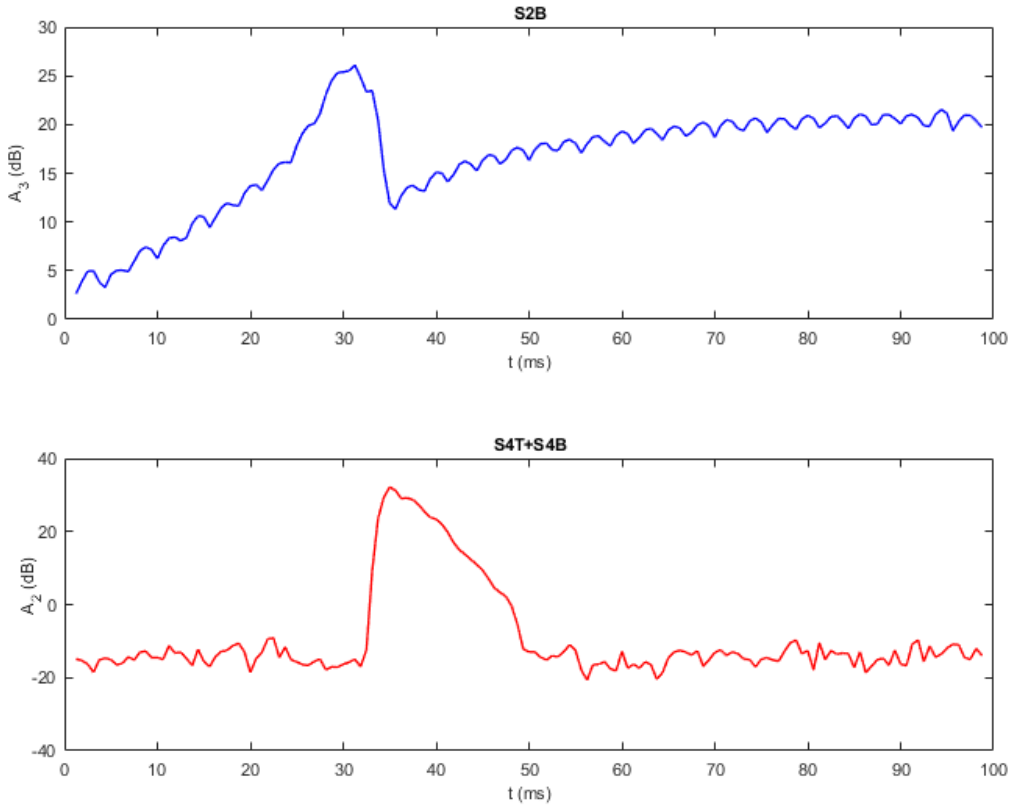

Figure 6.20: Amplitude of the $l = 3$ mode (top panel) and $l = 2$ mode (bottom panel) for the case of a sweeping drive with V_d=1.1 V_{pp}, corresponding to the signal in figs. 6.17, 6.18, 6.19. We can see in better detail the slow growth of the l=3 mode, likely due to phase locking with the external drive. As for the fixed frequency drive, when the $l = 3$ mode reaches saturation, it decays abruptly, and the l=2 mode grows.

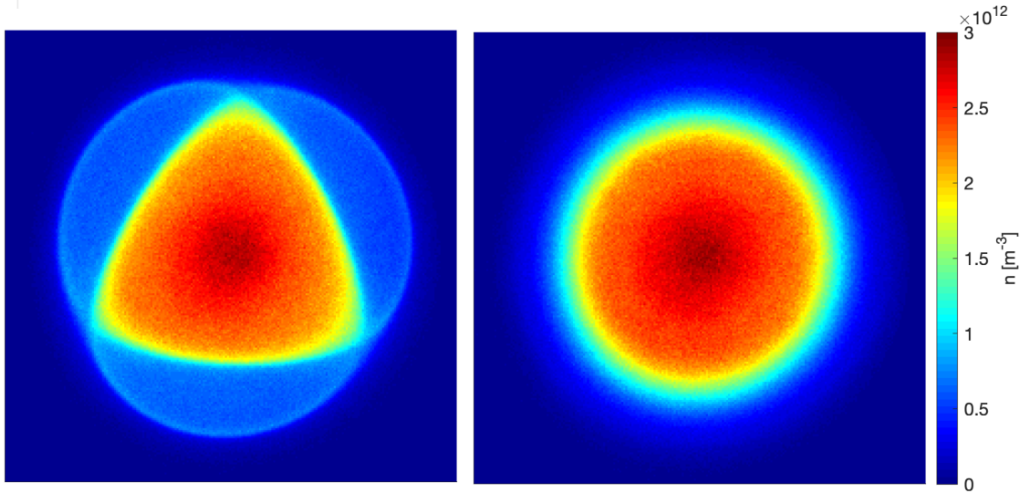

Figure 6.21: To the left, plasma profile for a sweeping amplitude drive over threshold,V_d=0.6 V_{pp}, while to the right for an under threshold drive, V_d=0.1 V_{pp}. Both are taken at t=45 ms.

a strong, non-perturbative external excitation. Moreover, experiments prove that an external drive with an increasing frequency sweep, 52 kHz→66 kHz in 100 ms, does not induce any significant diocotron mode excitation.
When the diocotron modes are excited with a drive sweeping in frequency, and become subject to autoresonance, their growth in time is slower compared to the static frequency drive excitation: autoresonance is the key ingredient for a better control of the modes.

6.4 CCD image data analysis

Given the limitations of the transimpedance amplifier, we cannot measure the induced electrostatic signal for the $l > 3$ modes. But we can evaluate the amplitude of the modes thanks to the optical diagnostic.
To improve the accuracy of our measurements, all the images are subject to noise removal and calibration, see appendix B. Firstly, with a bilinear interpolation algorithm, we transform our cartesian CCD pixel grid into a polar grid, so that we switch from $n_e(x, y)$ to $n_e(r, \theta)$, with $(r = 0)$ the charge center (x_c, y_c), defined in cartesian coordinates, as

$$x_c \equiv \frac{\sum_i x_i Q_i}{\sum_i Q_i} \qquad y_c \equiv \frac{\sum_j y_j Q_j}{\sum_j Q_j} \tag{6.1}$$

Now, for all the discrete r^*, we re-write $n_e(r, \theta)$ in an harmonic Fourier series:

$$n(\theta)|_{r^*} = \sum_{l=0}^{+\infty} A_l(r^*) \sin(l\theta) + B_l(r^*) \cos(l\theta) \tag{6.2}$$

where A_l and B_l are the Fourier amplitude of the l^{th} term. Now that we have the amplitudes, in terms of the Fourier series, of every diocotron mode for every discreet $r*$ of the

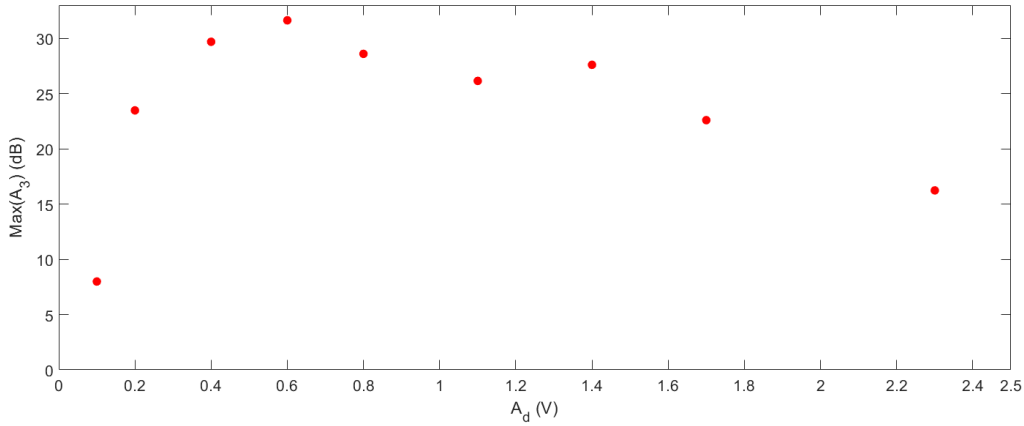

Figure 6.22: Maximum amplitude of the $l = 3$ diocotron mode for several drive amplitude. The mode amplitude is calculated as the average of three shots

polar grid, we define the mode amplitude as

$$\mathcal{A}_l \equiv \int_0^{R_w} \int_0^{2\pi} \sqrt{(A_l^2(r) + B_l^2(r))} r dr d\theta \quad \rightarrow \quad 2\pi \sum_{r*} \sqrt{(A_l^2(r^*) + B_l^2(r^*))} r^* \Delta r \quad (6.3)$$

where Δr is the radial step length. That is to say, the total mode amplitude is obtained by summing the mode contribution at all the radii with the proper radial weight: at bigger radii, the deformation is stronger.
With the image analysis we can evaluate the amplitude of all the diocotron modes for every CCD image, overcoming the limitation of the electrostatic diagnostic, but losing the time resolution.
In fig 6.23, a comparison between the amplitude of the $l = 3$, $l = 4$, $l = 5$ modes, calculated via optical diagnostic, for different drive frequencies. The modes amplitudes are normalized to the respective A_0, that is the plasma "unperturbed" (circular) density. With this frequency scan, we can see that $\mathcal{A}_l(\nu_d)$ has a resonant behavior, with the resonant peak at the l diocotron mode, at least qualitatively in the $\omega_{E\times B}$ range given by the plasma profile in fig. 6.3. The curves in 6.23 are not symmetric with respect to the peak frequency, and do not exhibit a $\delta(\nu_d - \nu_l)$ resonance, but rather a Lorentzian shape, because of the $\nu_l(A)$ dependence induced by the non-linear regime of the experiments. The drive amplitude is regulated so to have the most evident effect, that is to say a plasma profile with the proper geometrical deformation, with the minimum excitation. Therefore, we cannot claim from fig. 6.23 if the mode amplitude follows a $\left(\frac{R_p}{R_w}\right)^l$ dependence, as suggested by eq. 2.22, because the drive amplitude is not the same, and the excitation necessary for the higher modes, $l \geq 5$ is usually too strong for the $l = 3$ mode, disrupting the plasma profile. In fig. 6.23 the plasma is ejected after few ms, that is to say in correspondence of the first resonance peak, to avoid the complex recombination dynamics of longer excitement times. Even though these measurements are less practical, because of the limited control we have in ejecting the plasma at the desired mode amplitude, we are certain that this first peak comes from a mode excited on a density profile like 6.2, and not from a density profile subject to filamentations and smearing as we can infer from the electrostatic signals. In fig. 6.24, the resonance curves for the $l = 3$ mode at a 100

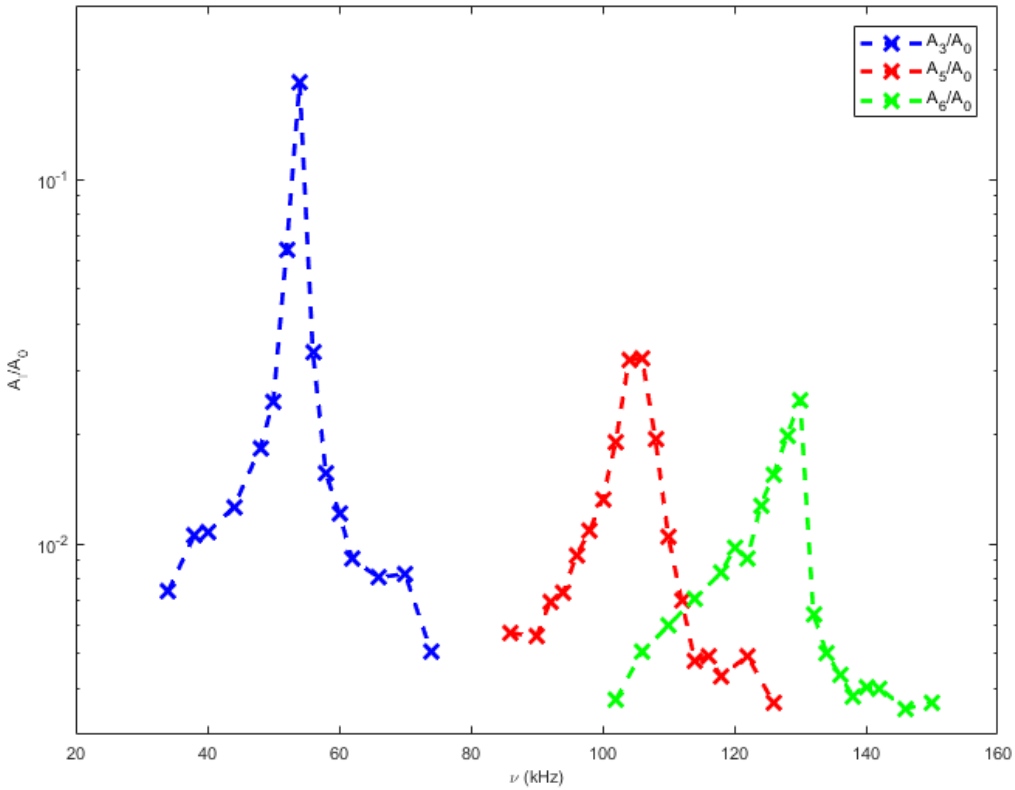

Figure 6.23: Resonance for the various modes. Each curve is obtained with its proper rotating drive configuration, in separate experiments. For the $l = 3$ mode $V_d = 1$ V_{pp} and the plasma is ejected at $t = 2$ ms. For the $l = 5$ and $l = 6$ mode $V_d = 2$ V_{pp} and with the plasma ejected at $t = 5$ ms

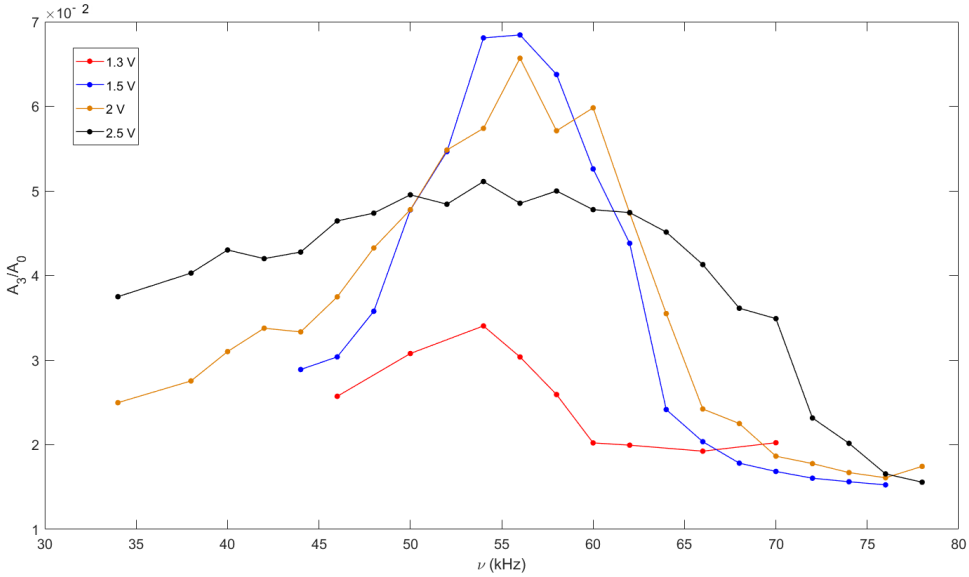

Figure 6.24: Resonance curves for the $l = 3$ mode for various amplitudes at t=100 ms. As the drive potential grows, the resonance curves become broader. The normalized amplitude at the peak is roughly one half the peak amplitude in fig. 6.25: this is because these are long-time (100 ms) excitations, so we are not measuring the first, high amplitude resonant peak.

ms. The resonance curves are sharper for lower drive amplitude values. This is because, if we increase the external perturbation amplitude, we enter the non-linear regime, and we change the plasma equilibrium density profile, making the resonance less defined: there is no longer a unique plasma radius at which the plasma density is such that it matches the drive frequency. The broadening of the resonance curves as the amplitude drive grows is continuous, and this denotes the absence of a threshold amplitude for the mode excitation, in opposition to the frequency sweeping drive.

In fig.6.25 we can see the amplitude of several diocotron modes obtained with the CCD image analysis for the excitation of an $l = 3$ mode. As expected the other modes do not resonate with the drive excitation and they contribute with an unavoidable, but very small, distortion. Their amplitude is at least one order of magnitude lower than the amplitude of the $l = 3$ mode, and their presence is due to small imperfections in the sectored electrodes, not perfectly symmetric.

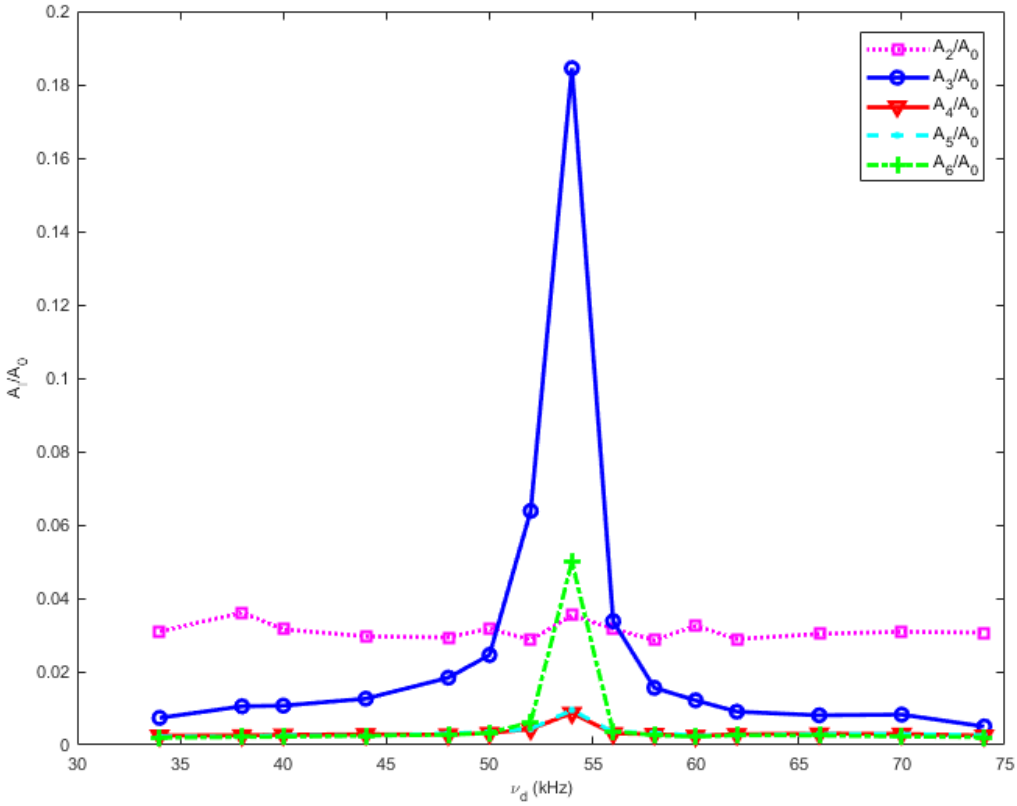

Figure 6.25: Frequency scan for an $l = 3$ diocotron mode excitation with $V_d = 1$ V_{pp} for a plasma ejected at t=2 ms. We show here all the modes amplitudes obtained with the analysis of the CCD image. The non resonant modes have an amplitude orders of magnitude lower compared to the $l = 3$ mode.

CHAPTER 7

TG modes behavior in non axisymmetrical plasma column

During an experimental session on CamV aimed at studying the behavior of TG waves under particular external excitations, it occurred that, when the plasma profile was not axisymmetric, the spectrogram of the electrostatic signal collected with any one of the electrodes showed a peculiar feature: the frequency of the TG modes presented a splitting. That is to say, we no longer observed one $\nu_{TG}(t)$ signal but two distinct $\nu_{TG}^{\pm}(t)$ signals, with frequencies close to the single TG frequency signal. Moreover, the higher the plasma deformation, the bigger the amplitude of the splitting $\Delta\nu = \nu^{+} - \nu^{-}$. To create a non-axisymmetric plasma profile, we excited a strong amplitude $l = 2$ dioctron mode, that makes the plasma elliptical, see 1.1.
It is the first time this phenomenon is observed, and there is no any theoretical explanation for it. We have performed several experimental campaigns, with CamV, in order to investigate these new features of the nonlinear interaction between orthogonal waves in magnetized, pure electrons plasma columns, to exploit the various dependencies and elaborate a first theoretical model.

7.1 Experimental setup

The experimental campaign consists in analyzing the behavior and evolution of TG and $l = 2$ diocotron modes when they are simultaneously excited on the same plasma column, for different TG modes. The experiments follow the usual inject-hold-eject cycle: the plasma is generated through a biased thermocathode, injected into the trap by raising to 0 V the potential on the end electrode close to the filament (usually L2) and trapped by lowering the potential of that end electrode back to -100 V. The plasma is then manipulated, that is to say, in this case, diocotron and TG modes are excited at the same time and all the interesting quantities are measured, and, in the end, ejected by raising to 0 V the potential on the end electrode close to the phosphor screen (usually G10). The potential on this electrode is then brought back to -100 V and another experimental cycle can be performed.
We are interested in exciting and observing the evolution of a TG wave when the plasma column has an elliptical profile, in this case due to the presence of an l=2 diocotron mode. We require our plasma to have a flat profile, to allow for an easier theoretical model of the splitting phenomenon, and to be able to use the results already existing in literature about diocotron and TG waves. Moreover, we are interested in having a plasma profile that is as repeatable as possible, to avoid further difficulties in the analysis because of the nonlinear dependencies of the plasma relevant quantities. For example, different density profiles have different diocotron wave frequencies, and so different critical radii and damping times, and therefore different temperature evolutions in time; that means

different TG waves frequencies.
For all the experiments, we have kept this confinement setup:

- Confinement between L2 - G10: confinement length of 48 cm
- $V_{confinement}$= -100 V on both L2 and G10
- B= 13 kG
- Transverse magnetic field correction: V_x= -90 mV, V_y= -20 mV
- V_{bias}= 30 V
- Squeeze 100 ms after injection, for 7900 ms, applying -30 V on G5

Squeezing the plasma induces radial transport that removes the central spike, smooths the density profile and removes any residual l=1 diocotron mode from the injection process [53]. In fig. 7.1 an example of plasma density profile is shown. Before exciting the l=2 diocotron mode and the various TG modes, we let the plasma cool for 10$\sim$20 s, to let the plasma reach the thermal equilibrium, after the heating induced by the squeezing. Once in this equilibrium state, we excite the waves on the plasma column.
For the l=2 diocotron mode, we follow this excitation scheme:

- Excitation on S4BD
- ν= 16-18 kHz
- V_{pp}= 6-8 V
- Wave cycles: 10-20
- Detection on S4AC, coupled with 1 MΩ resistor

A range of parameters for the excitation has been given because of the unavoidable differences between the plasma profiles of different experiments. Indeed, even just in few hours, plasma parameters can change, due, for example, to the trap walls heating and therefore higher equilibrium plasma temperature.
Even though we dispose of a direct diagnostic for the diocotron modes amplitude, that is to say measuring the induced potential on one or more of the azimuthally sectored electrodes, we are more interested in the geometrical deformation of the plasma profile, rather than in the amplitude of the l=2 mode.
Given an ellipse with major radius a and minor radius b, we define the ellipticity ϵ as

$$\epsilon \equiv \frac{a^2}{b^2} - 1 \tag{7.1}$$

The ellipticity ϵ is measured via optical diagnostic (CCD camera coupled with the phosphor screen): it is the quantity *q2eps* in fig. 7.1.
We can look for a relationship between the ellipticity and the amplitude of the l=2 mode through a calibration procedure. With the above mentioned confinement scheme, we excite, 20 s after the injection, an l=2 mode with different amplitude and we measure the induced signal on S4AC until the ejection. 30 s after the injection, that is to say, 10 s after the excitation of the diocotron mode, we eject the plasma on the phosphor screen, collecting the image with the CCD, and therefore measure the plasma ellipticity too. The ejection process takes $\sim \mu$s, orders of magnitude less than the typical evolution times of

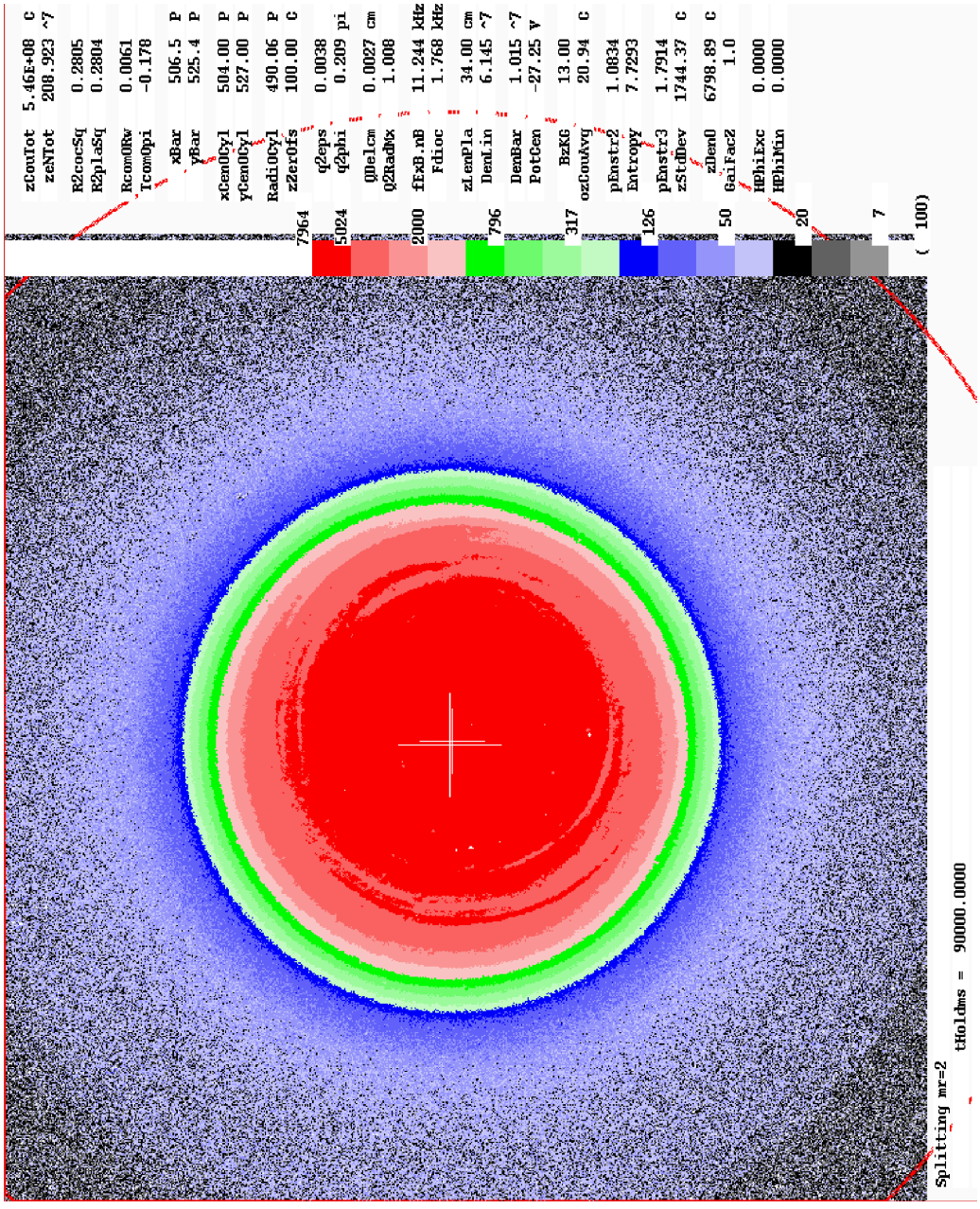

Figure 7.1: CCD image of typical plasma density profile used for the TG splitting experiments. In this case, the plasma is held for 90 s. Among the measured and calculated quantities, "$q_2 eps$" is the ellipticity.

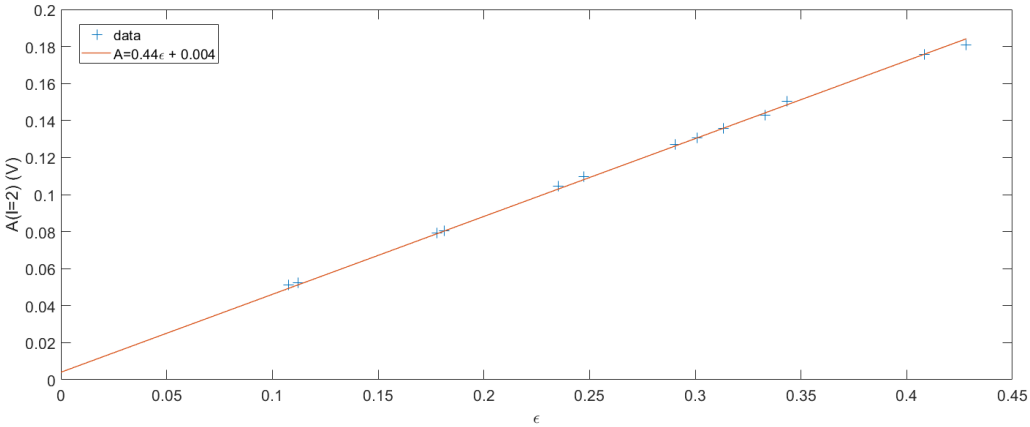

Figure 7.2: Measured amplitude of the l=2 diocotron mode (electrostatic diagnostic) and relative plasma ellipticity (optical diagnostic) obtained with different amplitudes of the excitation signal.

diocotron modes $(\omega_{E\times B})^{-1} \sim$ ms, so the plasma impacts the phosphor screen with the l=2 mode amplitude that is the last measured with the electrodes. In this way we can unambiguously associate plasma ellipticity and amplitude of the diocotron mode. As can be seen in fig. 7.2 the ratio ϵ/A is pretty much constant over a wide range of ellipticity, so with a linear fit of the calibration data, we establish that

$$\epsilon = 0.44 \left(\frac{1}{V}\right) * A(l=2) \tag{7.2}$$

We consider as background noise level those ellipticity values characterized by $\epsilon \leq 0.015$. With these plasma generation and confinement procedures, we usually produce plasmas with $T_{\|} \sim 0.1$ eV, hence TG waves have a typical decay time $\tau_{TG} \sim$ ms, caused by resistive wall image current dissipation (Landau damping is negligible at these temperatures), whereas an l=2 diocotron mode excited with an 8 V_{pp} signal has a typical decay time $\tau_{l=2} \sim 10^5$ ms. So, to study the behavior of TG waves propagating on an elliptical plasma with a wide range of ellipticity, and therefore for the longest time possible, we need to have more than one single TG wave propagating during our measurement time. To overcome this difficulty, we excite a sequence of 50 identical TG waves, one every 1 or 2 s, depending on the particular experiment. With this solution, we have a TG wave propagating on the plasma profile for the whole time it has an elliptical profile, that is to say, until the diocotron wave is damped. We do not have a continuous measurement, because from the damping of a TG wave to the excitation of the next one, we have more than 1 s of lost measurement time, but given the slow evolution of the diocotron mode, we still have a meaningful and precise characterization of the phenomenon over the whole range of ellipticity. 50 is the maximum number of times we can excite the TG waves during a single excite-hold-eject cycle because of technical limitations of the trigger and digitizer devices at our disposal on the CamV apparatus.

7.2 Experimental results: phenomenology of TG waves on an elliptical plasma

From an experimental point of view, we can excite and detect only few of the infinite number of different TG modes on a magnetized plasma column. We cannot detect waves with frequency $\nu_{TG} > 5$ GHz because that is the upper limit of our digitizer. Moreover, the higher the wave numbers (k_z, m_θ, m_r), the more complex the profile becomes, making it harder to design of a proper diagnostic scheme for the induced electrostatic signal. And the higher the wave numbers, the shorter is their damping time. Because of these issues, we can only work with a limited number of TG modes.
When a TG wave propagates in a non axisymmetrical plasma (elliptical in our case) what we observe is that, in Fourier space, a frequency splitting pattern appears, that depends on the magnitude of the plasma profile deformation.
In figs.7.3, 7.5, 7.6, 7.7, 7.8, we can see the spectrograms of the induced charge signal measured with one of the trap electrodes. On the x-axis is time, in ms, but it is not the real experiment time: it is the measured time, that is to say, the time during which we are actively measuring the signal. This total measured time is 108 ms and it does not take into account the time (usually $\sim$ s) between two consecutive TG excitations. From here we see the typical stepped profile of these spectrograms. On the y-axis is the measured frequency ν, in kHz. In color scale, the amplitude of the mode (A.U.), in logarithmic scale. For all the experiments discussed from now on, the plasma generation scheme and the l=2 mode excitation parameters given in table 7.1 are applied.
To label the TG modes and identify the wave numbers (k_z, m_θ, m_r), we take advantage of the dispersion relationship (3.25), with $T_e \sim 0.1$ eV. We look for longitudinal nodes by measuring the signal with different sectors: in this way we are moving along k_z. Once identified k_z (we always work with $k_z = 1$ modes) we calculate $k_\perp$ and, from (3.24), we extrapolate m_r. To identify m_θ we measure the TG wave signal with different combination of the azimuthal sectors of the "S" electrodes and, based on the different intensities with respect to the different angular sectors, we deduce the azimuthal structure of the wave.
In fig. 7.3 we can see the spectrogram of a $(k_z = 1, m_\theta = 0, m_r = 2)$ TG mode propagating on an elliptical plasma, and it is evident how, when we excite the l=2 diocotron mode, from a single frequency signal we have a three-frequency signal: two outer branches and a middle one, that is the continuation of the pre-existing single frequency signal.
In this case, the TG wave is excited on the H3 electrode, with frequency $\nu = 930$ kHz, amplitude $V_{pp} = 300$ mV, for 10 wave cycles, and we measure the induced electrostatic signal on the electrodes G8 and S7AB, both coupled with 1 MΩ impedance.
In the table 7.1, the temporal sequence of the experiment that generated fig. 7.3.
When the diocotron mode is damped, and the plasma returns to be circular, see fig. 7.1, the splitting structure disappears, and we have again a single frequency signal, slightly shifted from the original TG mode frequency because of the higher plasma temperature, caused by the several waves excitation.
We also observe that the diocotron mode do not experience any effect from the excitation of the TG modes: a diocotron mode propagating without any TG excitation on the same plasma generates a signal that is identical to that in fig. 7.4, that occurs when a TG mode and the $l = 2$ diocotron mode propagate simultaneously.
From fig. 7.3 we can say that there is a connection between the presence of the diocotron mode and the splitting of the TG signal, but we cannot exclude, for example, that the amplitude of the splitting $\Delta\nu = \nu^+ - \nu^-$ depends only on plasma temperature, or for example, that it depends on some kind of threshold parameter and that $\Delta\nu$ just becomes

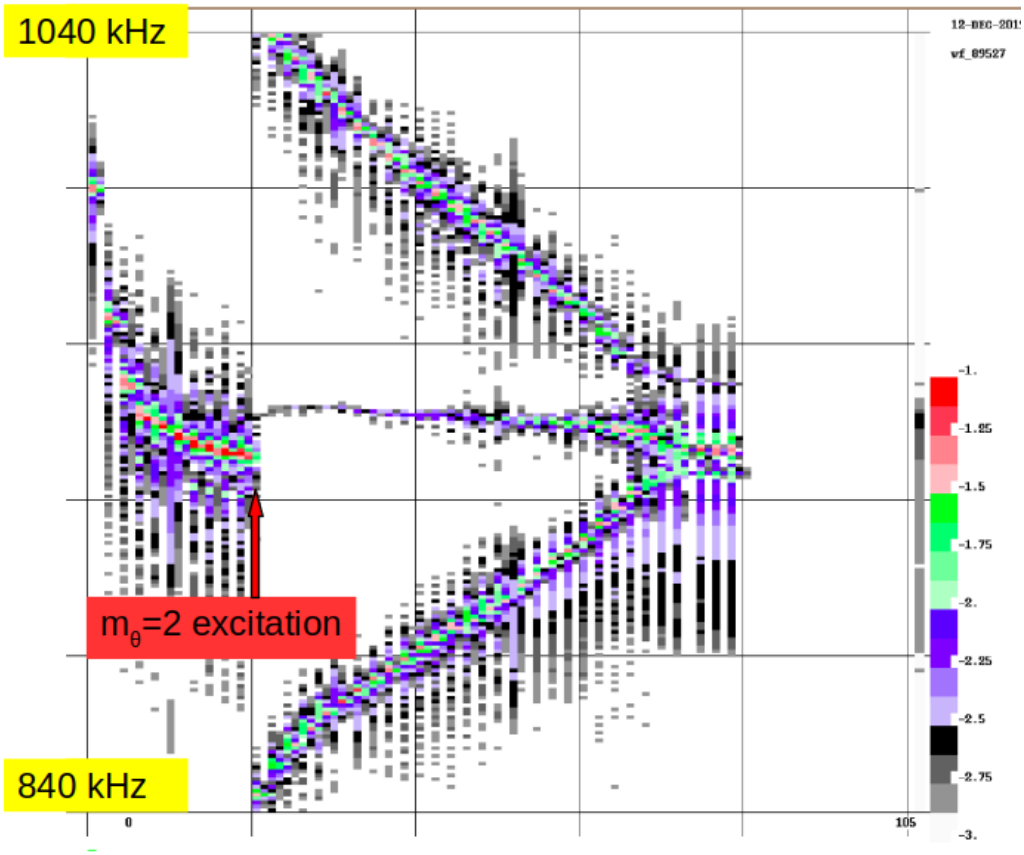

Figure 7.3: Spectrogram of the measured TG mode ($k_z = 1, m_\theta = 0, m_r = 2$) signal. Before the diocotron mode excitation, the frequency decreases because of plasma cooling. When the plasma becomes elliptical, due to the l=2 excitation, a three branches splitting appears. These three branches converge again in a single frequency signal when the ellipticity fades, approximately 40 s after the excitation.

smaller with time. In order to prove the direct dependency of $\Delta\nu$ on the ellipticity, we need to actively control the amplitude of l=2 and see how the TG frequency behaves.

In fig. 7.5 the spectrogram for an actively controlled diocotron mode experiment. It is obtained applying the feedback damping technique, but with the opposite goal of that described in chapter 6: we want to increase the amplitude of the diocotron mode, not to damp it. More specifically, we collect the diocotron mode signal on S7AE and we apply this same signal, shifted by $180°$, on the electrode S7CG, for 3 s. This technique allows us to actively increase the amplitude of the l=2 diocotron mode, without the risk of damping due to dephased wave interference (the plasma wave and the external excitation).
In the table 7.2, the temporal sequence for this kind of experiment is listed.
From fig. 7.5 we can see that the bigger is the ellipticity, the larger is $\Delta\nu$. When the ellipticity increases, because we are increasing the amplitude of the diocotron mode, $\Delta\nu$ increases too. When the ellipticity decreases, because the diocotron mode is damped,

t (s)	
0	injection
0.1	start squeeze
8	end squeeze
22	start TG modes excitation. Then, one every 1 s for 50 times
30	l=2 diocotron mode excitation
90	ejection

Table 7.1: Experimental sequence for the simultaneous excitation of diocotron modes and TG modes.

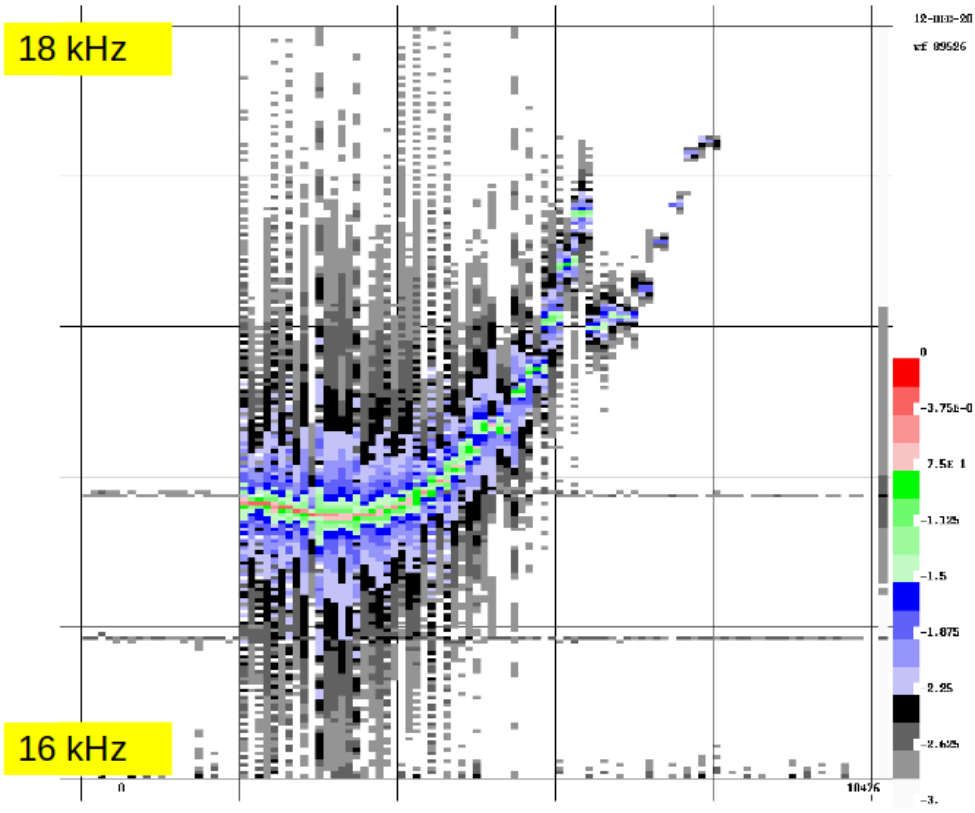

Figure 7.4: Spectrogram of the measured l=2 diocotron mode signal. The signal shown here represents the evolution of the mode in 50 s. The frequency evolution in time is due to the nonlinear relationship between frequency and amplitude.

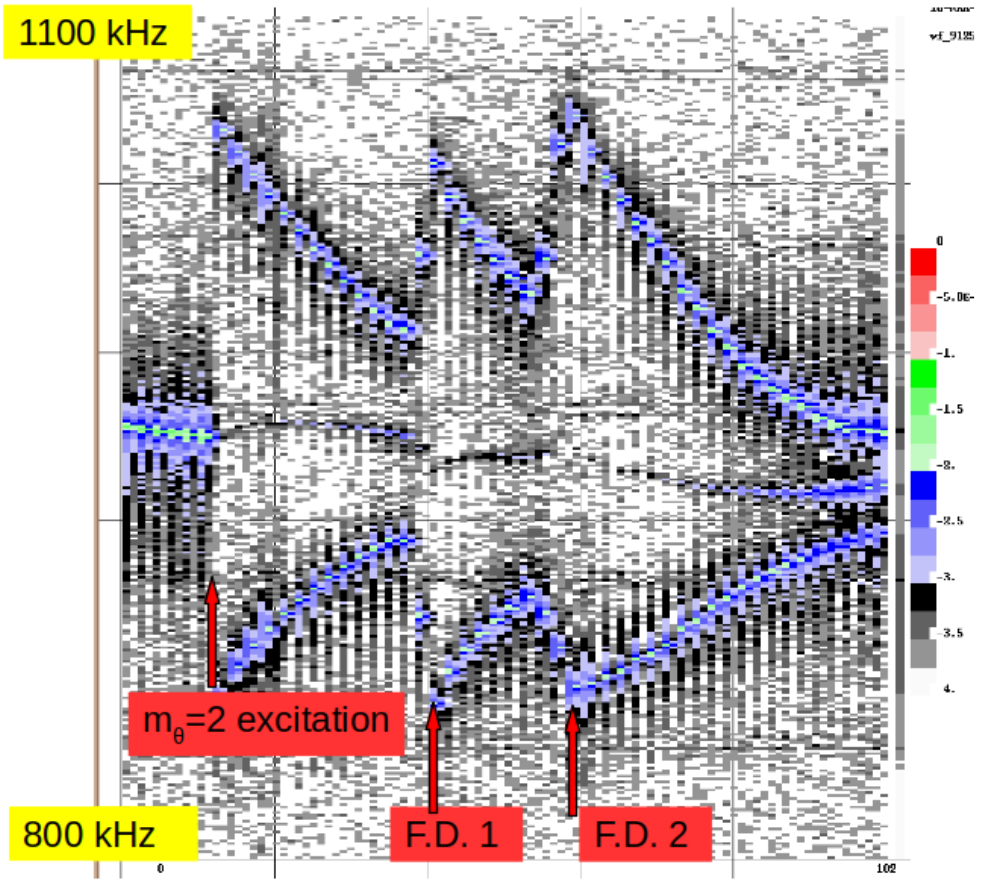

Figure 7.5: Spectrogram for the measured TG mode ($k_z = 1, m_\theta = 0, m_r = 2$) signal propagating on a plasma together with a diocotron mode subject twice to constructive feedback damping. Labelelled in red "F.D." are the instants of application of the two feedback intervals, that last 3 s.

$\Delta\nu$ decreases accordingly. So we can state that

$$\Delta\nu \propto \epsilon^n (\propto A(l = 2)) \tag{7.3}$$

with $n \geq 1$.

In fig. 7.6 the spectrogram for a ($k_z = 1, m_\theta = 0, m_r = 3$) TG mode propagating on an elliptical plasma. The temporal sequence is the same as for the $m_r = 2$ TG mode, shown in table 7.1. In this case the TG excitation is done at $\nu = 580$ kHz, $V_{pp} = 500$ mV, for 10 wave cycles, on the S4 frame, and the detection is on G8 and S7AB. It is clearly recognizable a splitting pattern, but different from the $m_r = 2$ case. Indeed we have 5 branches here: a fainter outer couple, a stronger inner couple, and the original signal, that is the weakest of all the branches, and it is at a slightly higher frequency compared to the TG mode before the diocotron mode excitation because of plasma heating.

In fig. 7.7 the spectrogram for a ($k_z = 1, m_\theta = 0, m_r = 1$) TG mode propagating on an elliptical plasma. The experimental sequence is always as in tab. 7.1. The TG excitation

t (s)	
0	injection
0.1	start squeeze
8	end squeeze
22	start TG modes excitation. Then, every 1.5 s for 50 times
30	l=2 diocotron mode excitation
49	feedback damping
52	end feedback damping
62	feedback damping
65	end feedback damping
90	ejection

Table 7.2: Experimental sequence to control the amplitude of the TG mode splitting via the feedback damping technique.

signal is at $\nu = 2.7$ MHz, $V_{pp} = 100$ mV, on the S4 frame, for 5 waves cycle, and the detection is on G8. In this case, there is no splitting. We can see several lines close to the TG modes, but they are just spurious signals, that is to say, they appear in different shapes and positions in different shots, and they do not appear to be related to the diocotron mode. Only one of these signals is a real TG mode, with $(k_z = 3, m_\theta = 0, m_r = 1)$.

In fig. 7.8 the spectrogram for the $(k_z = 1, m_\theta = \pm 1, m_r = 1)$ TG modes propagating on an elliptical plasma. It is obtained with the usual temporal sequence of 7.1. The TG excitation is at $\nu = 1430$ kHz, $V_{pp} = 3$ V on the electrodes S4A and S4C, with a phase difference between the two electrodes of $180°$, and the detection is on S7AB. Both of the modes split in two well separated branches but, contrary to what happens with the $m_r = 2$ and $m_r = 3$ modes, the original frequency mode disappear when the plasma is elliptical, and it only reappears when the diocotron mode is damped and the profile is axisymmetric again. In this case we also observe that the TG mode frequency decreases after the dissipation of the l=2 mode, because of plasma cooling.

To have a significant amount of data to perform a detailed analysis and to test the consistency of the observed phenomena, we perform 5 shots for every different TG mode. All of the features described here for the various TG modes are consistent and very repeatable: in all the experiments performed, the spectrograms always exhibit the same behavior accordingly to the TG mode excited.

7.3 Quantitative analysis and theoretical approach

We now perform a systematic analysis of the collected signals, to establish what kind of dependence there is between ϵ and $\Delta\nu$ in a more detailed form than in 7.3, and try to develop a first theoretical model for the TG waves splitting.

The diocotron mode and the TG modes are measured with two different digitizers, triggered at the same time and with the same 50 shots cycle, but with two different sample rates. Being the diocotron mode frequency $\nu_{l=2} \sim$ kHz several orders of magnitude lower than $\nu_{TG} \sim$ MHz, the diocotron mode signal is sampled at 10^2 kHz while the TG modes are sampled at 10^5 kHz. To look for a relationship between the ellipticity ϵ and the amplitude of the splitting $\Delta\nu$ defined as the difference in frequency between the higher frequency branch ν_+ and the lower frequency branch ν_-, we need to have these quantities at the same time. Therefore we cannot directly use all the data, because of the

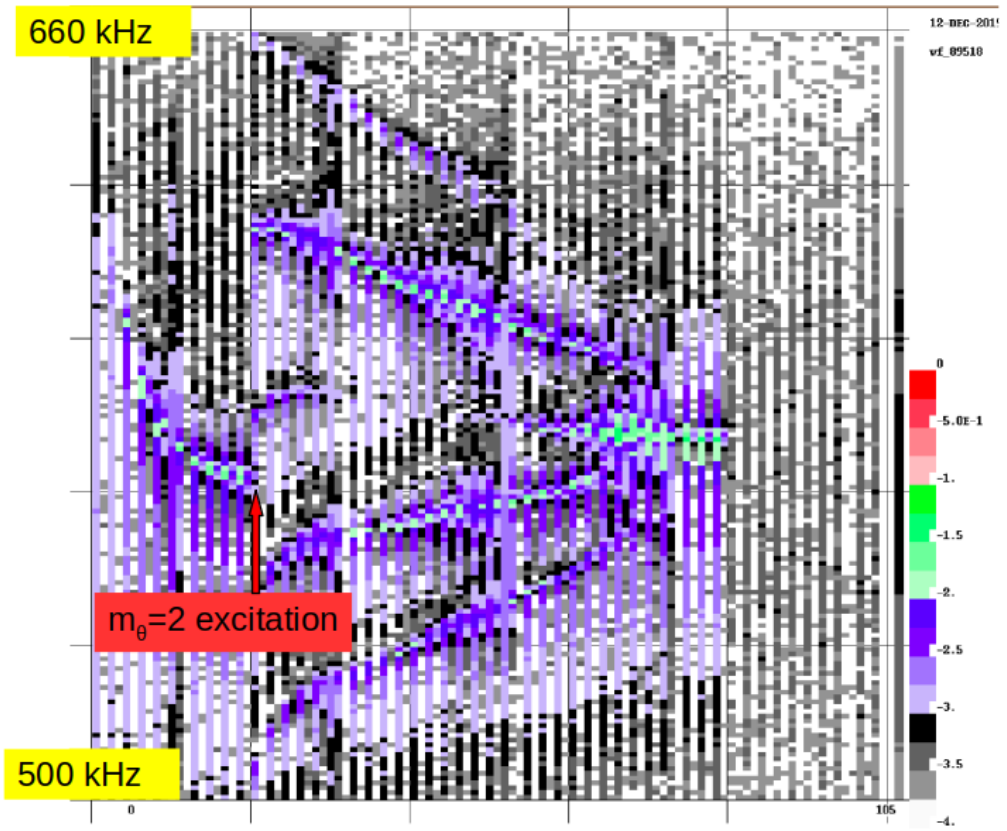

Figure 7.6: Spectrogram of the measured TG mode ($k_z = 1, m_\theta = 0, m_r = 3$) signal. Before the diocotron mode excitation, the frequency decreases because of plasma cooling. When the plasma becomes elliptical, due to the l=2 excitation, a five branch splitting appears. In this case the signal is weaker than in fig.7.3, but it is still an order of magnitude stronger than the noise level (black and grey in color scale) and the branches are easily recognizable. These branches converge again in a single frequency signal when the ellipticity fades, approximately 40 s after the excitation.

two different sample rates: only the first measurements after the digitizer is triggered, and then every 10^3 points, the TG mode signal and the diocotron mode signal are taken at the same time.

First we need to extrapolate the single branch signal from the raw signal, from which the spectrograms shown before are elaborated. To obtain the various $A_{l=2}(t)$, $\nu_{l=2}(t)$, $\nu_{+TG}(t)$, $\nu_{-TG}(t)$..., and so on, we fit the signal collected with the electrode with a sinusoidal function. We give as input the number of waves (branches), each one corresponding to a sinusoidal signal, the initial frequencies and amplitudes, that are usually deduced from the spectrograms, and the tolerance on the frequencies, usually, for the experiments shown here, of ~ 5 kHz. In figs. 7.9, 7.10 an example of the results of this fitting procedure is shown.

As explained, the single points of $(t, \nu)_{TG}$ cannot be directly related to the single points of $(t, A_{l=2})$, because they are taken at different times. But if we observe figs. 7.9 and 7.10, we can see that, during a single TG excitation (or step), frequency and amplitude are constant in time, both for the diocotron and the TG modes. Since all the points have

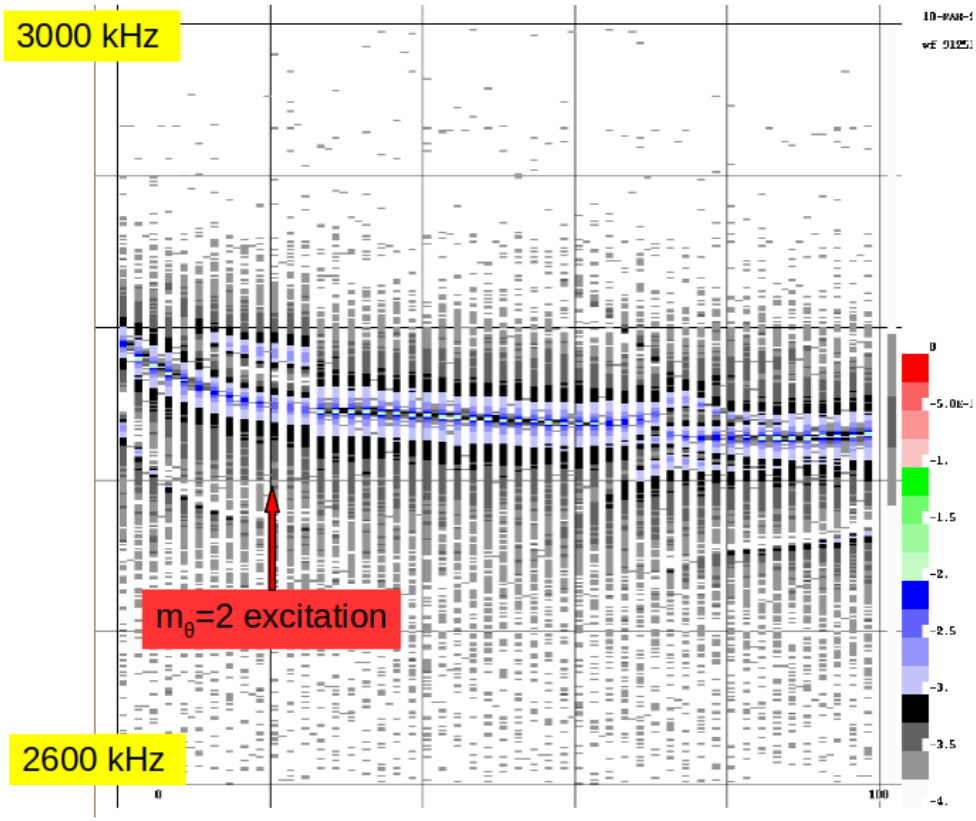

Figure 7.7: Spectrogram of the measured TG mode ($k_z = 1, m_\theta = 0, m_r = 1$) signal. Initially the frequency decreases because of plasma cooling. In this case, there is no splitting. There are some spurious signals close to the TG mode, but they differ from shot to shot and they are not related to the plasma ellipticity.

the same statistical weight, we take the average on a single TG shot (step):

$$A_{t^*} = \left(\frac{\sum_{j=1}^{N} A_j}{N} \right)_{t^*} \qquad \nu_{t^*} = \left(\frac{\sum_{j=1}^{M} \nu_j}{M} \right)_{t^*} \tag{7.4}$$

where t^* refers to one TG excitation shot (one step) and N, M refers to the number of data points in that shot. Note that N and M are not the number of measured data points, but the number of data points after the fitting procedure. Now we have data points in the form $(A_{l=2}, \nu_{+TG}, \nu_{-TG}, ...)_{t*}$ that is to say, we have unambiguously associated ellipticity of the plasma and frequency of the TG mode for any single TG mode excitation. This procedure comes without loss of significant information, because these quantities are constant for the whole duration of any measurement event t^*. In fig. 7.11 an example of plot $\Delta\nu(\epsilon)$: from this example, we can see the linear dependency $\Delta\nu \propto \epsilon^1$. This appears to hold for a wide range of ellipticity, but not for the smaller values, namely $\epsilon < 0.03$. Even though there might be some interesting and relevant details in this regime of ellipticity, we lack reliable data. Indeed, as can be noticed in fig. 7.10 for $t > 70$ ms and also in fig. 7.3, when the l=2 mode fades away and the different branches merge, the

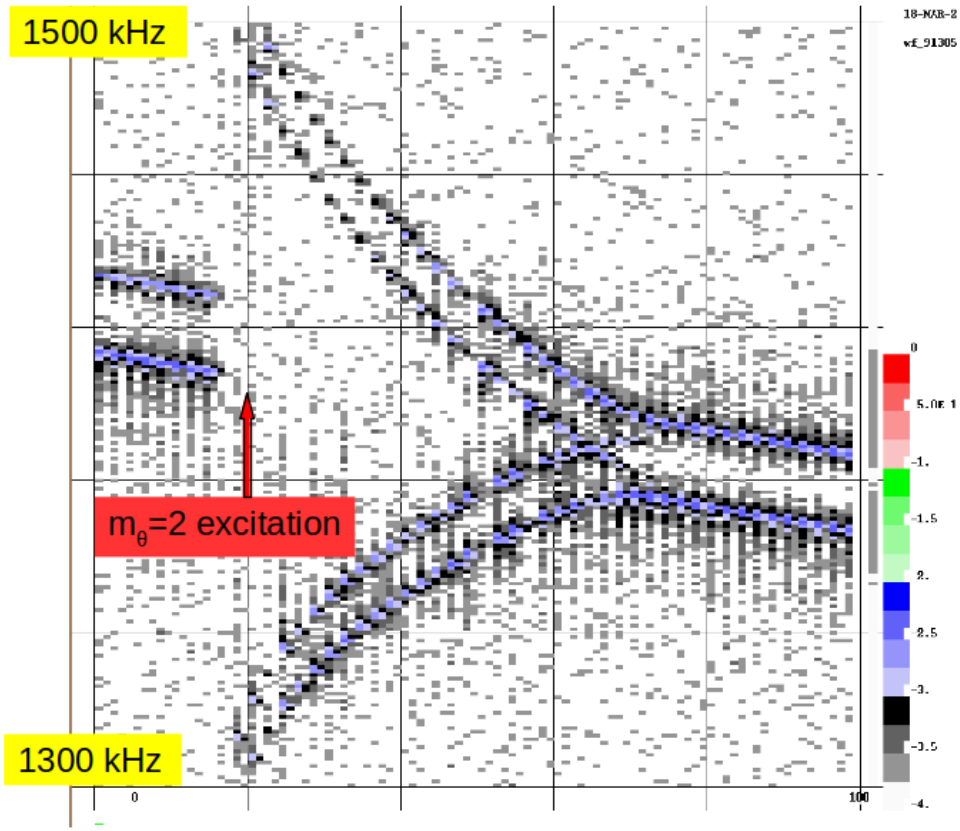

Figure 7.8: Spectrogram of the measured TG modes ($k_z = 1, m_\theta = \pm 1, m_r = 1$) signal. Referring to the signals before the diocotron mode excitation, the $m_\theta = +1$ mode is at $\nu_{m_\theta=+1} = 1430$ kHz while $\nu_{m_\theta=-1} = 1415$ kHz. Both modes split when the plasma becomes elliptical. When there is no splitting, so in the early and late phase of the experiment, the two modes frequencies decrease with the same $\frac{\partial \nu}{\partial t}$, because of plasma cooling.

fitting procedure fails to keep track of the signals, so that the frequency value for this part of the experiment cannot be trusted for our data. These considerations apply to all the different TG modes examined.
We assume there is a linear dependency, and express it in the form

$$\Delta\nu = \alpha\epsilon + \beta \tag{7.5}$$

with α and β two numerical coefficients, $\Delta\nu = \nu^+_{TG} - \nu^-_{TG}$ is the difference in frequency between the higher frequency branch ν^+_{TG} and the lower frequency branch ν^-_{TG} of the TG splitted mode and ϵ is the ellipticity of the plasma as defined in 7.2. The linearity hypothesis, with its experimental limitations, holds for all the different TG modes we have been dealing with: they all show a linear behavior like in the plot in fig. 7.11.

In fig. 7.12 all the data points for one of the two experimental campaigns, fitted with the linear law of eq. 7.5.
In the table 7.3, the results for the linear fitting of the ($k_z = 1, m_\theta = 0, m_r = 2$) TG mode splitting are given.

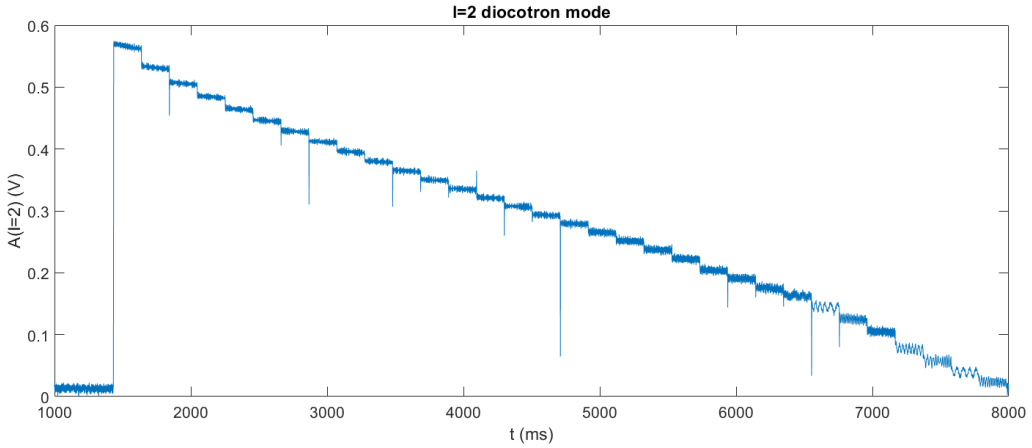

Figure 7.9: Amplitude evolution in time of the diocotron mode signal obtained by fitting with a sinusoidal wave the measured signal in fig. 7.4. The step-like structure is due to the digitizer being triggered every 1 s, while the single step measurement lasts $\sim$ 200 ms. So between two adjacent steps there is a noticeable difference in amplitude originated when the signal is not being measured while it continues to damp.

Data set	α	β
Nov 19	725.0	18.7
Mar 20	702.8	11.5

Table 7.3: Results of the linear fit for the experimental data for the $(k_z = 1, m_\theta = 0, m_r = 2)$ TG mode splitting.

In the case of $(k_z = 1, m_\theta = 0, m_r = 3)$ TG mode, the same considerations apply, but there is a complication in the analysis. We can already see in fig. 7.6, and with better detail in fig.7.13 that the $m_r = 3$ branches are weaker, compared for example to the amplitude of $m_r = 2$ branches. Having such a weak signal affects the fitting procedure, through which we establish ν^+_{TG} and ν^-_{TG}, see fig. 7.15.
First of all, we cannot fit the two outer branches that are clearly recognizable in the spectrogram in fig. 7.6. Moreover, although the two inner branches can be fit, the results of the fitting procedure in this case are not very accurate, showing abrupt oscillations and spikes in the $\nu^{\pm}_{TG}(t)$ curve that are not real and do not have any physical meaning, but are just artifacts from the fit. This issue greatly increases the error in the frequency calculated as in 7.4, so that now for the arithmetical average we only take into account those points for which $A(TG) > 0.03$ V. We have, on average for every "step" t^*, a standard deviation on the frequency of $\delta\nu^{\pm} \sim 8$ kHz for the $m_r = 3$ mode while, for comparison, the standard deviation on the frequency for the $m_r = 2$ mode is $\delta\nu^{\pm} \sim 2$ kHz.
The results for the linear fitting of the $(k_z = 1, m_\theta = 0, m_r = 3)$ TG mode splitting are given in the table 7.4 and shown in fig. 7.14. For this TG mode, the error on the frequency of the first data set is such that the points are too spread, and they do not satisfy the linear relationship 7.5.
For the $(k_z = 1, m_\theta = \pm 1, m_r = 1)$ TG mode, the signal is even weaker then the $(k_z = 1, m_\theta = 0, m_r = 3)$ mode, compare the color scales of the signal in fig. 7.6 and

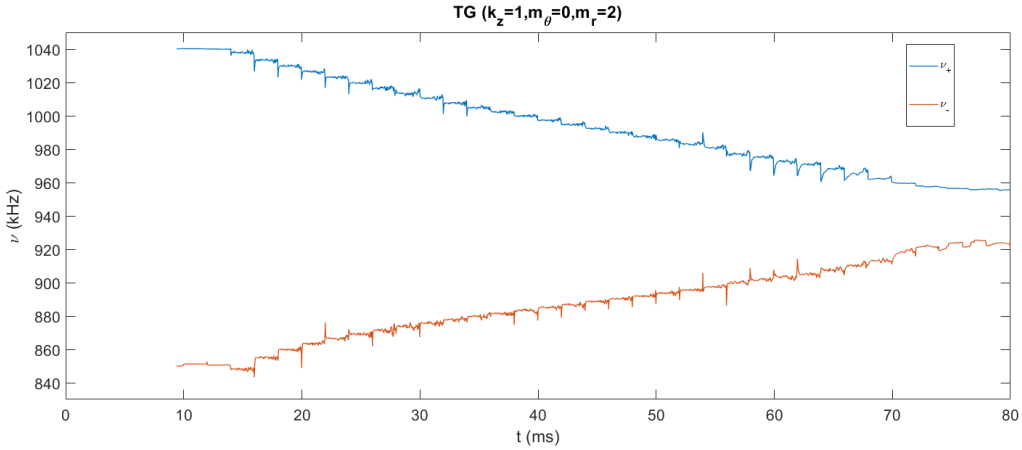

Figure 7.10: Frequency evolution in time of the TG $(k_z = 1, m_\theta = 0, m_r = 2)$ mode obtained by fitting with three sinusoidal waves the measured signal in fig. 7.3. The central branch is not displayed because the fitting procedure was not accurate for that particular branch, the signal being too weak. The step-like structure is due to the digitizer being triggered every 1 s, while the single step measurement lasts ~ 5 ms. So between two adjacent steps there is a noticeable difference in frequency, for both the branches, originated when the signal is not being measured while the plasma keeps cooling, hence the TG mode frequency changes.

Data set	α	β
Nov 19	/	/
Mar 20	279.5	13.8

Table 7.4: Results of the linear fit for the experimental data for the $(k_z = 1, m_\theta = 0, m_r = 3)$ TG mode splitting.

fig. 7.8. The fit procedure completely fails to give a proper $\nu(t)$ so, in this case, the data points are extrapolated from the spectrograms. $A(l = 2)_{t^*}$ is still calculated with (7.4), but $(\nu_\pm = 1)_{t^*}$ is directly evaluated from the spectrograms. Then, the various couples $(\epsilon, \Delta\nu)_{t^*}$ are easily created, thanks to the different shots t^* being well separated and clearly distinguishable.

In the table 7.5, the results of the linear fitting for the TG $(k_z = 1, m_\theta = \pm 1, m_r = 1)$ mode. Only one experimental data set is available for this mode. The results for this fit, even though we still have few data, suggest that the two modes behave in the same way, as can be noticed in the spectrogram fig. 7.8.

Let us try to create a theoretical model for the splitting focusing on the $m_\theta = 0$ TG modes.

Mode	α	β
$m_\theta = 1$	683.4	-4.7
$m_\theta = -1$	708.9	-10.9

Table 7.5: Results of the linear fit for the experimental data for the $(k_z = 1, m_\theta = \pm 1, m_r = 1)$ TG mode splitting.

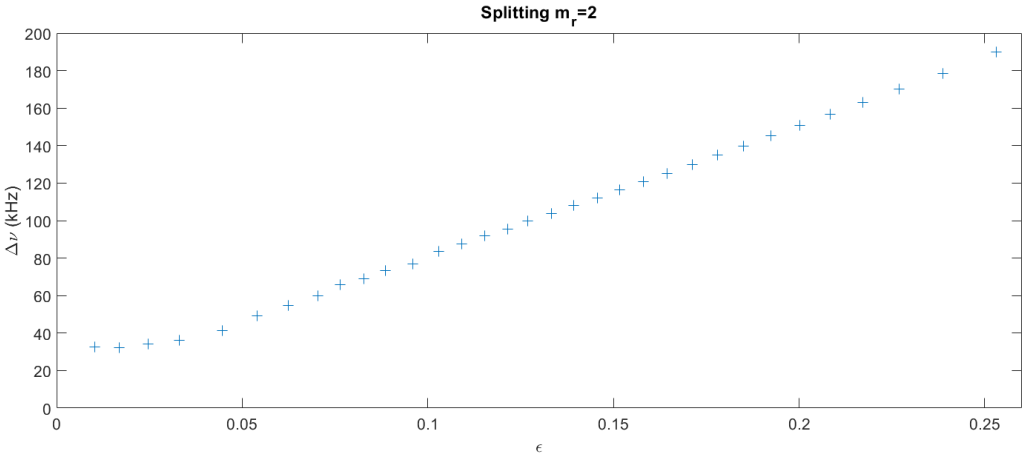

Figure 7.11: Difference in frequency between upper and lower branch $\Delta\nu = \nu^+_{TG} - \nu^-_{TG}$ vs ellipticty ϵ for the $(k_z = 1, m_\theta = 0, m_r = 2)$ TG mode. These data come from the fitting of the signal in fig. 7.10, so they come from one single experimental shot.

If we look at the TG mode dispersion relation (3.21), their frequency are determined largely by the zeros of the Bessel functions $j_{m_\theta - 1,n}$. In fact, for $k_z R_w << 1$ both the $m_\theta = 0$ and $m_\theta = 2$ modes have frequencies, in the rotating frame, determined by $k_\perp R_p \sim j_{1,n}$ while $m_\theta = 4$ modes have $k_\perp R_p \sim j_{3,n}$ and so on. Moreover, as can be seen in fig. 7.16, $j_{1,1}$ is not degenerate, $j_{1,2}$ has one near-degeneracy, $j_{1,3}$ has two near degeneracies and so on. This is suspiciously similar to what observed with the experiments: no splitting for $m_r = 1$, one splitting for $m_r = 2$, two splittings (two couples of branches) for $m_r = 3$. It is possible that what we see as a splitting, is actually a degeneracy removal due to the elliptical deformation. To prove this analytically is a hard task, but we can support this hypothesis thanks to figs. 7.18 and 7.19 that show, solving numerically the dispersion relations, how, when the plasma becomes elliptical, the $m_\theta = \pm 2$ modes assume new, non degenerate, dispersion relations. This case could correspond to what is observed for the $(k_z = 1, m_\theta = 0, m_r = 2)$ TG mode. An elliptical density perturbation not only shifts the frequencies of the modes, but it also removes the orthogonality, allowing their mixing: the $m_\theta = 2$ modes pick up the $m_\theta = 0$ components resulting in the splitting pattern.

The theory for the $(k_z = 1, m_\theta = 0, m_r = 2, 3)$ does not apply for the $(k_z = 1, m_\theta = \pm 1, m_r = 1)$ modes, because for $m_r = 1$ there is no degeneracy in the dispersion relation: there are no other modes with these frequencies. We have to develop another theory, hinting at the fact that these modes have a non zero azimuthal symmetry, being $m_\theta \neq 0$. First, as can be measured from the spectrogram in fig. 7.8, the difference in frequency between the $m_\theta = \pm 1$ TG modes is $\nu_{m_\theta = +1} - \nu_{m_\theta = -1} = 2\nu_{E\times B}$ because of the Doppler shift between the modes, that rotate in opposite directions on the plasma column. The potential perturbation due to the $(k_z = 1, m_\theta = \pm 1, m_r = 1)$ TG modes is:

$$\begin{aligned} m_\theta = +1: &\qquad \delta\phi = \exp(i\theta - i\omega_{+1}t)\cos(kz)K_{+1}(r) \\ m_\theta = -1: &\qquad \delta\phi = \exp(i\theta - i\omega_{-1}t)\cos(kz)K_{-1}(r) \end{aligned} \tag{7.6}$$

with $K_{\pm 1}$ the Bessel functions of the first kind. When we excite a l=2 diocotron mode and the plasma becomes elliptical, it reaches a new equilibrium state. The ellipticity ϵ

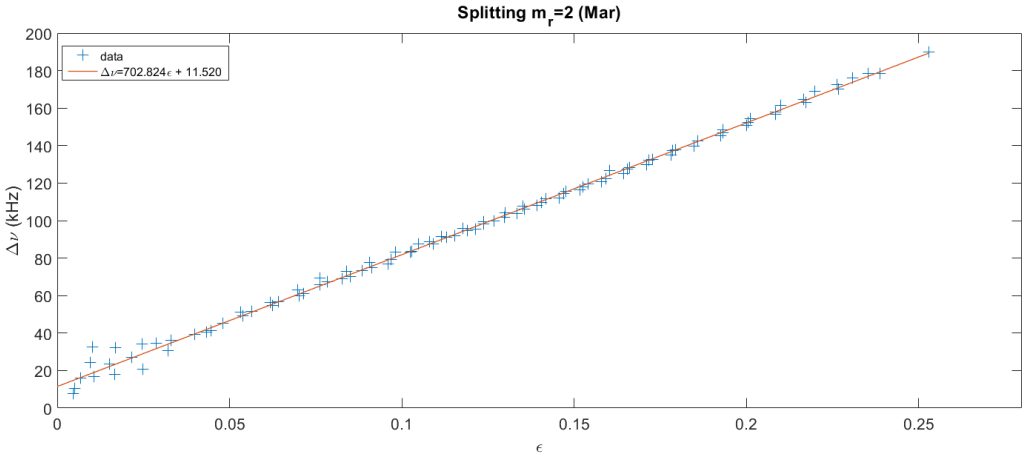

Figure 7.12: Linear fit of one of the experimental data sets for the $(k_z = 1, m_\theta = 0, m_r = 2)$ TG mode. The points with $\epsilon < 0.03$ are not included in the fit. The data come from all the shots made for this TG mode during the March 2020 experimental session.

generates a density perturbation $\Delta N = f(r)\cos(2\theta)$, time independent in this model, that causes a new density and electrostatic potential equilibrium configuration. In the frame of the diocotron mode $\theta_{lab} = \theta + \omega_{l=2}t$, we have

$$\begin{aligned} m_\theta = +1: \quad & \delta\phi = \exp(i\theta - i\omega_{+1}t)\cos(kz)K_{+1}(r) + \\ & + A'\epsilon exp(-i\theta - i\omega_{+1}t - i\Delta\omega_1 t)\cos(kz)K'_{+1}(r) \\ m_\theta = -1: \quad & \delta\phi = \exp(i\theta - i\omega_{-1}t)\cos(kz)K_{-1}(r) + \\ & + B'\epsilon exp(i\theta - i\omega_{-1}t - i\Delta\omega_{-1}t)\cos(kz)K'_{-1}(r) \end{aligned} \tag{7.7}$$

with A' and B' numerical constants, $\Delta\omega = \Delta\omega(\epsilon)$ and $K'_{\pm 1}$ first order Bessel functions that solve the Poisson equation for the new equilibrium potential $\phi + \delta\phi$. The ellipticity changes the potential and therefore the TG mode frequencies. In the diocotron mode frame, we still have only two frequencies. Returning in the lab frame we have:

$$\begin{aligned} m_\theta = +1: \quad & A\exp(i\theta_{lab} - i(\omega_{+1} - \omega_{l=2})t + B\exp(-i\theta_{lab} - i(\omega_1 + \omega_{l=2} - \Delta\omega_{+1}(\epsilon))t \\ m_\theta = -1: \quad & C\exp(-i\theta_{lab} - i(\omega_{-1} + \omega_{l=2})t + D\exp(i\theta_{lab} - i(\omega_1 - \omega_{l=2} - \Delta\omega_{-1}(\epsilon))t \end{aligned} \tag{7.8}$$

with A, B, C, D numerical constants. There are now four frequencies:

$$2\pi\nu_{1,2} = \omega_1 \pm \omega_{l=2} \qquad 2\pi\nu_{3,4} = \omega_{-1} \pm \omega_{l=2} - \Delta\omega_{\pm 1}(\epsilon) \tag{7.9}$$

This simple theory, that relies on both the diocotron mode and the TG modes to have a non-zero azimuthal component, could explain what it is observed in fig. 7.8: when the dioctron mode is excited, the original TG modes frequency disappear, and are replaced by four new frequencies signals, with frequencies that depend, as estimated in the limits of our data analysis, linearly on the plasma ellipticity: $\Delta\omega \propto \epsilon^1$. As the diocotron mode damps, $\epsilon \to 0$, the two initial TG modes frequencies are restored.

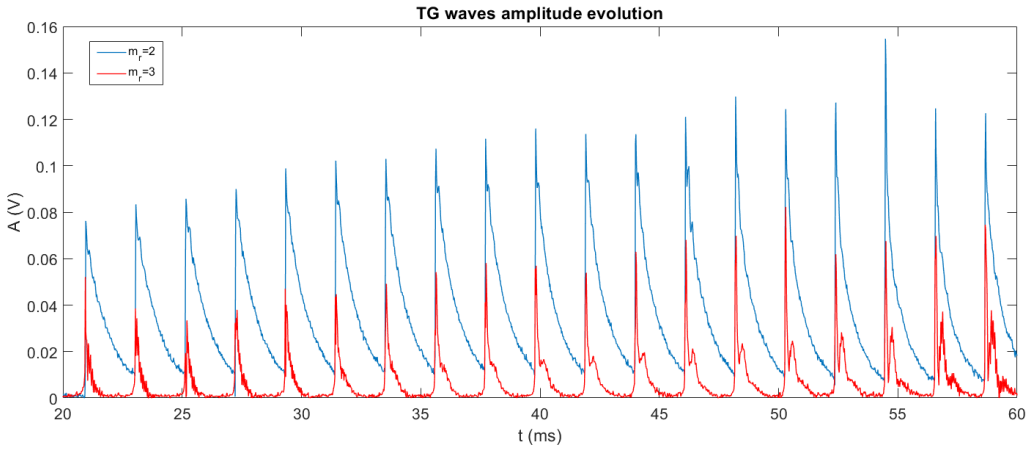

Figure 7.13: Amplitude evolution in time for two different TG modes. In blue the evolution of the upper branch of the $m_r = 2$ TG mode, while in red the evolution of the inner upper branch of the $m_r = 3$ TG mode. There is no difference in the amplitude evolution of upper and lower branches. Each spike corresponds to a different TG excitation.

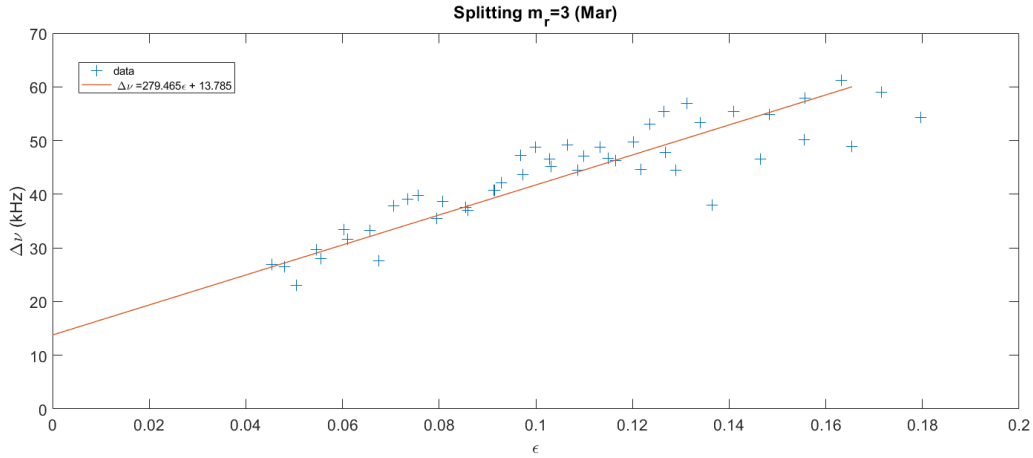

Figure 7.14: Linear fit of the March 2020 data sets for the $(k_z = 1, m_\theta = 0, m_r = 3)$ TG mode. The points with $\epsilon < 0.03$ are not included in the fit. The data come from all the shots made for this TG mode during the March 2020 experimental session.

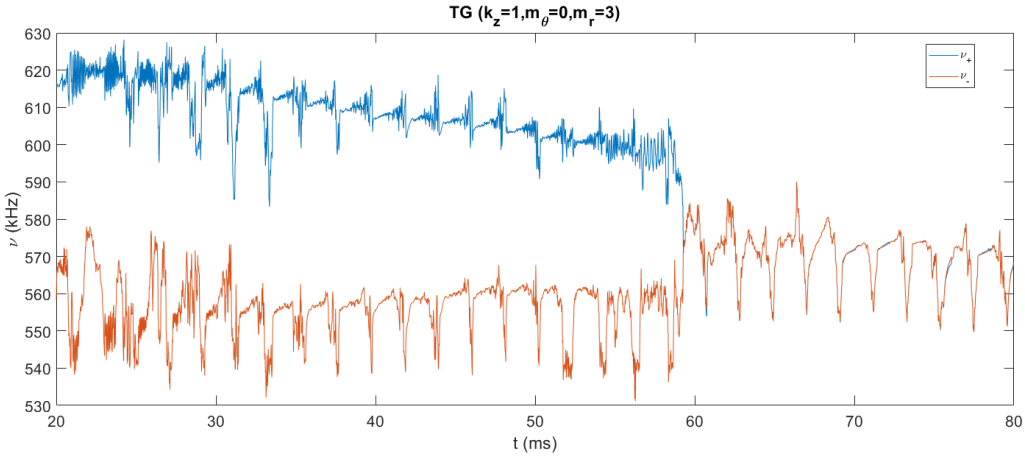

Figure 7.15: Frequency evolution in time of the TG $(k_z = 1, m_\theta = 0, m_r = 3)$ mode obtained by fitting with two sinusoidal waves the measured signal in fig. 7.3. The central branch and the two outer branches have a signal too weak to be properly fit. The step-like structure is due to the digitizer being triggered every 1 s, while the single step measurement lasts ~ 5 ms. The abrupt oscillations in frequency are not real, see fig7.6, but are the results of a the fitting procedure on faint signals. Hence further manipulation and data selection are required to use the experimental data for this TG mode.

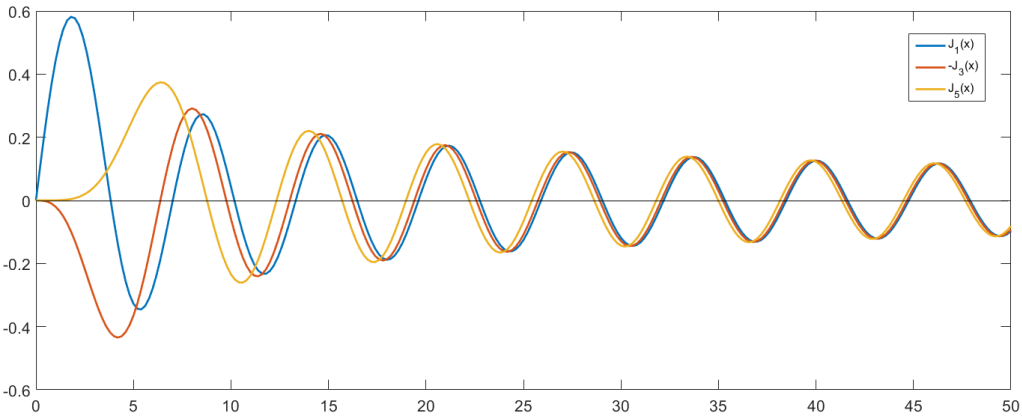

Figure 7.16: J_1, -J_3 and J_5 Bessel functions. As their argument gets bigger, their respective zeros $j_{m,n}$ become more degenerate.

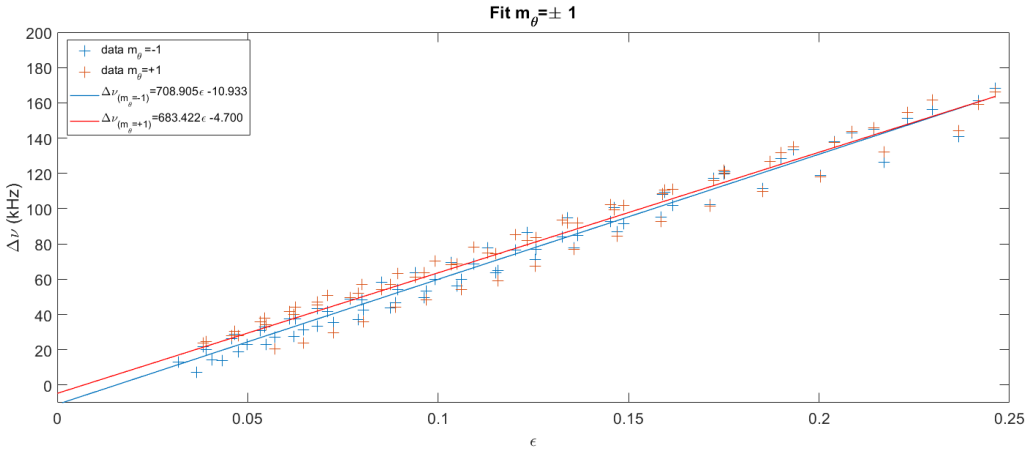

Figure 7.17: Linear fit of one of the experimental data set for the $(k_z = 1, m_\theta = \pm 1, m_r = 1)$ TG modes. In red, $m_\theta = +1$, in blue $m_\theta = -1$.

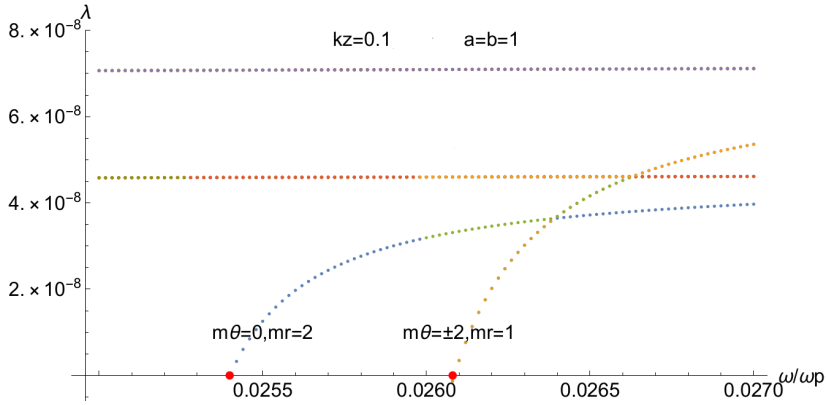

Figure 7.18: Numerical solution of the dispersion relationship (3.21) for the $(k_z = 1, m_\theta = 0, m_r = 2)$ (blue dots) and $(k_z = 1, m_\theta = \pm 2, m_r = 1)$ (yellow dots) TG modes in the case of a circular plasma (a=b=1). The two $(m_\theta = \pm 2)$ modes are degenerate.

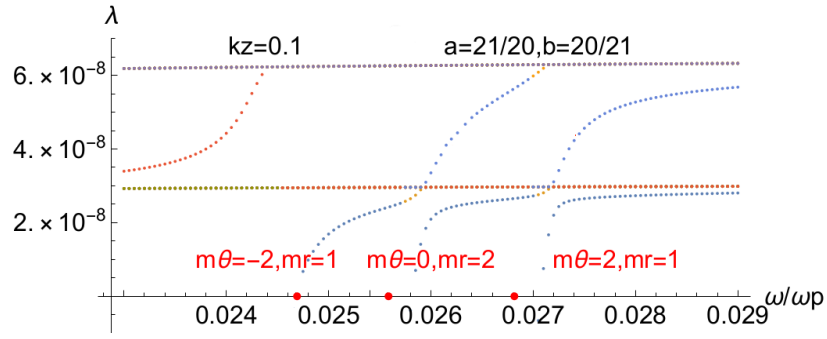

Figure 7.19: Numerical solution of the dispersion relationship (3.21) for the $(k_z = 1, m_\theta = 0, m_r = 2)$ and $(k_z = 1, m_\theta = \pm 2, m_r = 1)$ TG modes in the case of an elliptical plasma (a≠b). The two $(m_\theta = \pm 2)$ modes are no longer degenerate.

Conclusions and future directions

In this thesis work we present the results of experiments performed on pure electron plasmas confined in Penning-Malmberg traps in the frame of excitation and control of non-linear waves. The goal of this experimental work is to improve and develop new techniques to control and analyze waves propagating on magnetized pure electron plasma columns, and provide new insights on their phenomenology, helping to develop more refined theoretical models in the context of non-neutral plasma physics and, via the fluid analogy, of fluid physics. Penning traps are also widely used in the confinement and manipulation of antimatter plasmas, and it can be expected that a deeper understanding of these waves will contribute to the creation of new tools for a range of applications in the field of confined charged particles in electromagnetic traps.
With the Eltrap device, experiments on the high order diocotron mode excitation via the rotating electric field technique are performed. We successfully show that this technique is an efficient and promising tool, but with some limitations on the temporal control of the instabilities. An improvement of the technique in this sense is achievable recurring to an excitation drive that slowly changes in frequency, inducing autoresonance. In the context of this work, future works include:

- To upgrade the electrostatic diagnostic to have a more precise description of the diocotron modes excitation with $l > 3$.
- To extend the investigation of the autoresonance parameters, with different chirp rates and for different modes.
- Once improved the autoresonant drive excitation and refined diagnostics, to provide a more thorough characterization of the cascade decay of the modes and their damping.
- To study in detail the nonlinear relationship between frequency and amplitude, exploiting all its feature, to support the development of a theoretical model.

With the CamV apparatus we investigate the interaction of TG and diocotron $l = 2$ modes propagating on the same plasma columns, that results in a peculiar TG modes splitting pattern in the Fourier space. This phenomenon has never been observed before, and we provide, in the limits of our instrumentation, a detailed description of its features. From this experimental characterization, we develop a rough theoretical model that involves a degeneracy removal in the TG dispersion relation and the mixing of orthogonal waves due to the non-axisymmetric (elliptical) plasma profile. In the context of this work, future directions are:

- To increase the statistics and refine the measurements on those modes with a very weak signal, such as the $(k_z = 1, m_\theta = 0, m_r = 3)$ mode, and eventually extend the experiments to other known TG modes experimentally accessible such as the $(k_z = 1, m\theta = 2, m_r = 1)$ TG mode.

- To perform tailored experiments for very low $(\epsilon < 0.05)$ and very high $(\epsilon > 0.2)$ ellipticity regime, to test the validity regime of the linearity hypothesis for all the TG modes.

- To further develop the theory, supported by new experimental data, aiming at creating a generalized and unified theory for all the TG modes propagating on a non-axisymmetrical plasma column.

In the frame of non-linear wave theory in pure electron plasma, these two experimental works can be of mutual interest! We can think to study the behavior of TG modes propagating on a plasma profile subject to high order diocotron modes excited with the rotating electric field technique, and observe what happens when a TG wave propagates on a triangular, squared, pentagonal profile and so on. Vice-versa, we can devise the TG modes as an indirect, on-line diagnostics for the evolution of diocotron modes on the same plasma column.

Appendices

APPENDIX A

Charge collector diagnostic: total plasma charge measurement

On the side of the trap opposite to the optical diagnostic, there is an aluminum circular charge collector with diameter $\phi = 100$ mm, enough to cover the whole trap area. If we eject the plasma on the charge collector, by grounding the confinement electrode on this side, we can obtain the total charge of the plasma by measuring the charge/discharge process on the collector.

In fig A.1 a typical charge discharge signal. The process appears as a sudden, vertical charge (μs), followed by a slow discharge (ms), with an exponential growth in time. Given the resistance of oscilloscope, set to $R = 10^6\ \Omega$, that makes the collector resistance negligible, and taking into account the unavoidable presence of parasitic capacity, the system can be considered as an RC circuit, where

$$V(t) = V_0 \exp(-\frac{t}{RC}) = Q_0/C \exp(-\frac{t}{RC}) \tag{A.1}$$

$V(t)$ being the measured quantity and Q_0 the total plasma charge.
When the electrons impact the collector, it appears as an instant process, because $\nu_{ee} \sim 10^6$ Hz$>> 1/RC \sim 10^3$ Hz. Thus, by the time the discharge occurs, all the electrons have impacted the charge collector, and we are actually measuring the total charge of the previously confined plasma. Fitting the data with eq.A.1 we can extrapolate Q_0 and C, that usually is $C \sim 400$ pF.
A more general method does not consider the charge instantaneous, but rather

$$Q_0 = \int_{t_0}^{T} \frac{V(t)}{R} dt \tag{A.2}$$

where t_0 is the start time of the charging process, and T is a time big enough to consider the discharge complete. This is useful if we are interested in slower particles, such as during a parallel temperature measurement, or to measure the total charge associated with the positive ions (much less energetic than the electrons) generated with the RF excitation.

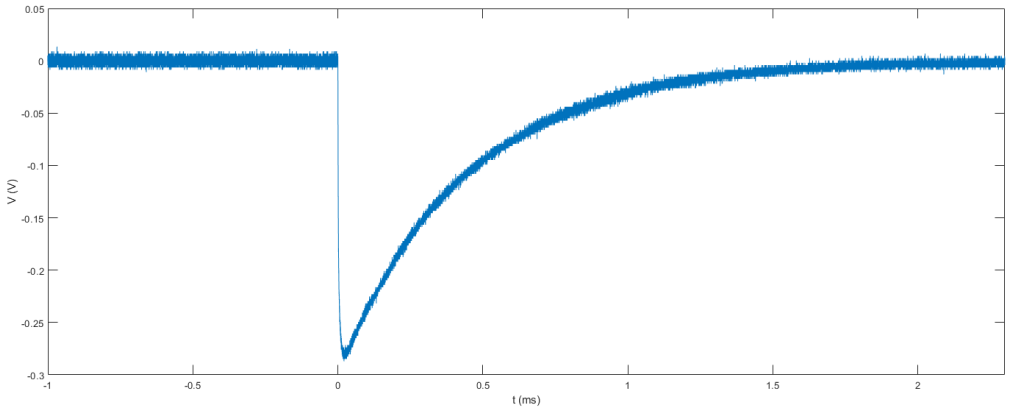

Figure A.1: Typical charge/discharge signal registered when the plasma impacts the charge collector. The time scale is in ms: while the discharge takes few ms, the charge process occurs in the μ s range. In this case, the total charge of the plasma is $Q_p = -120$ pC.

APPENDIX B

CCD image noise removal and centering

All the phosphor screen images collected with the CCD camera need to be processed to get rid of noise and systematic errors. Firstly, we take 80 images with 1 ms exposure without any plasma in the trap. The average of these images is the dark background, and it is subtracted from every CCD image: this procedure allows us to get rid of any unfiltered and undesired background luminosity and CCD noise. We now need to properly identify the phosphor screen edge, so to distinguish the trap area from the area outside of the trap. By taking a 1 s exposure image, without any plasma in the trap, we can clearly identify the phosphor screen border and the trap edge: all the pixels outside the trap area are set to zero luminosity.
Due to minor misalignments, the phosphor screen center does not coincide with the magnetic trap center. To identify the trap center, we generate a plasma column whose radius is not too big, and we eject it on the screen: due to the RF generation, and since we are not applying any feedback damping, the plasma has a relevant $l = 1$ mode. By overwriting several images of the plasma subject to the diocotron mode, they describe a circumference, whose center is actually the real trap center, the point around which the center of the plasma column subject to the $l = 1$ diocotron mode revolves. In fig. B.1 an example of this procedure. Calculating the charge center of every plasma column, we fit these points with a circumference, whose center is the trap center.
To calibrate the CCD and convert the luminosity in charge density, we calculate the total plasma charge Q_p with the collector as explained in appendix A. When the same plasma (within the shot to shot reproducibility limits) is ejected on the phosphor screen, it generates a total luminosity I_{tot}, that only depends on the total charge, not on the plasma characteristics. Therefore, the 3D charge density on the j-pixel is

$$n_j = \frac{Q_p}{I_{tot} A_p L} I_j \tag{B.1}$$

where A_p is the pixel area (in length unit), that depends on the camera chosen binning, and L is the plasma length that can be calculated as confinement length or, for more accurate results, with a Poisson equation solver.
Of course, all these procedure needs to be done with the same pixel binning and phosphor screen voltage.

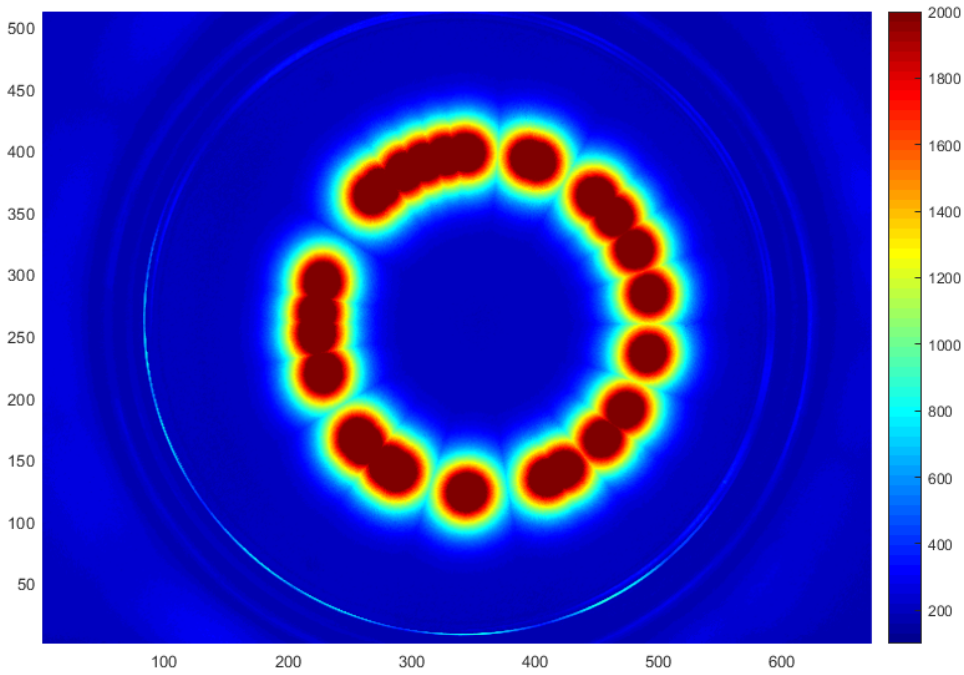

Figure B.1: Superposition of different shots to identify the trap center. The image is purposely over-saturated, also to show the phosphor screen edges (outer light blue circle) and the trap edges (inner light blue circle).

Bibliography

[1] J. H. Malmberg and J. S. deGrassie, "Properties of nonneutral plasma", *Phys. Rev. Lett.*, vol. 35, p. 577, 1975.

[2] T. M. O'Neil, "Trapped plasmas with a single sign of charge", *Phys. Today*, vol. 52, p. 24, 1999.

[3] K. Blaum, "High-accuracy mass spectrometry with stored ions", *Phys. Rep.*, vol. 425, pp. 1–78, 2006.

[4] I. J. Amster, "Fourier transform mass spectrometry", *J. Mass Spectrom.*, vol. 31, pp. 1325–1337, 1996.

[5] M. Audi and M. de Simon, "Ion pumps", *Vacuum*, vol. 37, pp. 629–636, 1987.

[6] M. Ahmadi *et al.*, "Investigation of the fine structure of antihydrogen", *Nature*, vol. 578, pp. 375–380, 2020.

[7] G. B. Andresen *et al.*, "Antimatter plasmas in a multipole trap for antihydrogen", *Phys. Rev. Lett.*, vol. 98, p. 023 402, 2007.

[8] G. Gabrielse, R. Kalra, W. S. Kolthammer, R. McConnell, P. Richerme, D. Grzonka, W. Oelert, T. Sefzick, M. Zielinski, D. W. Fitzakerley, M. C. George, E. A. Hessels, C. H. Storry, M. Weel, A. Mullers, and J. Walz, "Trapped antihydrogen in its ground state", *Phys. Rev. Lett.*, vol. 108, p. 113 002, 2012.

[9] G. B. Andresen *et al.*, "Confinement of antihydrogen for 1,000 seconds", *Nature Physics*, vol. 7, pp. 558–564, 2011.

[10] J. Fajans and C. M. Surko, "Plasma and trap-based techniques for science with antimatter", *Phys. Plasmas*, vol. 27, no. 3, p. 030 601, 2020.

[11] M. Ahmadi *et al.*, "Enhanced control and reproducibility of non-neutral plasmas", *Phys. Rev. Lett.*, vol. 120, p. 025 001, 2 2018.

[12] N. C. Hurst, "Electron vortices subject to imposed strain flows", PhD thesis, University of California, San Diego, 2018.

[13] N. C. Hurst, J. R. Danielson, D. H. E. Dubin, and C. M. Surko, "Experimental study of the stability and dynamics of a two-dimensional ideal vortex under external strain", *J. Fluid Mech.*, vol. 848, p. 256, 2018.

[14] S. Chen, G. Maero, and M. Romé, "Spectral analysis of forced turbulence in a non-neutral plasma", *J. Plasma Phys.*, vol. 83, no. 3, p. 705 830 303, 2017.

[15] F. Lepreti, M. Romé, G. Maero, B. Paroli, R. Pozzoli, and V. Carbone, "Scaling properties and intermittency of two-dimensional turbulence in pure electron plasmas", *Phys. Rev. E*, vol. 87, p. 063 110, 2013.

[16] C. F. Driscoll and K. S. Fine, "Experiments on vortex dynamics in pure electron plasmas", *Phys. Fluids B*, vol. 2, pp. 1359–1366, 1990.

[17] J. S. deGrassie and J. H. Malmberg, "Waves and transport in the pure electron plasma", *Phys. Fluids*, vol. 23, no. 1, pp. 63–81, 1980.

[18] M. R. Stoneking, J. P. Marler, B. N. Ha, and J.Smoniewski, "Experimental realization of nearly steady-state toroidal electron plasmas", *Phys. Plasmas*, vol. 16, p. 055 708, 2009.

[19] R. C. Davidson, *An Introduction to the Physics of Nonneutral Plasmas.* Addison-Wesley Publishing Company, 1990.

[20] W. D. White, J. D. Malmberg, and C. F. Driscoll, "Resistive wall destabilization of diocotron waves", *Phys. Rev. Lett.*, vol. 49, 1822, 1982.

[21] A. A. Kabantsev and C. F. Driscoll, "Diocotron instabilities in an electron column induced by a small fraction of transient positive ions", in *Non-Neutral Plasma Physics V*, vol. AIP Conf. Proc. 692, pp. 61-68, 2003.

[22] K. S. Fine and C. F. Driscoll, "The finite length diocotron mode", *Phys. Plasmas*, vol. 5(3), p. 601, 1998.

[23] T. J. Hilsabeck, "Finite length and trapped-particle diocotron modes", PhD thesis, University of California, San Diego, 2003.

[24] J. M. Kriesel, "Experiments on viscous and asymmetry-induced transport in magnetized, pure-electron plasmas", PhD thesis, University of California, San Diego, 1999.

[25] G. Bettega, B. Paroli, R. Pozzoli, and M. Romé, "Excitation of the l=3 diocotron mode in a pure electron plasma by means of a rotating electric field", *J. Appl. Phys.*, vol. 105, 053303, 2009.

[26] L. Patricelli, "Eccitazione di modi di diocotron in un plasma non neutro mediante l'applicazione di campi rotanti a radiofrequenza", BS thesis, Università degli Studi di Milano, 2016.

[27] D. H. E. Dubin, "Trapped charged particles: A graduate textbook with problems and solutions", in, R. T. M. Knoop N. Madsen, Ed. World Scientific, 2016, ch. Penning Traps and Plasma Modes.

[28] F. Anderegg, "Physics with trapped charged particles", in, R. T. M. Knoop N. Madsen, Ed. Imperial College Press, 2014, ch. Waves in Non-Neutral Plasmas.

[29] J. R. Danielson, D. H. E. Dubin, R. G. Greaves, and C. M. Surko, "Plasma and trap-based techniques for science with positrons", *Rev. Mod. Phys.*, vol. 87, pp. 247–306, 2015.

[30] S. A. Prasad and T. M. O'Neil, "Waves in a cold pure electron plasma of finite length", *Phys. Fluids*, vol. 26, p. 665, 1983.

[31] A. W. Trivelpiece and R. W. Gould, "Space charge waves in cylindrical plasma columns", *J. Appl. Phys.*, vol. 30, 1784, 1959.

[32] G. Maero, "Generation, dynamics and coherent structures in rf-generated trapped non-neutral plasmas", *Il Nuovo Cimento C*, vol. 40, no. 90, 02 2017.

[33] G. Bettega, R. Pozzoli, and M. Romé, "Multiresolution analysis of the two-dimensional free decaying turbulence in a pure electron plasma", *New J. Phys*, vol. 11, 053006, 2009.

[34] M. Romé, S. Chen, and G. Maero, "Structures and turbulent relaxation in non-neutral plasmas", *Plasma Phys. Control. Fusion*, vol. 59, p. 014 036, 2017.

[35] M. Amoretti, G. Bettega, F. Cavaliere, M. Cavenago, F. De Luca, R. Pozzoli, and M. Romé, "Cylindrical penning trap for the study of electron plasmas", *Rev. Sci. Instrum.*, vol. 74, no. 9, p. 3991, 2003.

[36] G. Maero, S. Chen, R. Pozzoli, and M. Romé., "Low-power radio-frequency excitation as a plasma source in a penning–malmberg trap: A systematic study.", *J. Plasma Phys.*, vol. 81, no. 5, p. 495 810 503, 2015.

[37] G. Maero, R. Pozzoli, M. Romé, S. Chen, and M. Ikram, "Axial heating and temperature of rf-excited non-neutral plasmas in penning-malmberg traps", *J. Inst.*, vol. 11, C09007, 2016.

[38] B. Paroli, F. D. Luca, R. Pozzoli, and M. Romé, "Broadband radio frequency plasma generation in a penning–malmberg trap.", *Plasma Sources Sci. Technol.*, vol. 19, no. 4, p. 045 013, 2010.

[39] M. Romé, F. De Luca, G. Maero, B. Paroli, and R. Pozzoli, "Radio frequency generation of an electron plasma in the malmberg-penning trap eltrap", in *37th EPS Conference on Plasma Physics*, ser. European Conference Abstracts, vol. 34A, European Physical Society, 2010, P5.412.

[40] K. S. Fine, A. C. Cass, W. G. Flynn, and C. F. Driscoll, "Relaxation of 2d turbulence to vortex crystals", *Phys. Rev. Lett.*, vol. 75, 3277, 1995.

[41] A. C. Cass, "Experiments on vortex symmetrization in magnetized electron plasma columns", PhD thesis, University of California, San Diego, 1998.

[42] C. F. Driscoll, "Observation of an unstable l=1 diocotron mode on a hollow electron column", *Phys. Rev. Lett.*, vol. 64, p. 645, 1990.

[43] K. S. Fine, A. C. Cass, W. G. Flynn, and C. F. Driscoll, "Relaxation of 2d turbulence to vortex crystals", *Phys. Rev. Lett.*, vol. 75, p. 3277, 1995.

[44] A. A. Kabantsev, K. A. Thompson, and C. F. Driscoll, "First experiments with e-/h- plasmas: Enhanced centrifugal separation from diocotron mode damping", in *AIP Conference Proc*, vol. 1928, 020008, 2018.

[45] V. V. Gorgadze, L. Friedland, and J. S. Wurtele, "Autoresonant control of a pre-excited diocotron mode", *Phys. Plasmas*, vol. 14, p. 082 317, 2007.

[46] K. Gomberoff, H. Higaki, C. Kaga, K. Ito, and H. Okamoto, "Autoresonances of m=2 diocotron oscillations in non-neutral electron plasmas", *Phys. Rev. E*, vol. 94, p. 043 204, 2016.

[47] K. S. Fine, "Experiments with the l = 1 diocotron mode", PhD thesis, University of California, San Diego, 1988.

[48] M. Brioschi, "Controllo attivo di vortici di plasmi non neutri e magnetizzati", BS thesis, Università degli Studi di Milano, 2018.

[49] T. B. Mitchell and C. F. Driscoll, "Symmetrization of 2d vortices by beat-wave damping", *Phys. Rev Lett.*, vol. 73, p. 2196, 1994.

[50] A. A. Kabantsev, C. Y. Chim, T. M. O'Neil, and C. F. Driscoll, "Diocotron and kelvin mode damping from a flux through the critical layer", *Phys. Rev. Lett.*, vol. 112, p. 115 003, 2014.

[51] J. Fajans, E. Gilson, and L. Friedland, "Autoresonant (nonstationary) excitation of the diocotron mode in non-neutral plasmas", *Phys. Rev. Lett.*, vol. 82, no. 22, p. 4444, 1999.

[52] R. Chu, J. S. Wurtele, J. Notte, A. J. Peurrung, and J. Fajans, "Pure electron plasmas in asymmetric traps", *Phys. Fluids B*, vol. 5, no. 7, pp. 2378–2386, 1993.

[53] A. Ashourvan and D. H. E. Dubin, "Collisionless and collisional effects on plasma waves from a partition squeeze", *J. Plasma Physics*, vol. 81, 305810202, 2015.

List of Publications

As of January 2021

Refereed publications

- L. Serafini, I. Drebot, A. Bacci. F. Broggi, C. Curatolo. A. Marocchino, N. Panzeri. V. Petrillo, A. R. Rossi and M. Rossetti Conti, *"A muon source based on plasma accelerators"*, Nucl. Instrum. Meth. A 909, 309 (2018)
- M. Cavenago, M. Romé, G. Maero, M. Maggiore, L. Bellan, F. Cavaliere, M. Comunian, A. Galatà, N. Panzeri, A. Pisent, L. Pranovi and A. M. Porcellato, *"Development and installation of a radio frequency quadrupole test"*, Rev. Sci. Instrum. 90, 113324 (2019)

Publications in preparation

- K. A. Thompson, A. A. Kabantsev, N. Panzeri and C. F. Driscoll. *"Measurements of the parallel temperature profile in Nonneutral Plasmas"* in preparation for Physics of Plasmas.
- K. A. Thompson, A. A. Kabantsev, N. Panzeri and C. F. Driscoll. *"Measurements of Cross-Magnetic-Field Heat Transport in Pure Electron Plasmas"* in preparation.

Publications in conference proceedings

- G. Maero, N. Panzeri, R. Pozzoli and M. Romé, *"Dynamics and stability in RF-generated nonneutral plasmas"*, in Europhysics Conference Abstracts Vol. 42A, O4.J503 Proceedings of the 45th EPS Conference on Plasma Physics (Prague, Czech Republic, 2018), ed. by S. Coda, J. Berndt, G. Lapenta, M. Mantsinen, C. Michaut, S. Weber (European Physical Society, 2018)

- M. Romé, G. Maero, N. Panzeri and R. Pozzoli, *"Resonant excitation of high-order diocotron modes with rotating RF fields"*, in Europhysics Conference Abstracts Vol. 42A, P1.4003 Proceedings of the 45th EPS Conference on Plasma Physics (Prague, Czech Republic, 2018), ed. by S. Coda, J. Berndt, G. Lapenta, M. Mantsinen, C. Michaut, S. Weber (European Physical Society, 2018)

- G. Maero, L. Lanzanova, N. Panzeri, R. Pozzoli and M. Romé, *"Ion instability and off-axis equilibrium in a RF-sustained nonneutral plasma"*, in Europhysics Conference Abstracts Vol. 43C, P2.4004, Proceedings of the 46th EPS Conference on Plasma Physics (Milano, Italy, 2019), ed. by C. Riconda, S. Brezinsek, K. McCarty, K. Lancaster, D. Burgess, P. Brault, D. Farina (European Physical Society, 2019)

- M. Romé, G. Maero, N. Panzeri and R. Pozzoli, *"Selective excitation of Kelvin-Helmholtz modes with rotating electric fields"*, in Europhysics Conference Abstracts Vol. 43C, P2.4003, Proceedings of the 46th EPS Conference on Plasma Physics (Milano, Italy, 2019), ed. by C. Riconda, S. Brezinsek, K. McCarty, K. Lancaster, D. Burgess, P. Brault, D. Farina (European Physical Society, 2019)

Acknowledgments

Everything I learned, everything I did during these years I owe it to my mentors, supervisors and colleagues, and hopefully I said "Thanks" not one, but a thousand times. What a bitter, unfair hunt would be for those who helped me, to look for their well earned gratitude among the pages of this dissertation!
Delayed courtesies often miss their mark, however, let these acknowledgments be fixed, here, not to be dispersed and forgotten.
My PhD career would not have been possible without the continuous and attentive support of my supervisor, Massimiliano, that allowed me to choose freely my path.
I'm deeply indebted to Giancarlo: he has been incredibly patient nurturing me throughout these years, and I could barely call myself an experimentalist without his careful teachings and earnest mentoring.
I also would like to acknowledge the assistance of Francesco Cavaliere and the mechanical workshop crew: my results would have been way less colorful without their prompt assistance.
Many thanks to the UCSD group: they kindly welcomed me, despite all I could bring was my inexperience.
Firstly thanks to Fred. I could not wish for a wiser and more cunning "scientific mother", as he defines himself: always keen on questioning, not for the sake of doubt itself, but to aim to intelligible, affirmative, scientific statements.
Thanks to Andrey, my CamV mentor, for unraveling all the challenges an experimentalist has to face, with the unwavering optimistic temper of Russians.
I am extremely grateful to Kurt: he has been entirely good with me, always prone to assist with the utmost care and sheer passion; helping me with everything, from the insidious electronics details to the most refined experiments.
Thanks also to Dan, Francois and Tom, for the stimulating discussions and mindful insights.
Thanks to my family, for standing still while I wander.
Friendships are frail things, they rarely survive the merciless ailment of time, the scourge of distance. Yet, some fire keeps burning, ablaze. To those whose flame still flickers, I thank you, for your unyielding and inextinguishable presence. But thanks also to those whose fire faded.
Plasma taught me we are rarely aware of the meaningfulness of our interactions.